UAB
Universitat Autònoma de Barcelona

Radiation Hard Timing 3D Detectors for Future Colliders

Òscar David Ferrer Naval

ADVERTIMENT. L'accés als continguts d'aquesta tesi queda condicionat a l'acceptació de les condicions d'ús establertes per la següent llicència Creative Commons: https://creativecommons.org/licenses/?lang=ca

ADVERTENCIA. El acceso a los contenidos de esta tesis queda condicionado a la aceptación de las condiciones de uso establecidas por la siguiente licencia Creative Commons: https://creativecommons.org/licenses/?lang=es

WARNING. The access to the contents of this doctoral thesis it is limited to the acceptance of the use conditions set by the following Creative Commons license: https://creativecommons.org/licenses/?lang=en

UNIVERSITAT AUTÒNOMA DE BARCELONA

DOCTORAL THESIS

Radiation Hard Timing 3D Detectors for Future Colliders

Author:
Òscar David Ferrer Naval

Supervisors:
Giulio Pellegrini
Neil Moffat

A thesis submitted in fulfillment of the requirements
for the degree of Doctor of Philosophy

in the

Institut de Microelectrònica de Barcelona
Radiation Detector Group

July 12, 2024

UNIVERSITAT AUTÒNOMA DE BARCELONA

Abstract

Physics faculty
Radiation Detector Group

Doctor of Philosophy

Radiation Hard Timing 3D Detectors for Future Colliders

by Òscar David Ferrer Naval

This thesis focuses on the characterization and simulation of 3D silicon sensors fabricated at the Centro Nacional de Microelectrónica (IMB-CNM-CSIC) within the framework of the RD50 collaboration. This work is encouraged by the upcoming upgrades for the Large Hadron Collider (LHC), the High-Luminosity LHC (HL-LHC), and the planned Future Circular Collider (FCC). These upgrades will increase the number of events per collision, which requires radiation hard silicon sensors with good time resolution to properly resolve events in time. 3D sensors are considered the best candidates for radiation harsh environments. Their short inter-electrode distance leads to a shorter travelling distance for drifting carriers, reducing the probability of being trapped by non-ionizing effects. Additionally, they yield faster signals, necessary for good time resolution performance. In this work, 3D sensors built on $200 \mu m$ thick n-type wafers are studied, both before and after various levels of irradiation. In Chapter 2, an electrical characterization is performed. In Chapter 3, devices are studied using an infrared laser to investigate charge collection and time resolution. In Chapter 4, a radioactive source setup using strontium-90 is commissioned for the Radiation Laboratory at CNM and used to study the sensors' performance with ionizing particles in terms of charge collection efficiency and time resolution. I Chapter 5, 3D sensors designed for timing applications, featuring thicker wafers and a hexagonal distribution of pixels, are investigated with electrical characterization, and studied with simulations to understand the difference with the usual orthogonal geometry.

Acknowledgements

First and foremost, I would like to thank Giulio and Neil for all their guidance and help throughout the thesis and to give me the opportunity to make this possible. I would also thank the entire Radiation Detector Group and those who were part of it for the extremely nice willingness to cooperate and to help each other, whether by getting sensors wire-bonded, providing pieces of code, or sharing required knowledge - to work with such a good environment makes trying times easier to overcome. Including in no particular order: Jairo, Ivan, Milos, Albert, Maria, Javier, Manolo, Celeste, Joan Marc, Miguel, Consuelo, Marcio, Eric, Esteve and Daniela. Thanks should be provided as well to David Quirion, for shedding so much light and knowledge at the beginning of this journey. Further thanks go to stuff at CNM - Marta and Alberto for carrying on so many wire-bondings, Xavier and Libertad for the FIB processes, the IT team for helping with simulation software issues and Jordi for kindly lending the oscilloscope so many times. I would also like to thank the CNM clean room staff for the invaluable importance of the sensors production, without which any of this work would be possible. Deep thanks would have to go for the pixel detector's group from IFAE for the opportunity to use their facilities whenever it was required, making me always feel welcomed and for helping me whenever anything was required. Without Stefano, Sebastian, Juan, Viveka, Giorgos, specially the TCT measurements would not have been posible. I would also like to thank Vagelis for the great opportunity of the stay at CERN, which provided me an experience from which much I learned. Also to Jakob for accompanying and helping me during the experience.

Last, but not least, I would like to wholeheartedly thank my friends and family, who supported me through all these years and helped me being who I currently am. And my soulmate, for everything you have done and what is yet to come.

This work has been financed by the Spanish Ministry of Science and Innovation (MCIN/AEI/10.13039/501100011033/) and by the European Union's FEDER program "A way of making Europe". Project references: RTI2018-094906-B-C22, PID2020-113705RB-C32

Contents

Abstract **iii**

Acknowledgements **v**

1 Radiation Silicon Sensors for Particle Accelerators **1**

1.1 Introduction 1

1.1.1 LHC 2

1.1.2 High Luminosity - LHC 3

1.1.3 Future Circular Collider 4

1.2 Silicon Physical Properties 6

1.3 P-N Junctions 9

1.3.1 Leakage Current 11

1.3.2 Capacitance 12

1.4 Radiation-matter Interactions 13

1.4.1 Electromagnetic Radiation 13

1.4.2 Charged particles 15

1.4.3 Signal Formation in Silicon p-n Junctions 17

1.5 Non-ionizing effects on silicon 18

1.5.1 Increase of depletion voltage 20

1.5.2 Increase of leakage current 20

1.5.3 Decrease of charge collection 21

1.5.4 Annealing 22

1.6 Silicon P-N junctions as Radiation Detectors 23

1.6.1 Planar Sensors 25

1.6.2 3D sensors 25

1.7 Time Resolution 27

1.7.1 Jitter 28

1.7.2 Time Walk 29

1.7.3 Landau Noise 30

1.7.4 Non-uniform Weighting Field 30

1.7.5 Waveform analysis for time resolution measurements . 31

1.8 Physical models for TCAD simulations 32

1.8.1 Mobility models . . . 33
1.8.2 Generation-recombination models . . . 34
1.8.3 Effective Intrinsic Density . . . 35

2 3D Double Sided n-on-n characterization and technology 37
2.1 N-on-N technology and samples . . . 38
2.1.1 Re-metalization for the small test structures . . . 40
2.2 Electrical characterization . . . 42
2.2.1 Before irradiation . . . 42
2.2.2 After irradiation . . . 46

3 Transient Current Technique (TCT) measurements 55
3.1 Setup . . . 55
3.2 Focus Scan . . . 58
3.3 Signal calibration with beta source . . . 61
3.4 Pad diode arrays . . . 62
3.4.1 2D charge collected map . . . 63
3.4.2 Time resolution . . . 67
3.5 Small test structures . . . 70
3.5.1 2D charge collection map . . . 71
3.5.2 Time resolution . . . 74
3.5.3 Charge Collection Efficiency . . . 74
3.5.4 Conclusions and Future work on TCT measurements . . . 78

4 Beta-source setup 81
4.1 Setup . . . 81
4.2 Timing Calibration . . . 83
4.3 3D Test Structures . . . 87
4.4 Results . . . 87
4.5 Discussion and future work . . . 91

5 3D sensors for Timing Applications 93
5.1 Architecture and Geometry . . . 93
5.2 Electrical Characterization . . . 96
5.3 TCAD Simulations . . . 99
5.3.1 Structure models . . . 102
5.3.2 Electrical Characteristics . . . 105
5.3.3 Electric Field Distribution and Uniformity . . . 107
5.4 Conclusions and Discussion . . . 113

6 Conclusions and Future Work **117**

A Simulation Models **123**

A.1 Mobility models 123

A.1.1 Doping dependence 123

A.1.2 Lombardi Model 124

A.1.3 High Field Saturation 125

A.1.4 Carrier-Carrier Scattering 126

A.2 Generation-recombination models 126

A.2.1 Schockley-Reah-Hall Recombiantion 126

A.2.2 Auger Recombination 127

A.2.3 Avalanche - Impact Ionization 128

A.3 Effective Intrinsic Density 129

List of Figures

1.1 In A, the diagram of the ATLAS detector with its different parts. In B, a computer-generated image of the Inner Tracker pixel detector. 4
1.2 Computer generated image with a size comparison between the LHC and the project for the FCC [13]. 5
1.3 In *A* the energy bands of intrinsic silicon, and in *B* the carrier concentration dependence on temperature in intrinsic silicon [16]. 7
1.4 Representation of introducing an acceptor (A) or a donor (B) in a silicon crystallographic lattice. 9
1.5 Representations of the (from left to right) band diagram, density of states, Fermi-Dirac distribution and carrier concentrations for (a) intrinsic, (b) n-type and (c) p-type at thermal equilibrium. [16] 10
1.6 Figures representing, along the junction, the charge distribution (A), the electric field (B), the potential energy, where ψ_{bi} is the built-in potential (C) and the energy bands diagram (D). . 11
1.7 I-V curve for an ideal p-n junction, according to Eq. 1.7. [16] . 12
1.8 $1/C^2$ vs bias for a sample sensor further studied in Chapter 2. The full depletion voltage is set by the intersection of the fits to the initial increase and the plateau after full depletion. . . . 14
1.9 Wavelength dependence of the absorption coefficient. [21] . . 15
1.10 Light transmission intensity dependence with the doping concentration in silicon with a wavelength of $1550nm$. [22] 16
1.11 Rate of energy loss due to ionization as a function of the kinetic energy of a charged pion traversing silicon (effective ionization potential $I = 173eV$) with (continuous line) and without (dotted line) density and shell corrections. [17] 17
1.12 Graphical representation of the different type of lattice defects that non-ionizing effects can create in the silicon lattice. [19] . 19

1.13 Displacement damage function $D(E)$ normalized to $95 MeV mb$ for neutrons, protons and electrons. [19] 20
1.14 Depletion voltage and effective doping concentration versus fluence. [19] 21
1.15 Variation of the doping concentration versus annealing time. Figure adapted from [26]. 23
1.16 Variation of charge collection efficiency versus annealing time in a $300 \mu m$ thick strip sensor. [31]. 24
1.17 Schematic representation of the Low Gain Avalanche Detector. The p-type multiplication layer is the highly doped region that leads to impact ionization, resulting in intrinsic gain. The Junction Termination Extension (JTE) separates separates the high electric field from the multiplication layer from nearby pixels, and limits the collected charge to a controlled region. Extracted from [33] 26
1.18 Cross section representations for 3D sensors (A) and planar sensors (B). 27
1.19 Graphic representation of the necessity of a good time resolution for silicon sensors. If the tracks are only resolved in space but not in time (left), it is not possible to reconstruct the whole path, resulting in loss of information. [37] 28
1.20 An uncertainty in the y-axis of dV causes a trigger variation in time of dt, which translates into a decrease in time resolution. [38] 29
1.21 Representation of the time walk contribution to the time resolution. If only the trigger ToA is considered, different ToAs are given for identcally shaped but differently scaled signals (A). Using the CFD method largely reduces this effect (B). Figure adapted from[39] 30
1.22 Probability distribution of energy deposition by an ionizing particle, following a Landau distribution [41] 31

2.1 Depletion voltages versus fluence level, separated according different initial depletion voltages. Extracted from [47]. 38
2.2 Schematic cross section of the 3D n-on-n architecture studied in this work. 39

2.3 SEM images of the pads for the small test structures, showing that (A) there was no metal before depositing with FIB, (B) how the deposited metal looks like, (C) that there is a thin layer of metal around the area where the metal is deposited, and (D) the etching in the shape of strips to separate the channels. . . . 41
2.4 Image of the probe station setup at CNM, highlighting the different components. 41
2.5 I-V curves measured at room temperature ($T = 20°C$) for the RD53B sensors of types 1-X (A), 2-X (B) and 3-X (C). 43
2.6 I-V curves measured at room temperature ($T = 20°C$) for the pad diode arrays of 5-X (A), 6-X (B), 7-X (C) and 8-X (D). . . . 44
2.7 C-V curves of 5-X and 8-X devices, with the capacitance represented as quantity per pixel. 45
2.8 I-V curves taken at low temperature ($T = -20°C$) for the sensors of types 6-X (A) and 8-X (B). 45
2.9 I-V curves of some diode arrays with different geometries and sizes from different wafers. 46
2.10 Mask design for the test structures (A) and the I-V taken from a few samples from wafer 4 (B) 47
2.11 I-V curves for the 1-X (A), 2-X (B) at different fluence levels. . 48
2.12 I-V curves for the 6-X(A) and 8-X (B) at different fluence levels. 49
2.13 $1/C^2$ versus V curves for irradiated pad diodes 6-X (A) and 8-X (B). The curve before irradiation was not included for the 8-X devices. The C-V for the 6-X devices were done at a frequency of 1kHz due to other frequencies not yielding reliable enough results. 51
2.14 Full Depletion voltage for the $50x50$ μm (black) and $25x100$ μm (blue) geometries. 51
2.15 I-V curves of small test structures irradiated at different fluence levels. 52
2.16 Leakage current of the test structures at a bias of 100V for the different fluence levels. 53

3.1 Photos of the TCT setup, of (A) the equipment for biasing, cooling down and the oscilloscope, and (B) the optics to create two signals, as well as the amplifier and the DUT. 56
3.2 Image of the PCB board designed by DESY used for the TCT measurements. The DUT is a 300 μm thick PiN sensor used for signal calibration, explained in section 3.3. 57

3.3 Schematic representation of the circuit with which the beam from the laser is separated in two different paths to induce two signals to the sensor. 58
3.4 A: Charge collected along the scanning axis, corresponding to the direction represented in Fig. 3.5. B: The FWHM extracted from the fits for each of the taken curves in A. 59
3.5 Graphical representation of different spot sizes with relation to the test structures and the travelled distance along the focus scan from Fig. 3.4. The diameters of the spot sizes correspond, in the scale of the mask layout and from top to bottom, to 40 μm, 20 μm and 12 μm. 60
3.6 Histogram distribution of the signal height taken for the planar PiN reference sensor. The mean value of 63mV has been used as the charge generation resulting from the laser intensity and the iris opening of the optical focusing system. 62
3.7 Representation of the mask for the 6X devices. A zoomed in region has been presented so that can be compared with the 2D charge collection map. 63
3.8 Plot of the refractive index for different doping concentrations in polysilicon . Graphic extracted from [61]. 64
3.9 2D maps of the charge collected for different fluence levels at different devices. Must be taken into account that some of them have different step size and total scanning distance for both directions. 65
3.10 2D map of the charge collected for the device irradiated at the fluence level of $1 \cdot 10^{17}$ n_{eq}/cm^2. Red and black circles highlight the intercalation of the n-type electrodes, with the positions equidistant to the n-electrodes coinciding with regions with low charge collection. 66
3.11 Time resolution for 6-X sensors irradiated at different fluence levels at different bias voltages for a 1 MIP-like signal calibration. Since the sensor irradiated at $1E16 n_{eq}/cm^2$ has a much higher value for the time resolution a separate plot for the other fluences has been done so that the difference in time resolution with voltage can be better seen. 68

3.12 Time resolution for 6-X sensors irradiated at different fluence levels at different bias voltages for a 2 MIP-like signal calibration. Since the sensor irradiated at $1 \cdot 10^{17} n_{eq}/cm^2$ has a much higher value for the time resolution, a separate plot for the other fluencies is provided to better illustrate the variation in time resolution with bias voltage. 69
3.13 Time resolution versus bias for 6-X sensors irradiated at different fluence levels, with the laser intensity set at different multiple times 1-MIP. 69
3.14 2D map of the time resolution (A) and peak amplitude (B) taken for a 6-X sensor irradiated at an equivalent fluence level of $1E17 n_{eq}/cm^2$ and biased at 250V. The laser intensity calibration was of 3-MIP. 70
3.15 2D maps of the charge collected for different fluence levels for the test structures. The operational voltages from no fluence to higher fluence levels were 30V (Before Irr), 30V ($1 \cdot 10^{14} n_{eq}/cm^2$), 150V($1 \cdot 10^{15} n_{eq}/cm^2$) and 150V ($5 \cdot 10^{15} n_{eq}/cm^2$). 72
3.16 2D maps of the charge collected for different fluence levels for the test structures. The operational voltages from lower to the highest fluence level 220V ($1 \cdot 10^{16} n_{eq}/cm^2$), 300V ($5 \cdot 10^{16} n_{eq}/cm^2$) and 350V ($1 \cdot 10^{17} n_{eq}/cm^2$) 73
3.17 In A, time resolution of the test structures irradiated at different fluence levels at different bias voltages for a 1 MIP-like signal calibration. In B, amplitude of the signal peak for the different fluence levels at different bias voltages. 75
3.18 Noise RMS (A) and risetime (B) values versus bias at the different equivalent fluence levels. 76
3.19 Charge collection efficiency versus bias at the different fluence levels. 77
3.20 Voltage at which a 100% CCE is reached at the different fluence levels. 78

4.1 Picture of a UCSC board used for the Sr90 source setup. 82
4.2 Pictures from the Sr90 source setup. On the left, the used equipment for biasing, the oscilloscope, the metal box and the freezer, and on the right where the sensors are placed, the amplifiers and the sensor used to monitor the temperature. 83
4.3 Schematical representation of the Sr90 source setup. 83

4.4 Gain (A) and current at rom temperature (B) versus reverse bias voltage from devices from the run 13002 for devices from different wafers. The sensors used for the calibration are from the same run as the sensor in green. Measurements and graphs done by Mr. Jairo Villegas. 84
4.5 Mask diagram of the LGAD sensors used for the Sr90 source setup calibration. 85
4.6 Time resolution (A), charge collected (B) and the jitter contribution (C) from the CNM LGADs used as reference sensors. . 86
4.7 Sample histogram distribution of the difference in ToA together with the Gaussian fit. 88
4.8 Graphical representation versus the reverse bias for different fluence levels of: the noise RMS (A), the risetime (B), the weighting field distortion contribution (C), the jitter (D) and the time resolution (E) of the DUT. 90
4.9 Graphical representation versus the reverse bias for different fluence levels of the peak amplitude (A) and the CCE (B). . . . 91
4.10 Sample waveform for the fluence levels of $1 \cdot 10^{15} n_{eq}/cm^2$ (A) at 100V. 91

5.1 Mask designs for the hexagonal distribution of electrodes for the 3D sensor with a p-n radius distances of $30\mu m$ (A) and $50\mu m$ (B). 95
5.2 I-V curves taken from 1-X (A) and 2-X (B) devices from wafer 4, 5 and 6. Attention must be paid to the scale of the x-axis, being the one for the 1-X (hexagonal) larger than the ones for the 2-X (orthogonal). 97
5.3 I-V curves taken from ALTIROC pixels, which feature different array sizes, with electrodes in hexagonal arrays with p-n distances of 30 μm (A) and 50 μm (B). 98
5.4 I-V curves taken from test structure with hexagonal (A) and orthogonal (B) geometries, taken at room temperature (red) and low temperature (blue). 100
5.5 Representation of $1/C^2$ versus bias for 100x100 pixel arrays, represented as the quantity per pixel. 101
5.6 Representation of $1/C^2$ versus bias for different pixel arrays within the ALTIROC devices, represented as the quantity per pixel. 101

5.7 Graphical representation of the symmetries applied by using images of the mask layout. The n-type electrodes are inside the p-stop while the p-type are found in between them. 103
5.8 Simulated structures for the orthogonal geometry (A) and hexagonal geometries with p-n distances of 30 μm (B) and 50 μm (C). A legend for the doping concentrations is presented (D). . . . 103
5.9 Cross sections of the doping concentration from the simulated structures of Fig. 5.8 for the orthogonal geometry (A) and hexagonal geometries with p-n radius distances of 30 μm (B) and 50 μm (C). A legend for the doping concentrations is presented (D). 104
5.10 I-V curves resulting from the simulations for the different geometries. The leakage current saturates at below 10V while the breakdown occurs at 60V. 105
5.11 $1/C^2$ vs V from simulations (straight line) and measurements (empty symbols). 106
5.12 Electric field distributions for the orthogonal geometry, applying biases of 1V (A), 5V (B), 10V (C) and 60V (D). 108
5.13 Electric field distributions at a cross section of the orthogonal geometry structure, with applied biases of 1V (A), 5V (B), 10V (C), and 60V (D). 108
5.14 Electric field distributions for the hexagonal geometry with p-n distance of 30 μm, applying biases of 1V (A), 5V (B), 10V (C) and 60V (D). 109
5.15 Electric field distributions at a cross section of the hexagonal geometry structure with p-n distance of 30 μm, with applied biases of of 1V (a), 5V (b), 10V (c), and 60V (d). 109
5.16 Electric field distributions for the hexagonal geometry with p-n distance of 50 μm, applying biases of 1V (A), 5V (B), 10V (C) and 60V (D). 110
5.17 Electric field distributions at a cross section of the hexagonal geometry structure with p-n distance of 50 μm, with applied biases of 1V (a), 5V (b), 10V (c), and 60V (d). 110
5.18 2D Histograms of the frequency of the absolute values of the electric field depending on the distance from the n-type electrode located at the (0,0) position. 112

5.19 Mean value of the electric field depending on the distance. The error bars represent the spread of the values of the electric field within a given distance from the n-type electrode. 113
5.20 Mean value of the electric field. 114

List of Tables

2.1 List of the samples featured in the run 10339 and some of their key characteristics. 39

4.1 List of the obtained time resolutions with different biases at various fluence levels. 88

A.1 Coefficients used for the Masetti model. 124
A.2 Coefficients used for the Lombardi model. 125
A.3 Coefficients used for the Canali model. 126
A.4 Coefficients used for the auger recombination effect model. . . 128
A.5 Coefficients from the van Overstraeten-de Man model for impact ionization. 129

Chapter 1

Radiation Silicon Sensors for Particle Accelerators

1.1 Introduction

The Standard Model (SM) is the most accepted physical model which describes three of the four fundamental forces in nature: weak, strong and electromagnetic interactions, lacking yet the possibility to unify them with the gravitational interaction. [1] The SM also describes the underlying fundamental particles that constitute matter, including quarks, leptons, bosons, or notably the Higgs boson which was first theoretically predicted by the SM and later observed experimentally [2], [3].

To observe these subatomic particles, particle colliders are employed. In these experiments, a large amount of kinetic energy is transferred to bunches of charged particles which are made to collide. The resulting nuclear interactions produce other particles, which interact with radiation silicon sensors, this allows for the reconstruction of the tracks of the particles. With these tracks, it is possible to deduce physical properties of the crossing particles.

This thesis is focused on the performance of the radiation silicon sensors used in particle accelerators. First the LHC, the largest existing particle collider will be introduced, followed by its upcoming upgrade, the High Luminosity LHC (HL-LHC). Next, the project Future Circular Collider (FCC) will be discussed together with its objectives. Additionally, the physical principles in which radiation silicon sensors are based on will be explained, including the concepts of charge collection efficiency, radiation damage and the time resolution. Finally, the physical properties used for the Technological Computer-Aided Design (TCAD) simulations used for this thesis are presented and more thoroughly explained in Appendix A.

1.1.1 LHC

The largest particle collider to date is the Large Hadron Collider (LHC), located in Geneva, on the border between Switzerland and France. It is primarily operated by the European Organization for Nuclear Research (CERN) and involves collaborating institutes from around the world. The LHC is built at a depth ranging from $50m$ to $150m$ underground and comprises a ring with a circumference of $27km$. It operates two proton beams that collide with each other, achieving a record energy of 13.6 TeV at the beginning of Run 3, which started in July 2022 [4]. Along the LHC's pipes there are currently nine experiments, each with different objectives according to their unique characteristics [5]:

- ATLAS (A Toroidal LHC ApparatuS) and CMS (Compact Muon Solenoid): These are the most general-purpose ones. Both study the SM, including the Higgs boson, search for extra dimensions, and potential candidates for dark matter. Despite sharing the same goals, the magnet-system design and the technical approaches are different.

- LHCb (Large Hadron Collider beauty): This experiment aims to observe the slight asymmetry between matter and antimatter present in interactions involving the b-quark.

- ALICE (A Large Ion Collider Experiment): ALICE studies the properties of quark-gluon plasma created immediately after the collision due to the large temperatures reached. This state of matter is believed to have existed right after the Big Bang. ALICE observes how the quark-gluon plasma expands, cools, and forms the particles that constitute matter in the universe. The properties of the quark-gluon plasma are key issues for the theory of quantum chromodynamics (QCD).

- LHCf (Large Hadron Collider forward): LHCf measures particles produced very close to the direction of the beams to test models estimating the primary energy of ultra-high-energy cosmic rays. It consists of two detectors placed 140m away from the ATLAS collision point, allowing for nearly zero-degree measurements from the proton beam direction.

- MOEDAL-MAPP (Monopole and Exotics Detector At the LHC - MoEDAL Apparatus for Penetrating Particles): This experiment searches hypothetical highly ionising particles such as magnetic monopoles or other exotic particles that could indicate physics beyond the Standard Model.

- TOTEM (TOTal cross section, Elastic scattering and diffractive dissociation Measurement at the LHC): TOTEM aims to make precise measurements of protons that emerge from proton-proton collisions at small angles, occurring in a forward direction not accessible by other LHC experiments.
- FASER (ForwArd SEarch ExpeRiment): FASER searches for light and extremely weakly interacting particles, such as dark matter or neutrinos, and investigates the imbalance between matter and antimatter in the observable universe.
- SND @ LHC (Scattering and Neutrino Detector at the LHC): This experiment studies neutrinos and particles with no electric charge and extremely low masses, as well as searches for weakly interacting particles not predicted by the Standard Model that could constitute dark matter. Additionally, since neutrinos originate from the decay of particles made of heavy quarks, it also investigates the production of heavy-quark particles at angles that are inaccessible to other LHC experiments.

Among these experiments, the ATLAS and CMS experiments are the most relevant to this thesis. The sensors considered for the inner parts of these experiments are of the same architecture as those studied in this work, the so-called **3D sensors**, due to their high radiation tolerance. This feature is essential for the areas closer to the collision points, where higher radiation per surface area must be withstood. Currently, the Inner Tracker pixel detector (ITk) in the ATLAS experiment features 3D sensors, which were installed in 2017 [6], [7].

1.1.2 High Luminosity - LHC

Run 3 of the LHC is expected to conclude by 2024, at which point much of the physics attainable currently will have been explored. To advance the frontiers of physics discovery, particle accelerators pursue the maximization of two critical values: *beam energy* and *integrated luminosity*. Beam energy is defined as the sum of the energies of the two colliding beams, measured in teraelectronvolts (TeV). The current ion beam collision energy is 13 TeV, designed with a maximum of 14 TeV, a target set to be attained by the High-Luminosity LHC (HL-LHC) [8]–[10].

Integrated luminosity is directly proportional to the number of collisions per unit area over a specified time period [11], and is denoted in the inverse

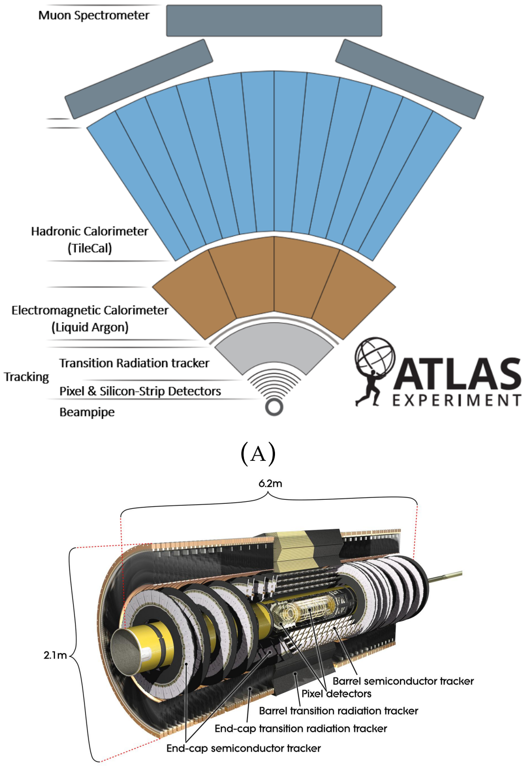
Muon Spectrometer
Hadronic Calorimeter (TileCal)
Electromagnetic Calorimeter (Liquid Argon)
Tracking
Transition Radiation tracker
Pixel & Silicon-Strip Detectors
Beampipe
ATLAS EXPERIMENT
6.2m
2.1m
Barrel semiconductor tracker
Pixel detectors
Barrel transition radiation tracker
End-cap transition radiation tracker
End-cap semiconductor tracker

(A)

(B)

FIGURE 1.1: In A, the diagram of the ATLAS detector with its different parts. In B, a computer-generated image of the Inner Tracker pixel detector.

unit of *femptobarn* $\left[fb^{-1}\right]$. It is expected to increase from the current run's $350fb^{-1}$ to an anticipated $3000fb^{-1}$ by the end of the HL-LHC, representing an almost tenfold increase. This boost in luminosity results in a greater number of events, providing more statistical data that can reveal rare phenomena that might otherwise go undetected [12].

1.1.3 Future Circular Collider

The Future Circular Collider (FCC) is a European project aiming to construct the largest particle accelerator ever built. It will consist of a ring with a diameter of 80-100km, situated in an average depth of 300 meters. The FCC will target collision energies of up to 100 TeV for protons and 350GeV for electrons, with an instantaneous luminosity expected to exceed $10^{34}cm^{-2}s^{-1}$. The FCC is planned to be operational by the time HL-LHC reaches its end in 2040, promising to enable new physics studies. The project includes plans for two different stages: the FCC-ee, focusing on electron-positron collisions,

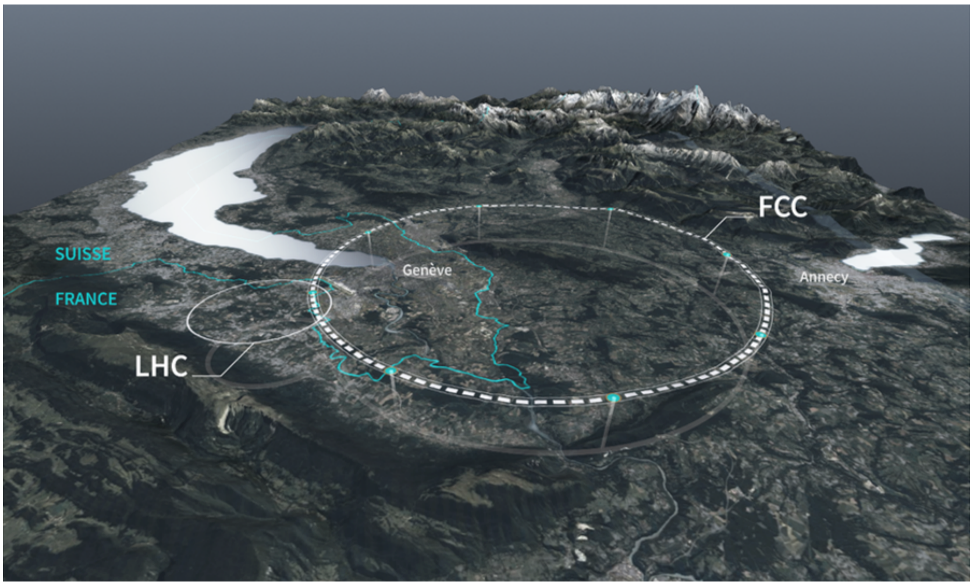

FIGURE 1.2: Computer generated image with a size comparison between the LHC and the project for the FCC [13].

and the FCC-hh, based on hadron-hadron collisions, which will complement each other.

Some of the key areas of focus for the FCC are:

- Follow-up of the Higgs boson: Higher energy interactions will allow for more precise measurements of the production and decay of the Higgs boson and other Standard Model (SM) particles. This could reveal any deviations from the SM and determine whether the Higgs boson is an elementary or composite particle. The increased luminosity will also improve statistical data, providing insights into Higgs self-interaction.
- Search for dark matter: While dark matter is not included in the SM and no experiments can probe the range of masses allowed by astrophysical observations, models suggest it could have masses ranging from GeV to tens of TeV. The FCC could potentially observe particles that interact with dark matter, broadening the search possibilities.
- Mass of the neutrinos: The SM does not predict a mass for neutrinos, although experiments indicate they have a small mass. The FCC aims to discover the origin of this mass, which might not stem from the SM.
- Matter-antimatter asymmetry: The SM includes C-P violation, suggesting a possible asymmetry between matter and antimatter. However, observed C-P violations have not been sufficient to explain the matter

present in the universe. The FCC's higher luminosity could help detect these violations more clearly, enhancing our understanding of this asymmetry.

- Supersymmetry: To explain the unexplained phenomena in current physics, supersymmetric theories propose the existence of supersymmetric particles. The FCC's energy range would enable the observation of these particles.

Overall, many of the most significant questions in contemporary physics cannot be answered by the current largest particle accelerator. The FCC's higher energy and luminosity capabilities are expected to address these major uncertainties. A feasibility study assessing the technical and financial viability of such a facility at CERN has been ongoing since 2023 and is planned to continue until 2027 [14], [15].

1.2 Silicon Physical Properties

Silicon has been a core material in the semiconductor industry due to its abundance on Earth while still featuring the required properties for many electronic applications. Devices based on silicon are typically built on silicon wafers through a series of fabrication steps that vary depending on the application. Despite the use of many other materials during the fabrication process (such as oxides, metals or silicon without crystalline structure) the final device's properties and fabrication methods strongly depend on the intrinsic properties of silicon. In the following sections the most relevant properties of silicon related to this thesis will be highlighted. Most of the information has been extracted from the books from references [16]–[19].

To understand the main properties of silicon as a radiation detector, it is essential to focus on the energy-momentum relationship (E-k) for electrons, as it shows their allowed states. The E-k relation can be found by solving the Schrödinger equation:

$$\left[\frac{-h^2}{2m^*}\nabla^2 + V(r)\right]\psi(r,k) = E(k)\psi(k,r) \tag{1.1}$$

The Bloch theorem states that the Schrödinger equation in a system with periodic potential energy in the direct lattice space can be written as a Bloch function:

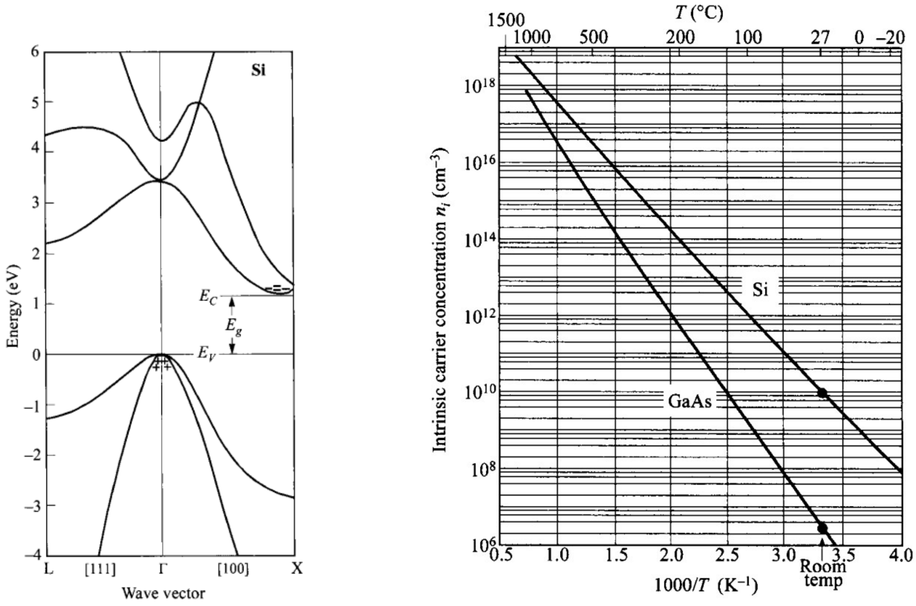

(A)

(B)

FIGURE 1.3: In *A* the energy bands of intrinsic silicon, and in *B* the carrier concentration dependence on temperature in intrinsic silicon [16].

$$\psi(r,k) = exp(jk \cdot r)U_b(r,k) \tag{1.2}$$

Where $\psi(r,k)$ and $U_b(r,k)$ are periodic in the direct lattice space, and b represents the band index. Hence, we have multiple energy bands along the periodicity of the crystalline structure.

By solving equation 1.2 numerically for silicon, we obtain the band structure in Fig. 1.3a. The multiple energy bands can be separated by a gap with no allowed state, the **band-gap**. The energy band below the gap is the **valence band**, and the one above is the **conduction band**. For silicon, the band gap has a value of 1.12eV at room temperature. However, since the maximum of the valence band is at a different wave vector value than the minimum of the conduction band, a phonon interaction is needed for the transition, requiring a total of 3.6 eV to promote an electron to the conduction band, creating an electron-hole pair as a result.

Without external energy injection, electrons cannot move due to the lack of available states in the valence band. One mechanism to promote electrons from the valence band to the conduction band is through thermal energy. In a pure semiconductor, the dependence of the carrier density on temperature is given by:

$$n_i = 4.9x10^{15} \cdot \left(\frac{m_{de} m_{dh}}{m_0^2} \right)^{3/4} M_C^{1/2} T^{3/2} exp \left(-\frac{E_g}{2kT} \right) \tag{1.3}$$

Thus, the carrier concentration is proportional to an exponentially decaying function of temperature. As shown in Figure 1.3b, the carrier concentration increases with temperature. For silicon at room temperature, the amount of carriers is of the order of $10^8 n_i/cm^3$, which for many semiconductor applications is insufficient. This concentration can be modified through a controlled introduction of impurities into the silicon lattice, called **doping**

Silicon has four electrons in its valence band, and due to its crystallographic structure, each silicon atom is bound to four atoms through covalent bonds, hence completing the $3s$ $3p$ electron shell. Introducing impurities with three or five valence electrons creates two scenarios:

- **Acceptors (p-type doping)**: When a silicon atom is replaced by a group III (such as boron) element with three valence electrons, a hole is created because one less electron is available to complete the $3s$ $3p$ shell. This results in a negatively charged region due to filling the remaining covalent bond with an electron. With the carrier majority being holes, the material is classified as p-type.

- **Donors (n-type doping)**: When a silicon atom is replaced by a group V element (such as phosphorus), an extra electron is introduced into the silicon lattice. This extra electron cannot form a covalent bond with silicon atoms, so it becomes free to move and is promoted to the conduction band. Hence, the missing electron effectively leads to a positively charged region with the majority of carriers being the electrons. The material would then be classified as n-type.

These impurities create defects in the lattice that introduce energy levels within the energy band gap shifting the Fermi energy level closer to the valence (conduction) band if the impurity is an acceptor (donor). This increases the probability of having a change of state and promoting an electron from the valence band to the conduction band as a result. Since less energy is needed to promote an electron to the conduction band, the impurities increase the amount of carriers in the material, enhancing the material conductivity.

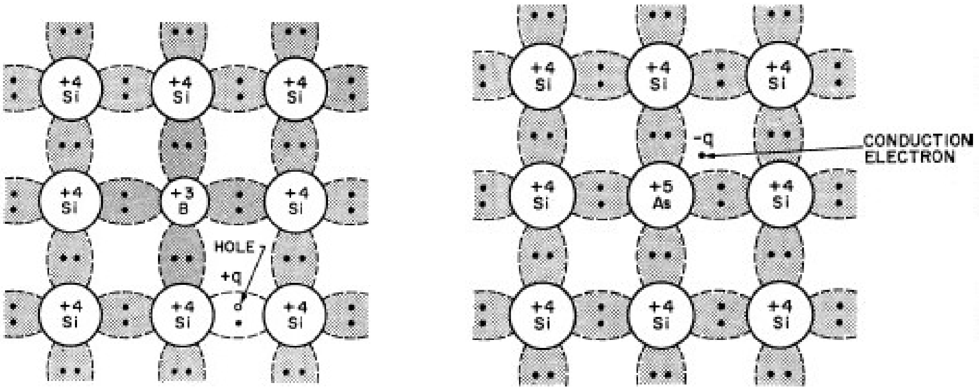

(A) (B)

FIGURE 1.4: Representation of introducing an acceptor (A) or a donor (B) in a silicon crystallographic lattice.

1.3 P-N Junctions

When a p-type semiconductor is joined with an n-type, there is a flow of charge at the interface to achieve an equilibrium for the electric field. Electrons flow from the n-side (donor) to the p-side (acceptor), creating a positively charged region in the n-side. Simultaneously, holes from the p-side diffuse to the n-side, creating a negatively charged region. These combined effects create a region with a charge gradient called the **space-charge region**, or the **depletion region**. The inherent electrostatic charge creates an electrostatic potential known as the built-in voltage (V_{bi}), given by:

$$V_{bi} = \Psi_n - \Psi_n = \frac{kT}{q} \ln\left(\frac{N_A N_D}{n_i^2}\right) \tag{1.4}$$

where n_i is the intrinsic carrier concentration, N_A and N_A are respectively the doping concentrations for acceptors and donors, k is the Boltzmann constant, T the temperature (in Kelvin), and q the charge of an electron. The width of the depletion region can be calculated as:

$$W = \sqrt{\frac{2\epsilon}{q}\left(\frac{N_A + N_D}{N_A N_D}\right) V_{bi}} \tag{1.5}$$

Thus, if one of the doping concentrations is much larger than the other, the depletion will be primarily in the less doped region, and will be given by:

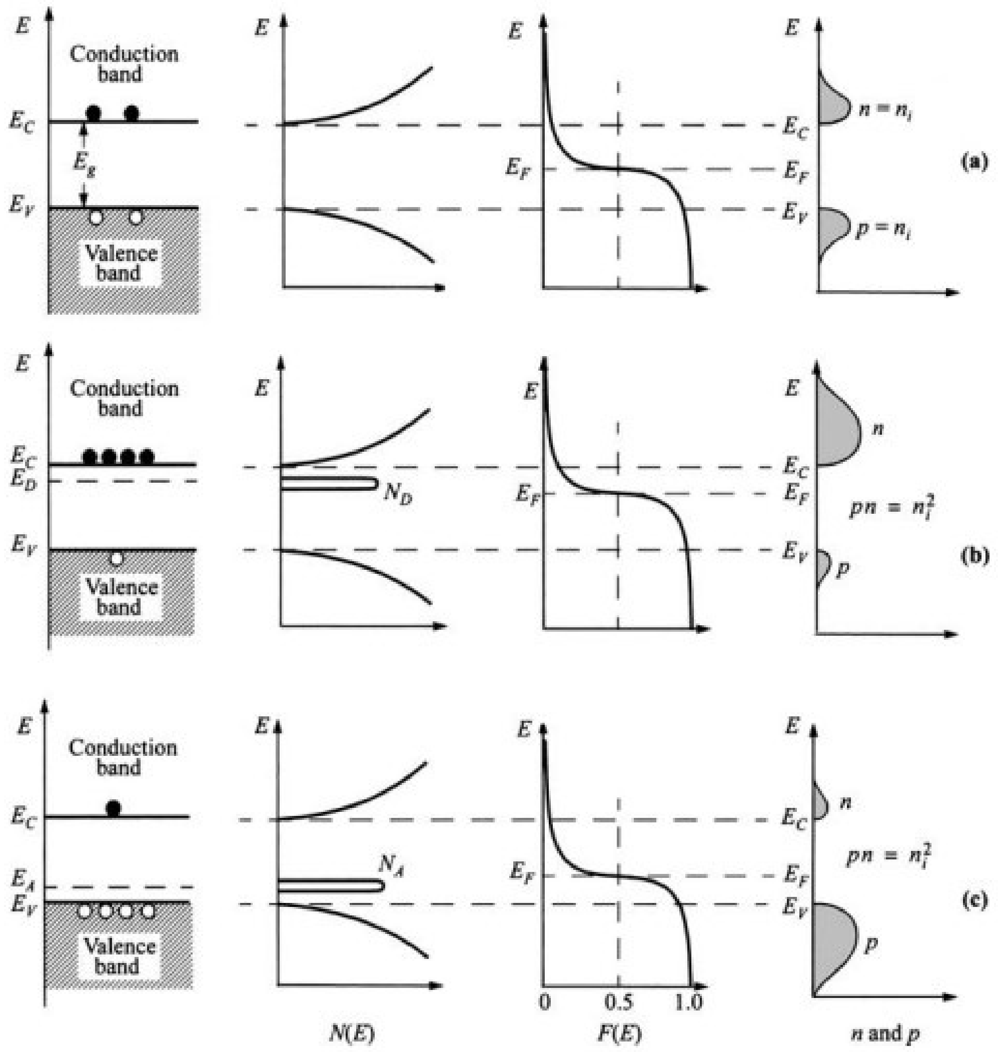
E
Conduction band
E_C
E_g
E_V
Valence band
E
E
E_F
E
E_C
E_F
E_V
$n = n_i$
$p = n_i$
(a)
E
Conduction band
E_C
E_D
E_V
Valence band
E
N_D
E
E_F
E
n
E_C
E_F
$pn = n_i^2$
E_V
p
(b)
E
Conduction band
E_C
E_A
E_V
Valence band
E
N_A
E
E_F
E
n
E_C
$pn = n_i^2$
E_F
E_V
p
(c)
0
0.5
1.0
N(E)
F(E)
n and p

FIGURE 1.5: Representations of the (from left to right) band diagram, density of states, Fermi-Dirac distribution and carrier concentrations for (a) intrinsic, (b) n-type and (c) p-type at thermal equilibrium. [16]

$$W = \begin{cases} \sqrt{\frac{2\epsilon V_{bi}}{qN_D}} & \text{if } N_A >> N_D \\ \sqrt{\frac{2\epsilon V_{bi}}{qN_A}} & \text{if } N_D >> N_A \end{cases} \tag{1.6}$$

In this scenario, there is a potential barrier (Fig. 1.6c) that can only be overcome by carriers through thermal excitation. Thus, assuming that the p-n junction is not at absolute zero, some current will flow. However, when an external bias is applied, there are two scenarios depending on the direction of the bias:

- **Reverse bias** - When the bias is applied against the natural flow of

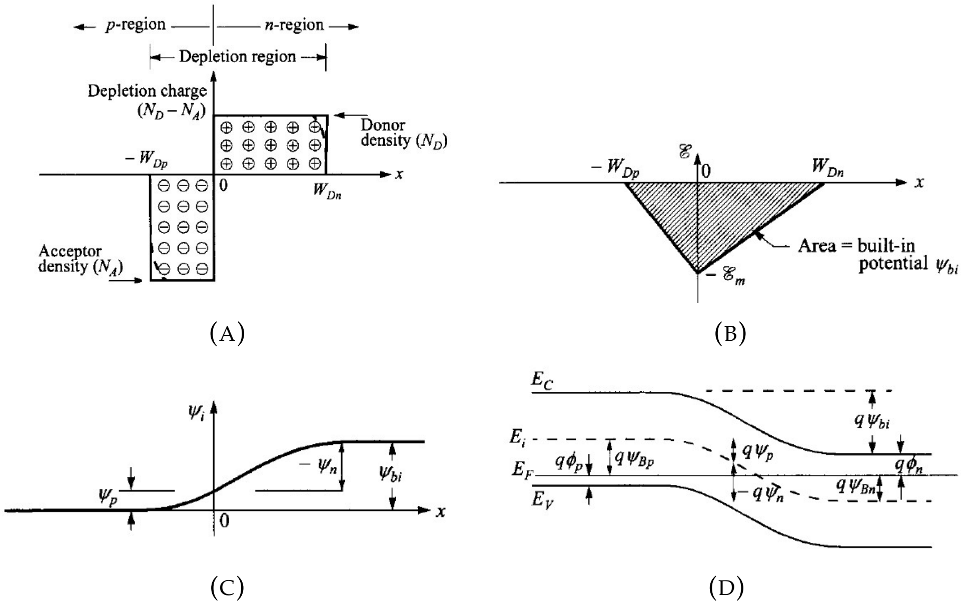
p-region
n-region
Depletion region
Depletion charge
(N_D − N_A)
Donor density (N_D)
− W_Dp
W_Dn
x
0
Acceptor density (N_A)
(A)
ℰ
0
− W_Dp
W_Dn
x
− ℰ_m
Area = built-in potential ψ_bi
(B)
ψ_i
ψ_p
− ψ_n
ψ_bi
0
x
(C)
E_C
E_i
E_F
E_V
qψ_bi
qφ_p
qψ_Bp
qψ_p
qφ_n
qψ_Bn
− qψ_n
(D)

FIGURE 1.6: Figures representing, along the junction, the charge distribution (A), the electric field (B), the potential energy, where ψ_{bi} is the built-in potential (C) and the energy bands diagram (D).

the carriers, with the positive terminal connected to the n-side and the negative to the p-side. In this configuration, electrons flow to the p-side, and holes to the n-side, enlarging the depletion region, resulting in very little current flow. Such small current is called *leakage current* and will be covered more in detail in section 1.3.1.

- **Forward bias** - The bias is applied in favour of the natural flow of carriers, with the positive terminal connected to the p-side and the negative terminal to the n-side. In this configuration, the depletion region decreases and the current increases exponentially with voltage.

1.3.1 Leakage Current

In an ideal p-n diode under bias, the current can be described as:

$$I = I_S \left(e^{\frac{qV}{k_B T}} - 1 \right) \tag{1.7}$$

Where V is the applied bias voltage, and I_S is the saturation current under the reverse bias condition, described by:

$$I_S = \frac{qD_p p_{n0}}{L_p} + \frac{qD_n n_{p0}}{L_n} \tag{1.8}$$

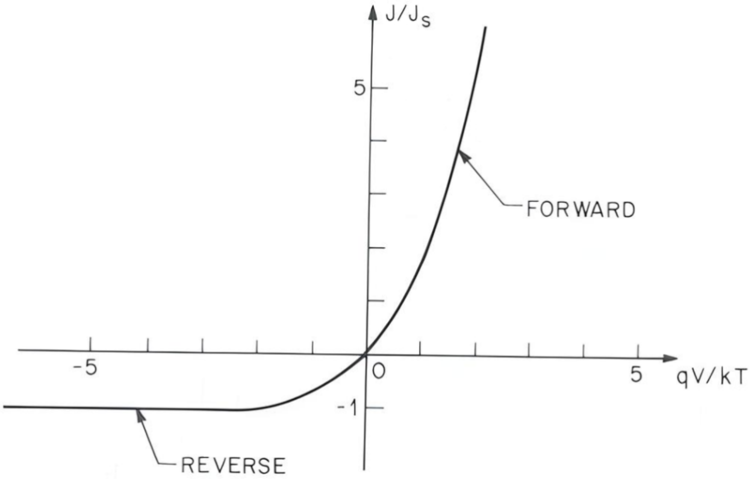

FIGURE 1.7: I-V curve for an ideal p-n junction, according to Eq. 1.7. [16]

Where D_n and D_p are the diffusion coefficients for electrons and holes respectively, L_n and L_p the diffusion length for electrons and holes respectively, and n_{p0} and p_{n0} the density of holes in the n region and the density of electrons in the p region in thermal equilibrium, respectively.

While a forward bias causes the current to increase exponentially with voltage due to the reduction in the energy barrier (as represented in Fig. 1.6), a reverse bias in an ideal p-n junction results in a saturation current equal to I_S, as shown in Fig. 1.7. An increasing reverse bias eventually leads to a point where the electric field in the junction becomes strong enough to give carriers enough energy to promote additional electrons to the conduction band, creating new electron-hole pairs. The newly created pairs can then create more pairs through further collisions. This multiplication mechanism leads to what is known as the *breakdown voltage*, which typically occurs in silicon when the electric fields reaches the order of $3 \cdot 10^5 V \cdot cm^{-1}$ [17].

1.3.2 Capacitance

A reversely biased ideal p-n junction has a charged region known as the depletion region, where very little current flows. Therefore, it effectively acts as a capacitor, and its capacitance can be approximated to that of a parallel plate silicon capacitor:

$$\frac{C}{A} = \sqrt{\frac{q\varepsilon \left|N_{eff}\right|}{2\left(V_{bi} + V\right)}} \tag{1.9}$$

Where N_{eff} is the effective doping concentration in the region with the higher doping, and V_{bi} the built-in potential when no external bias is applied. The capacitance decreases with bias because it essentially depends on the size of the depletion region. Once the external reverse bias reaches the full depletion voltage, the capacitance will reach a minimum value, which depends on the size and geometry of the sensor.

If the inverse square is applied to Eq. 1.9 one obtains:

$$\frac{A^2}{C^2} = \frac{2\left(V_{bi} + V\right)}{q\varepsilon\left|N_{eff}\right|} \tag{1.10}$$

From Eq. 1.10 the effective doping can be extracted from the non-fully depleted region through the slope:

$$\left|N_{eff}\right| = \frac{2}{\frac{d(1/C^2)}{dV}} \cdot \frac{1}{q\varepsilon A^2} \tag{1.11}$$

The $1/C^2$ can also be used to obtain the full depletion voltage. The voltage at which the capacitance ($1/C^2$) reaches its minimum (maximum) value determines the full depletion voltage. This can be determined by calculating the intersection of the linear fits to the plateau region and the initial increasing slope [20]. In Fig. 1.8 an example of a $1/C^2$ curve from a sensor of the type discussed in Chapter 2 is presented. In that example, the full depletion occurs at approximately 4V. The small depletion at low voltages do not deliver reliable measurements, therefore the first initial points are not taken into account.

1.4 Radiation-matter Interactions

Radiation particles can interacting with matter, and if they have sufficient energy, they can promote an electron from the valence band to the conduction band, creating an electron-hole pair. In this section, we consider two different types of radiation: electromagnetic radiation and charged particles. [18]

1.4.1 Electromagnetic Radiation

Electromagnetic radiation can generate charge in the bulk of silicon through various mechanisms, depending on the energy range. For energies ranging from a few eVs to some keVs, the most probable interaction is the photoelectric effect. From a few keV to $1.02MeV$ the Compton effect dominates,

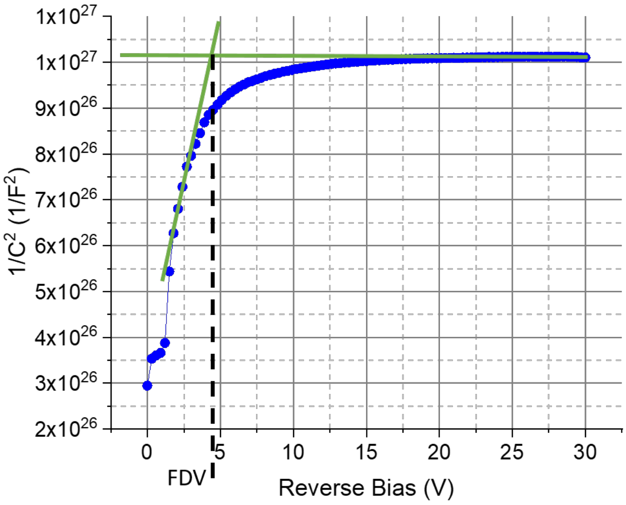

FIGURE 1.8: $1/C^2$ vs bias for a sample sensor further studied in Chapter 2. The full depletion voltage is set by the intersection of the fits to the initial increase and the plateau after full depletion.

and beyond $1.02 MeV$, the pair production occurs, resulting in an electron-positron pair. This thesis focuses on the photoelectric effect, as it is within the range of energies used in the studies. The energy of the electron resulting from the photoelectric interaction can be expressed as:

$$E_e = h\nu - E_b \tag{1.12}$$

Where E_e is the resulting energy of the electron, h the Plank constant coefficient, ν the frequency of the photon, and E_b the binding energy of the electron to the original atomic shell.

A photon traveling through the silicon bulk has an increasing probability of being absorbed along its path, resulting in an attenuating light intensity following the Beer-Lambert law:

$$I(x) = I_0 e^{\alpha x} \tag{1.13}$$

Where x is a point inside the silicon bulk, $I(x)$ is the intensity at such point, I_0 initial intensity, and α is the absorption coefficient. The absorption coefficient depends on the photon's wavelength and the material it interacts with. The $I(x)$ curve for silicon is shown in Fig. 1.9.

The absorption coefficient depends on the interaction cross-section between the atoms and the photons, which varies with the characteristics of

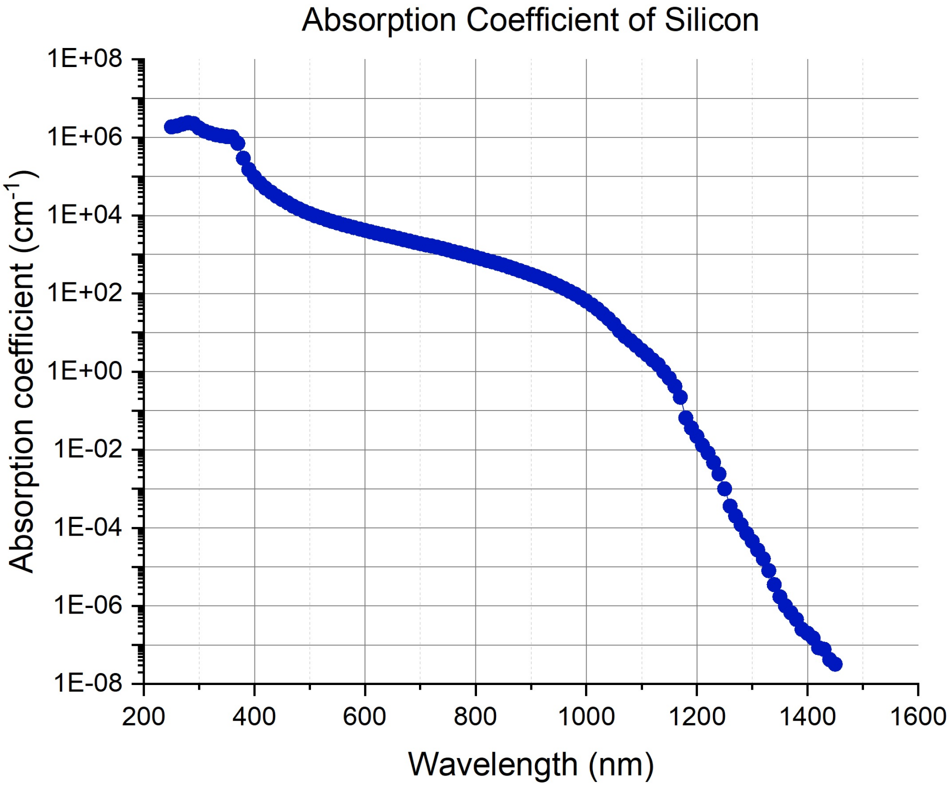

FIGURE 1.9: Wavelength dependence of the absorption coefficient. [21]

the electrons and the type of atoms they are bound to in the lattice. Therefore, the overall absorption coefficient may change according to the doping concentration due to different interaction cross-sections compared to silicon atoms. In Fig. 1.10 we see that at high doping concentrations the transmission decreases, meaning more light is absorbed and the absorption coefficient increases. At low doping concentrations (up to doping concentrations of the order of $10^{19} cm^{-3}$), the effective cross-section of photon interactions with electrons remains nearly unaffected.

1.4.2 Charged particles

When a charged particle traverses a material, it transfers energy to the atoms within the lattice via Coulomb or nuclear interactions with the nuclei or electrons. The mean rate at which a moderately relativistic charged heavy particle loses energy is described by the Bethe equation:

$$-\left\langle \frac{dE}{dx} \right\rangle = Kz^2 \frac{Z}{A} \frac{1}{\beta^2} \left[\frac{1}{2} ln \frac{2m_e c^2 \beta^2 T_{max}}{I^2} - \beta^2 - \frac{\delta(\beta\gamma)}{2} \right] \tag{1.14}$$

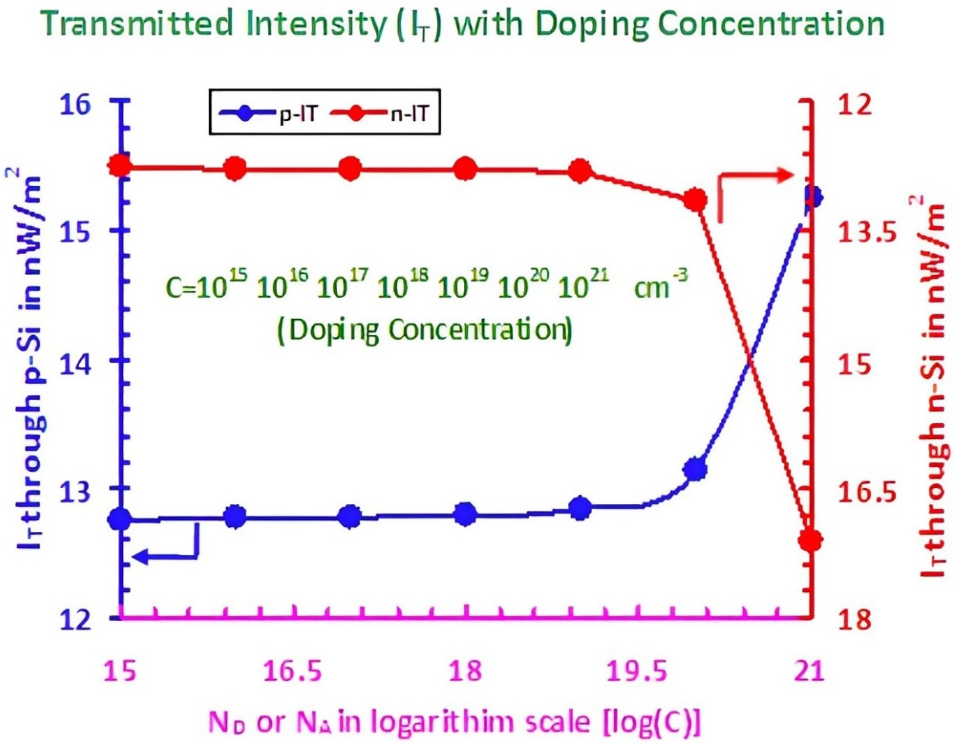

FIGURE 1.10: Light transmission intensity dependence with the doping concentration in silicon with a wavelength of $1550nm$. [22]

Where $\left\langle \frac{dE}{dx} \right\rangle$ is the energy loss rate along the track, $K = 0.307075 MeV \cdot cm^2$, z is the charge of the traversing particle, Z and A are atomic and mass numbers of the absorbing material, $m_e c^2$ is the energy of the electron at rest, β is the particle's velocity (in units of the speed of light), γ the Lorentz factor, I is the excitation energy, and T_{max} is the maximum kinetic energy that can be transferred to an electron by a particle of mass M in a single collision, given by:

$$T_{max} = \frac{2m_e c^2 \beta^2 \gamma^2}{1 + \frac{2\gamma}{M} + \frac{m_e}{M}} \tag{1.15}$$

If the colliding particle is much lighter than the absorbing material, T_{max} can be approximated to:

$$T_{max} = 2m_e c^2 \beta^2 \gamma^2 \tag{1.16}$$

In Fig. 1.11 the rate of energy loss due to ionization of a charged pion traversing silicon is represented, calculated using the Bethe equation. For non-relativistic energies, the energy loss rate is inversely proportional to the

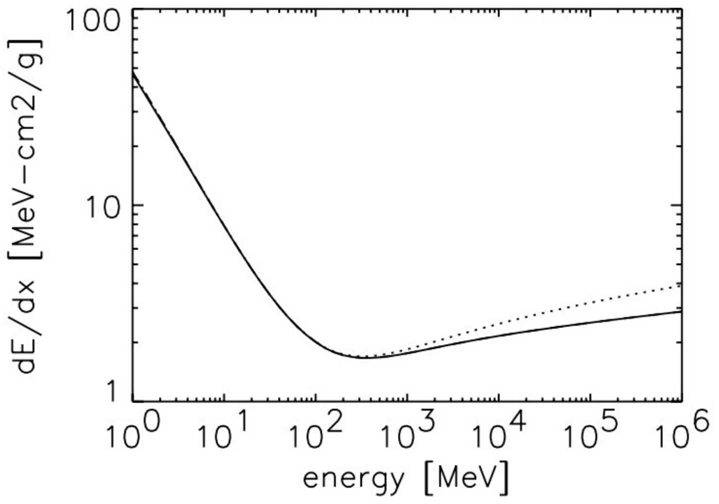

FIGURE 1.11: Rate of energy loss due to ionization as a function of the kinetic energy of a charged pion traversing silicon (effective ionization potential $I = 173eV$) with (continuous line) and without (dotted line) density and shell corrections. [17]

energy, reaching a minimum value. Particles with energies near this minimum value are called Minimum Ionizing Particles (MIP). Beyond the MIP energy, the energy loss rate increases with the particle energy.

1.4.3 Signal Formation in Silicon p-n Junctions

The number of e-h pairs created in a silicon semiconductor depends on the energy required to promote an electron from the valence band to the conduction band, the energy of the ionizing particle, and the total path length through the semiconductor. In silicon, the average energy to create an e-h pair is $3.6eV$. Therefore, for an ionizing particle with an energy loss rate of $\frac{dE}{dx}$ the total number of e-h created along a path of length l in silicon is given by:

$$N = \frac{l \cdot \frac{dE}{dx}}{3.6eV} \tag{1.17}$$

For a MIP-like particle, this results in approximately 75 $e - h\ pairs/\mu m$, which can vary and is often reported as $72 pairs/\mu m$ or 80 $e - h\ pairs/\mu m$.

When a carrier is generated in the bulk, it creates an electrostatic field that induces a current at the electrodes. Therefore, although the charge created in the bulk relates to the signal measured at the electrodes, it is not simply the charge itself. This effect is explained through the Shockley-Ramo's theorem

[23], which states that the current induced to an electrode due to a moving charge is given by:

$$I = q\overrightarrow{v} \cdot \overrightarrow{E_w} \tag{1.18}$$

Where q is the charge, $\overrightarrow{v}$ is the instantaneous velocity, and $\overrightarrow{E_w}$ is the **weighting field**, which is defined as the electric field in the system with no charges present, and all electrodes set to zero potential except for a single electrode set to 1 V. The total current induced in the electrode is then given by:

$$Q = -q\Delta\varphi_w \tag{1.19}$$

Where $\Delta\varphi_w$ is the potential difference of the weighting field in the electrode system which can be found by solving the Laplace equation with boundary conditions of no charges and one electrode set to 1 V.

1.5 Non-ionizing effects on silicon

As discussed in section 1.4 radiation can interact with matter by providing energy to the electrons in the lattice, promoting them from the valence band to the conduction band and thus creating electron-hole pairs. Besides this mechanism, radiation can also transfer energy to the nucleus, potentially displacing atoms from their lattice positions if the radiation particle has enough energy, creating defects as a result. If the particle carries enough energy, it can even initiate a chain reaction, causing multiple defects.

Some of the classified defects include **interstitials** (I), which are atoms located outside a lattice site, and **vacancies** (V), which are the absence of atoms in lattice sites. When two or more vacancies or interstitals are located next to each other, they are called bi-interstitial/vacancy (I^2/V^2), triple-vacancy/interstitial (I^3/V^3), etc. Additionally, a pair consisting of an interstitial and a vacancy is called a Frenkel pair. Additionally, when a charged particle displaces a lattice atom and takes its place,it is referred to as an **impurity substitute**. These defect types are graphically represented in Fig.1.12. [19]

(I^2/V^2), triple-vacancy/interstitial (I^3/V^3)

The amount of induced defects in the silicon bulk depends on the type and energy of the radiation interacting with it. To compare the radiation damage from different types and energies of radiation sources, the Non-Ionizing Energy Loss (NIEL) hypothesis is defined, considering the energy

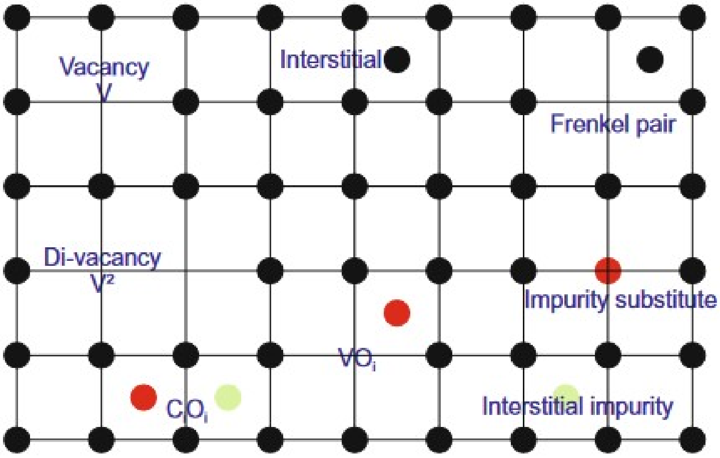

FIGURE 1.12: Graphical representation of the different type of lattice defects that non-ionizing effects can create in the silicon lattice. [19]

transferred in non-ionizing interactions independently of the type and energy of the particle. This energy is calculated using the displacement damage $D(E)$:

$$D(E) = \sum_i \sigma_i \left(E_{kin}\right) \int_0^{E_{R,max}} f_i(E_{kin}, E_R) P(E_R) dE_R \tag{1.20}$$

Where σ_i is the cross-section of the interaction type i, $f_i(E, T)$ is the probability of a collision with a kinetic energy E_{kin}, transferring a recoil energy E_R, and $P(E_R)$ is the Lindhard partition function, describing the fraction of energy used to displace a silicon atom. For example, $P(E_R)$ is 50% for 10 MeV protons and 42% for 24 GeV protons. The standard reference is neutrons with $1MeV$ of energy, thus the standard unit of fluence levels is the *neutron equivalent fluence*, with units of n_{1MeV}/cm^3. A conversion factor κ is used translate radiation damage from any source to the $1MeV$ neutrons:

$$\kappa = \frac{\int D(E)\phi(E)dE}{95MeVmb \cdot \phi} = \frac{\phi_{eq}}{\phi} \tag{1.21}$$

where $\phi = \int \phi(E)dE$ is the total irradiation fluence, and ϕ_{eq} is calculated with units of $\left[\phi_{eq}\right] = n_{1MeV}/cm^2$ (often denoted as n_{eq}/cm^2), by:

$$\phi_{eq} = \kappa\phi = \kappa \int \phi(E)dE \tag{1.22}$$

The collective effect of these defects is the creation of energy levels within the band gap, leading to several macroscopic effects which are listed and discussed below.

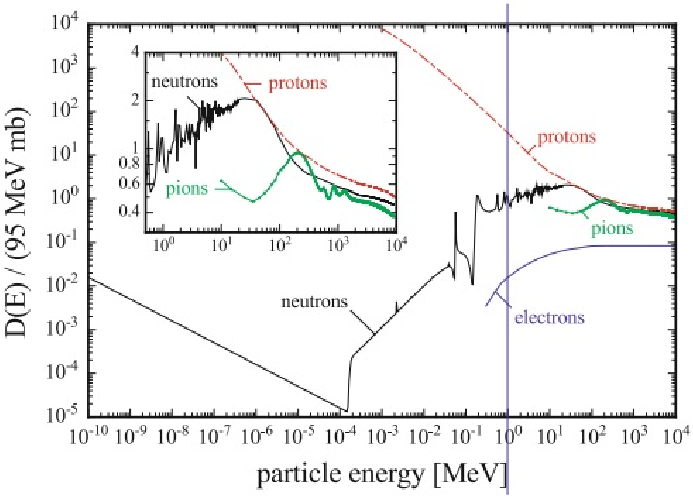

FIGURE 1.13: Displacement damage function $D(E)$ normalized to $95 MeV mb$ for neutrons, protons and electrons. [19]

1.5.1 Increase of depletion voltage

Displacements in the lattice can affect the dopants, such as phosphorus or boron, causing them to change the behaviour as acceptors or donors. For instance, a vacancy-phosphorus complex would shift to a total neutral charge, while phosphorus alone in the depletion region would be positive. Therefore, the effective doping changes with irradiation. For n-type silicon wafers, the effective doping concentration, as shown in Fig 1.14, decreases until it becomes intrinsic silicon, after which it increases with fluence, known as *type inversion* [24]. This inversion is due to the suppression of acceptor and donor activities [25], and the defects themselves acting as acceptors and donors, resulting in a net p-type doping concentration.

Changes in doping concentration affect the voltage required for full depletion, as stated in Eq. 1.5. For n-type silicon wafers, the full depletion voltage decreases with fluence until the substrate inversion occurs, after which it increases as shown in Fig. 1.14.

1.5.2 Increase of leakage current

Defects in silicon, acting as acceptors, change the effective doping of the silicon bulk. Thus, as shown in Eq. 1.7 and Eq. 1.8, the leakage current depends on the density of carriers within the bulk. Therefore, changing the effective doping concentration alters the leakage current. Such an increase can be expressed as:

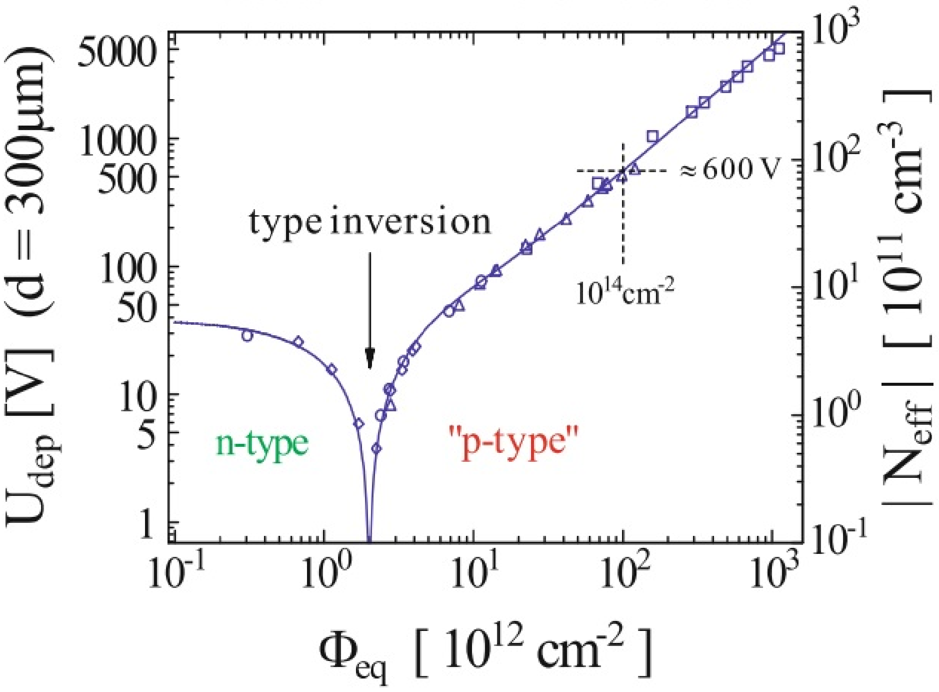

FIGURE 1.14: Depletion voltage and effective doping concentration versus fluence. [19]

$$\frac{\Delta I}{V} = \alpha \phi_{eq} \tag{1.23}$$

where ΔI is the change in leakage current before and after irradiation, V is the active volume, α is the current-related damage rate which is estimated to $4 \cdot 10^{-17}\ A/cm$ [26], and ϕ_{eq} is the fluence level normalized to $1 MeV$ neutrons. For fluence levels higher than $10^{15} n_{eq}/cm^2$, the leakage current curve flattens and does not increase linearly [27].

1.5.3 Decrease of charge collection

Defects induced by non-ionizing effects can act as charge traps, which may capture carriers generated by ionizing particles and release then later. It has been demonstrated experimentally that trapping times have a linear dependence with low fluence levels, which changes at higher fluence levels [28]:

$$\frac{1}{\tau_{eff,e,h}} = \beta_{e,h} \Phi_{eq} \tag{1.24}$$

where β is the traps introduction rate, with

$$\beta = \begin{cases} (4.2 \pm 0.3) \cdot 10^{-16} cm^2/ns & \text{For electrons} \\ (6.1 \pm 0.3) \cdot 10^{-16} cm^2/ns & \text{For holes} \end{cases} \tag{1.25}$$

While trapped charges may eventually be released and collected at the electrode, in particle detection, the measured charge is calculated within a time window. If the trapped charge is released outside the integration time or the preamplifier peaking time, it will not be accounted for and effectively is lost. For example, the bunch crossing time in the LHC is 25ns, much larger than the de-trapping time [29]. Hence, higher defect concentrations lead to more trapped drifting carriers and reduced collected charge. The Charge Collection Efficiency (CCE) is measured as:

$$CCE = \frac{Q_{irr}}{Q_0} \tag{1.26}$$

where Q_{irr} is the charge collected after irradiation, and Q_0 is the charge collected before irradiation.

1.5.4 Annealing

In the same way that silicon atoms can be displaced from their lattice sites, defects in the bulk do not remain immobile. They have the potential to interact with other defects or impurities, creating other defect structures or even cancelling each other, such as in the case of a Frankel pair recombining to fill a lattice vacancy. This process is called *annealing* and its rate is strongly dependent on temperature, since thermal energy allows defects to move through the lattice. The interaction rate increases with higher temperatures, and decreases with lower temperatures.

Annealing effects macroscopic behavior in three phases: a short-term beneficial annealing, where the most mobile defects are displaced and essentially decreases both the leakage current and the full depletion voltage; a stable annealing regime that involves non-mobile defects; and a long-term (or reverse) annealing that increases the space charge concentration [26]. The change in doping concentration with time is illustrated in Fig. 1.15.

In addition to affecting doping concentration, both leakage current and charge collection efficiency are also affected by annealing. For leakage current, annealing always results in a decrease [30]. For CCE, short-term annealing may slightly increase or maintain CCE, while long-term annealing

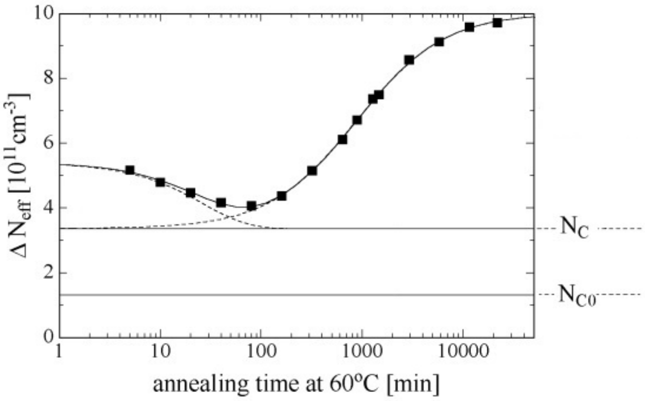

FIGURE 1.15: Variation of the doping concentration versus annealing time. Figure adapted from [26].

decreases CCE due to the increase in full depletion voltage. This is illustrated in Fig. 1.16. Typically, a beneficial annealing is performed on newly irradiated sensors during 80 minutes at 60°C.

1.6 Silicon P-N junctions as Radiation Detectors

A charged particle crossing a reversely biased p-n junction will create e-h pairs that, due to the inherent electric field in the space charge region (Fig. 1.6b), will be separated, with electrons moving to the n-side and holes to the p-side, thus creating a measurable signal described with equation 1.18.

Radiation silicon sensors are built on silicon substrates, with either n-type or p-type doping concentrations, and electrodes placed at both sides of the substrate by means of highly doped regions, where charge is collected. The separation between electrode determines the spatial resolution of the sensor. There are multiple ways in which electrodes can be constructed and segmented which depend on how the electrodes are built.

When spatial resolution is not crucial, strip sensors are used. Electrodes are interconnected in one direction by means of a metal strip, resulting in a higher spatial resolution in one direction then its perpendicular one. Each strip conforms a channel which is connected to the readout. Strip sensors in modern experiments may include from 500 to 800 independent channels [32]. Conversely, when higher spatial resolution is required, pixel sensors are used. They are composed of p-n diodes with very small dimensions which can be easily placed adjacent to each other, creating a matrix of separated regions which enhances the spatial resolution. In this configuration, each

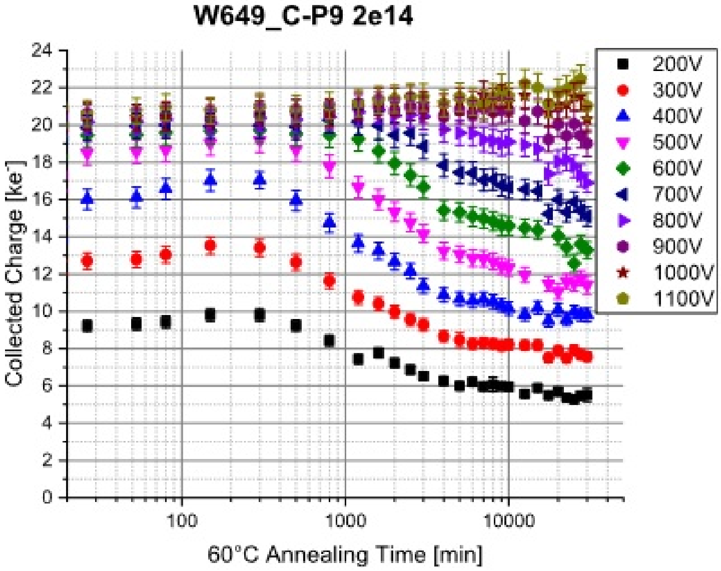

FIGURE 1.16: Variation of charge collection efficiency versus annealing time in a $300\mu m$ thick strip sensor. [31].

pixel conforms an independent channel, hence considerably increasing the amount of readout channels.

In LHC experiments, spatial resolution depends on the section. For inner sections, pixel sensors are required due to necessity for precise spatial resolution when compared to other sections of the experiments. For instance, for the innermost region of the ATLAS tracker, a spatial resolution of $10\mu m$ is required, a characteristic not achievable by strip sensors. Therefore, since this thesis focuses on sensors designed for the innermost sections of future colliders, pixel sensors are used and will be the only ones considered in this thesis.

In high energy physics, when high spatial precision is required, such as for tracking applications, the preferred sensor type is the pixel detector. Pixel detectors are composed of p-n diodes with very small dimensions, which can be easily placed adjacent the each other, forming a matrix of pixels that make up the entire sensor. This sensor is then bump bonded to a readout chip.

Besides the segmentation, there are two main architectures considered for silicon radiation sensors: planar and 3D. In planar sensors, electrodes are implanted on each side of the silicon wafer, whereas in 3D sensors, electrodes are created by etching a column into the silicon wafer and filling it with highly doped poly-silicon, resulting in an electrode that extends the full depth of the wafer.

1.6.1 Planar Sensors

The most basic and most used structure for a silicon radiation detector is obtained by highly doping one side of a high resistivity silicon wafer with donors and the other side with acceptors. Electrical contacts are made by metalizing the highly doped regions for reverse biasing and charge collection. This simple structure is called a PiN diode due to the bulk with low doping concentration (effectively acting as "intrinsic") between a p-n junction. Regardless of whether the less doped silicon region is n-type or p-type it can be biased in reverse mode, creating a depleted region where electron-hole pairs can be generated by an ionizing particle and separated by the electric field.

With this architecture, the volume to deplete is defined as the thickness of the substrate between the electrodes. Depending on the architecture, it can be from some tens of micrometers to a few hundreds of micrometers.

If a layer of high doping is introduced just below the charge-collecting electrode, it can create a region with high electric field that can cause drifting carriers to undergo impact ionization. This results in charge multiplication and intrinsic gain. This type of sensor is called a Low Gain Avalanche Diode (LGAD, Fig. 1.17), first fabricated and designed by the IMB-CNM in 2014 by the Radiation Detector Group (RDG) [33]. LGADs have gained significant interest due to their intrinsic gain, which provides good spatial and excellent time resolution. However, their major drawback is a decrease in gain after high radiation exposure due to the acceptor removal phenomenon discussed in section 1.5.1, which becomes dominant at fluence levels of few times $1 \cdot 10^{15} n_{eq}/cm^2$.

1.6.2 3D sensors

Another architecture was proposed by S.I Parker et. al [34] in which electrodes penetrate the bulk in a cylindrical shape, as shown in Fig. 1.18a. While it maintains the PiN structure, the distance between electrodes is determined by the mask design rather than the wafer's thickness, allowing for much shorter inter-electrode distances

The shorter inter-electrode distance results in shorter travelling distance for drifting carriers, leading to a faster signal collection, which is crucial for time resolution, which will be discussed in section 1.7. Additionally, the shorter drifting distance reduces the probability of carriers being trapped by defect points caused by non-ionizing effects, improving the charge collection

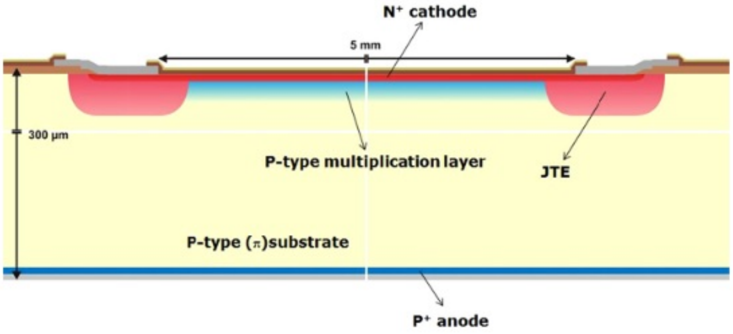

FIGURE 1.17: Schematic representation of the Low Gain Avalanche Detector. The p-type multiplication layer is the highly doped region that leads to impact ionization, resulting in intrinsic gain. The Junction Termination Extension (JTE) separates separates the high electric field from the multiplication layer from nearby pixels, and limits the collected charge to a controlled region. Extracted from [33]
.

and thus radiation hardness. Moreover, since there is a shorter distance to fully deplete the sensor, the full depletion voltage is lower for 3D sensors, resulting in reduced power consumption.

However, the 3D architecture requires a more complicated production technology, with runs usually featuring more than 120 fabrication steps. One of the most critical production steps with 3D detectors is etching the holes in which highly doped polysilicon is deposited to create the electrodes. The technique used is the Deep Reactive Ion Etching (DRIE), which alternates between directional etching with a biased plasma containing a reactant species, typically SF_6, and a passivating step where a passivating species, typically C_4F_8, is deposited to prevent lateral etching [35]. By repeating this cycle, directional etching creates cylindrical holes for the electrodes. However, this method does not yield perfectly smooth cylindrical shapes, often resulting in lateral etching artifacts known as **scalloping**. Another issue is that the end of the column is not perfectly flat, featuring some curvature that affects the column's length and the electric field at the end of the column, which is crucial for sensor performance. Additionally, monitoring DRIE performance is critical to ensure proper column depth. Etching shorter columns increases the drifting distance and depletion volumes, while longer columns can lead to full wafer penetration, causing a short circuit between the front to the backside of the wafer.

Moreover, the non-uniformity of the electric field in 3D sensors affects the timing resolution. Ionizing particles hit the sensor from the top, making the

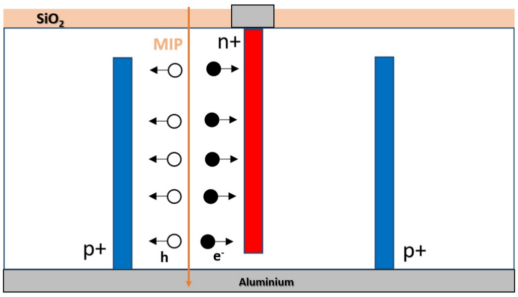

(A)

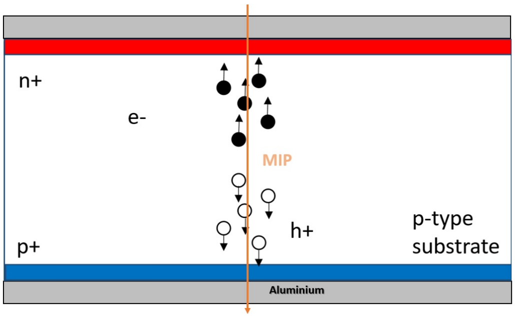

(B)

FIGURE 1.18: Cross section representations for 3D sensors (*A*) and planar sensors (*B*).

actual hit position within a pixel less critical for planar sensors but significant for 3D sensors due to the radial variation of the electric field from the column electrode, resulting in different travel times for carriers depending on the hit position.

1.7 Time Resolution

As discussed in Section 1.1.2, the HL-LHC and future colliders will feature an increased number of events per collision, needing as a result a better sensor capability to resolve events in time (graphically represented in Fig. 1.19).

The total time resolution of a detector mounted on a readout electronics system is given by the contribution of different factors expressed by:

$$\sigma^2 = \sigma_j^2 + \sigma_{tw}^2 + \sigma_{Landau}^2 + \sigma_{distortion}^2 \tag{1.27}$$

where σ_j^2 is the contribution from the jitter, σ_{tw}^2 is the Time-Walk contribution, σ_{Landau}^2 is the Landau contribution, and $\sigma_{distortion}^2$ is the contribution from the distortion of the weighting field.

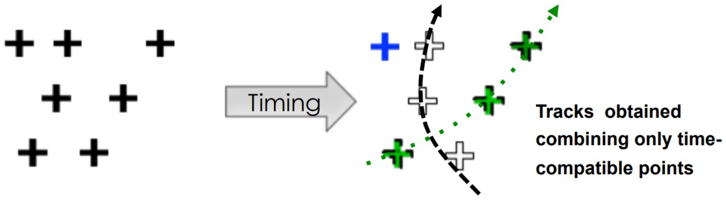

FIGURE 1.19: Graphic representation of the necessity of a good time resolution for silicon sensors. If the tracks are only resolved in space but not in time (left), it is not possible to reconstruct the whole path, resulting in loss of information. [37]

1.7.1 Jitter

The factor contributing to the time resolution due to the jitter is described by [36]:

$$\sigma_j = \frac{N}{dV/dt} \approx \frac{t_p}{(S/N)} \tag{1.28}$$

where N is the RMS noise level, (dV/dt) is the rise of the signal at the output of the amplifier, t_p is the peaking time (the time difference between the signal reaching 10% and 90% of its maximum value), and S/N is the Signal-to-Noise Ratio. A graphical explanation of the jitter is represented in Fig. 1.20.

Hence, the main factors determining how dominant the jitter contribution is:

- The slope of the signal: This depends essentially on the velocity of the drifting carriers, which is influenced by the material and its temperature; and the drift distance, since not all carriers move at the same velocity. Therefore, a longer drifting distance leads to a larger difference in arrival times for carriers moving at different velocities. Additionally, if a signal amplifier has a peaking time slower than the sensor, it may alter the signal rise time.

- The height of the signal: It depends on the total amount of carriers generated by an ionizing particle crossing the sensor. By Ramo's theorem (Eq. 1.18), the current in the electrodes (and the induced charge) depends on the amount of e-h pairs generated in the depleted bulk. Therefore, the reduction of charge collection efficiency after irradiation (discussed in 1.5.3) decreases the signal height, worsening the time resolution. One way to increase the signal height is through internal gain, as in LGADs, which yield excellent time resolution before irradiation.

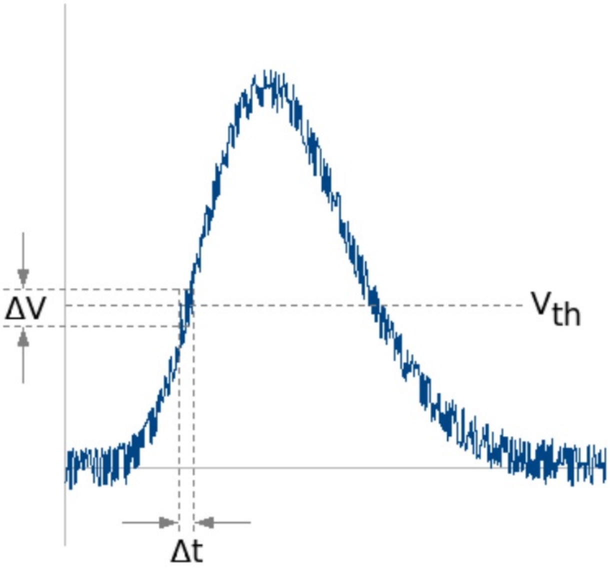

FIGURE 1.20: An uncertainty in the y-axis of dV causes a trigger variation in time of dt, which translates into a decrease in time resolution. [38]

- The noise in the signal: Common sources of noise include pickup noise from the electric network, noise from external radio-frequency waves, electronic noise from amplifiers or any device in the system, and noise from the detector itself due to leakage current or capacitance.

1.7.2 Time Walk

When detecting signals from particles, it is necessary to set a threshold on the voltage signal from the amplifier output to avoid false triggers. Considering two identically shaped signals in the same sensor, but with different heights, the threshold will be crossed at different times despite having the peak at the same timestamp (time of arrival, ToA). This effect is called time walk, graphically represented at 1.21, left.

The Constant Fraction Discriminator (CFD) method can be used to mitigate this effect by setting the ToA of a signal at a certain fraction of the total amplitude instead of the time at which the trigger threshold is crossed. The optimal CFD depends on the shape of the signals, and it is most effective when set at a percentage where the signals statistically have a faster rise time. For instance, for an initially slow signal, any small change at the beginning of the signal would lead to a large time walk, so a CFD set at a higher percentage would be preferable. On the other hand, for an initially fast signal that

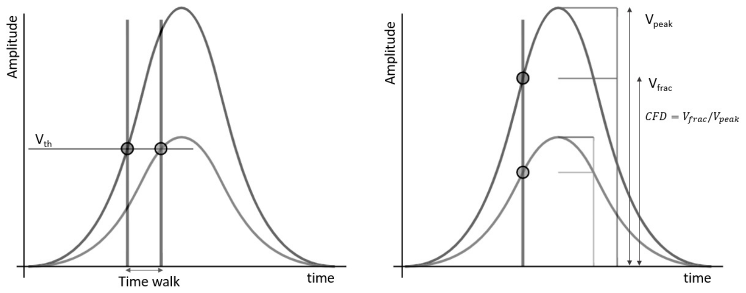

FIGURE 1.21: Representation of the time walk contribution to the time resolution. If only the trigger ToA is considered, different ToAs are given for identcally shaped but differently scaled signals (A). Using the CFD method largely reduces this effect (B). Figure adapted from[39]

.

slows down later, a smaller CFD percentage would be more optimal. Therefore, to mitigate the time walk contribution, a CFD study must be performed to determine the optimal value.

1.7.3 Landau Noise

While the Bethe equation 1.14 describes the average energy deposited by an ionizing particle,the actual deposition is non-uniform. Landau studied this in 1944 [40] for the case of a thin layer. The probability distribution has the shape shown in Fig. 1.22, featuring an asymmetry where the average energy deposited is higher than the most probable value (MPV), with a tail that yields higher signals than a Gaussian distribution. This non-uniform energy deposition leads to a noise-like effect called Landau noise.

For 3D sensors, since the impinging particle travels parallel to the electrodes, the distortion of the signal due to Landau fluctuations is very small and often negligible, as the parallel motion of the ionizing track with respect to the electrode causes drifting carriers to arrive at very similar times to the electrode.

1.7.4 Non-uniform Weighting Field

By Ramo's theorem (Eqn. 1.18), the induced current by a drifting carrier is proportional to the electric charge q, the drifting velocity v, and the weighting field E_w. While the charge is constant, both the drift velocity and the weighting field will change the signal shape. For a consistent signal, both should be as constant as possible, regardless of the ionizing particle's hit position.

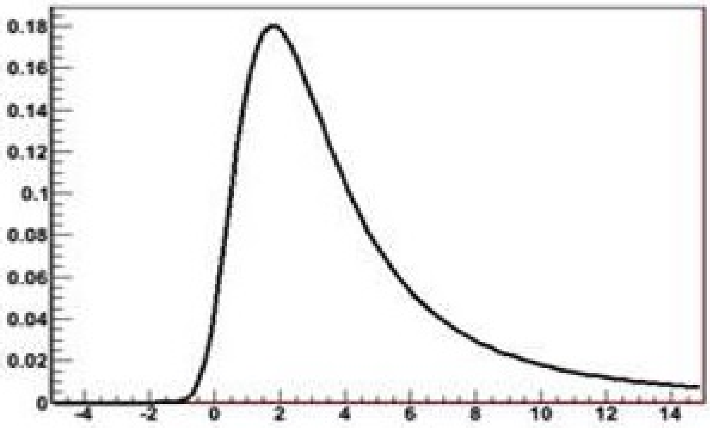

FIGURE 1.22: Probability distribution of energy deposition by an ionizing particle, following a Landau distribution [41]

If carriers reach the saturation velocity quickly in a high electric field, the drift velocity can be approximated as constant. However, the non-uniformity of the weighting field depends on the sensor type. For 3D sensors, this is crucial because, since discussed in section 1.6.2, ionizing particles impinging parallel to the electrodes cause the weighting field to vary strongly with hit position.

1.7.5 Waveform analysis for time resolution measurements

The time resolution of a system composed of two differentiated signals is determined by the sigma from the Gaussian fit to the histogram of the difference in ToA for both signals, expressed by:

$$\sigma^2_{total} = \sigma^2_1 + \sigma^2_2 \tag{1.29}$$

where σ_i represents the time resolution of each sensor. Therefore, if the signals come from two different sensors but one has a known time resolution that can be used as a reference (for instance, in the case of a Sr90 source setup as in Chapter 4), the DUT's time resolution can be determined after acquiring the system's time resolution:

$$\sigma_{DUT} = \sqrt{\sigma^2_{Total} - \sigma^2_{ref}} \tag{1.30}$$

If both signals come from a single sensor (which is the case in chapter 3) or two identical sensors of unknown time resolution (in the case of section 4.2), it can be expressed as:

$$\sigma_{DUT} = \sigma_{Total} / \sqrt{2} \tag{1.31}$$

In either case, waveform analysis can be treated similarly. If both signals come from the same sensor, the script must differentiate both peaks from a single waveform by identifying the maximum or minimum (depending on the signal's sign) in the first or second half of the waveform. Conversely, if the signals come from two different sensors, two separate waveforms are acquired. Therefore, the peaks are identified in each waveform, and the difference in ToA is measured between waveforms.

To reduce the time-walk contribution (Section 1.7.2), the CFD method can be used. To determine the ToA, a quadratic fit is done using the absolute maximum value and its surrounding points (three in each direction) to determine the exact value of the absolute maximum and its exact time. The script then scans for the amplitude crossing a threshold corresponding to a percentage of the signal height (which corresponds to the CFD value) and performs a linear fit with the eight surrounding points, and determines the ToA where the fit meets the threshold set by the specific CFD.

By performing linear fits for different CFD percentages, the best time resolution can be determined. The CFD values used range from 10% to 90% in steps of 10%. For future plots, only the time resolution corresponding to the optimal CFD will be shown.

Other variables studied include:

- Risetime: The time from 10% to 90% of the signal.
- Noise: Calculated as the RMS of the region at the beginning of the waveform where there are no events. The number of points taken may vary depending on the measurement.
- Jitter: Having the risetime, the RMS noise and the signal amplitdes, Eq. 1.28 is used to calculate the jitter contribution to time resolution.
- Charge: Calculated by integrating the signal between points where the waveform is at 10% of the peak height. The conversion from the integral to the collected charge is by means of the relations $Q = \frac{Ampl}{R} \int v(t)dt$.

1.8 Physical models for TCAD simulations

To better understand new technologies or devices, simulations can be performed. By using appropriate models, it is possible to closely replicate the real world behaviour. The software used for this thesis is the TCAD Sysnopsys Sentaurus [42], which is widely used for semiconductor technologies.

A TCAD simulation starts with the definition of the device, achieved through the Sentaurus Structure Editor. In it, the materials, their sizes, their locations, and the doping profiles at each point are defined. For the software to perform calculations, each region must be discretely divided into small regions so that the software can interpolate values from one small region to the adjacent ones. This process is called *meshing*, and it is a complex and crucial topic. To obtain accurate results, fine meshing is required, but it cannot be infinitely small due to the computing time being tied to the number of meshing points. Therefore, the meshing strategy must be carefully studied for each case. The meshing points should be smaller at regions where relevant parameters change significantly over small distances (for example, near an electrode, where the doping concentration decays as a Gaussian), and larger in regions where less significant phenomena happen, such as between electrodes.

After the meshing is defined, Sentaurus Device can load the modelled sensor created by Sentaurus Structure Editor and solve the Poisson equation with contour conditions, including a bias applied at the electrodes. Many relevant physical magnitudes can be simulated, such as the electric field, carrier mobility, current at the electrodes at different voltages (I-V curves), or the simulation of an ionizing particle crossing the device.

To accurately calculate such variables, it is crucial to use appropriate physical models that recreate the environment of the carriers in the device, such as mobility models, generation and recombination in the sensor or any dependence on the doping concentration. In this section, the physical models used for the simulations are presented and discussed, while more details on the mathematical representation and their coefficients can be found in appendix A

1.8.1 Mobility models

To properly simulate the behavior of a device, it is crucial to take into account the various factors that affect carriers behavior. This can be achieved by using some of the mobility models available in TCAD Sentaurus software. When multiple mobility models are used, the total mobility results from the Mathiessen's rule:

$$\frac{1}{\mu} = \frac{1}{\mu_1} + \frac{1}{\mu_2} + \cdots \tag{1.32}$$

Where μ is the total mobility and μ_1, $\mu 2, \cdots$ are the different mobility contributions from bulk, surface or thin layers. In our case, the models used are the doping dependence model, the Lombardi, high field saturation and carrier-carrier scattering:

- Impurities in semiconductors act as scattering points in the lattice, degrading the mobility of the carriers. Masetti et al [43] extracted the relationship between mobility and doping concentration, whether provided by donors or acceptors.
- Since the transverse electric fields at semiconductor interfaces are usually high, carriers are forced to interact with acoustic surface phonons and surface roughness. For this, the Lombardi model is used.
- At a sufficiently high electric field the velocity of carriers is not proportional to the electric field, but saturates to a certain value v_{sat}. This behaviour can be explained by the Canali model, which models the mobility in function of the temperature, fitted up to $430K$ [44].
- At high carrier concentrations, the carrier-carrier scattering degrades mobility and cannot be neglected. It can be described by the Conwell-Weisskopf model, which provides a relationship between the velocity of the carriers and both the carrier concentrations and the temperature. [45]

1.8.2 Generation-recombination models

Electron-hole pairs in semiconductors have multiple mechanisms to be created or eliminated, and taking them into account is important to have a correct electrical behavior representation.

- Defects and dopants in the crystal lattice introduce extra energy levels within the band gap, which are called deep energy levels when close to the Fermi level. These additional energy states facilitate carrier transitions between bands, which effectively acts as a recombination process. This mechanism is known as Schockley-Read-Hall recombination.
- When an electron transitions from the conduction band to the valence band, the released energy may be transferred to another electron, which

then relaxes through phonon emission. This process is called Auger recombination, and is particularly relevant at high carrier density regions due to the increase of interaction probability.

- When the space charge region width exceeds the mean free path of a carrier, an avalanche effect may occur, where an induced drifting carrier produces additional carriers along its path. This process is known as the Avalanche effect or Impact ionization.

1.8.3 Effective Intrinsic Density

At high doping levels, the band gap narrowing must be considered. The band gap for a given temperature can be expressed as the difference between the band gap energy at zero temperature and a temperature-dependent term [46]:

$$E_g(T) = E_g(0) - \frac{\alpha T^2}{T + \beta} \tag{1.33}$$

The total effective band gap, accounting for the temperature dependence and doping concentration variation, can be expressed as:

$$E_{g,erff}(T) = E_g(T) + \delta E_{bg} \tag{1.34}$$

The model used for δE_{bg} is the old Slotsboom model, which was fitted using a transistor built on a p-type wafer.

Chapter 2

3D Double Sided n-on-n characterization and technology

The n-on-p sensor configuration is widely employed in sensor architectures, primarily due to the superior mobility of electrons with respect to holes, being fastest drifting carriers. Electrons are collected at the n-electrode, which is subsequently connected to the readout electronics. For the p-n junction to be located at the n+ electrode, the bulk must be p-type. This is crucial because, with an n-type bulk, the electrostatic potential barrier between the bulk and the n+ electrode is lower, resulting in higher leakage current compared to the n-on-p configuration.

However, must be considered that, as discussed in section 1.5.1, n-type substrates undergo substrate inversion after a certain level of irradiation due to non-ionizing effects. As shown in Fig. 1.14, the full depletion voltage of n-type wafers decreases until substrate inversion occurs. This characteristic allows them to potentially operate at lower biases than their n-on-p counterparts.

N-type wafers as substrates for silicon sensors have already been used in experiments at the LHC. For instance, they were employed in the VELO detector for the LHCb experiment, where strip sensors with a thickness of 300 μm and n-on-n planar architecture were utilized. Additionally, two n-on-p sensors were employed as candidates for future upgrades [47]. Fig. 2.1 shows the measured effective depletion voltage over time against the equivalent fluence level of radiation. A noticeable decrease in the depletion voltage of the sensors is observed until substrate inversion occurs. In contrast, for the n-on-p configuration, the depletion voltage increases with fluence, reaching levels up to approximately $40V$ higher than the n-on-n configuration, at a fluence of $20 \cdot 10^{12}$ $MeV\ n_{eq}$.

In this chapter, we explore the behavior of 3D n-on-n sensors produced at the clean room facility from the Centre of Microelectronics of Barcelona

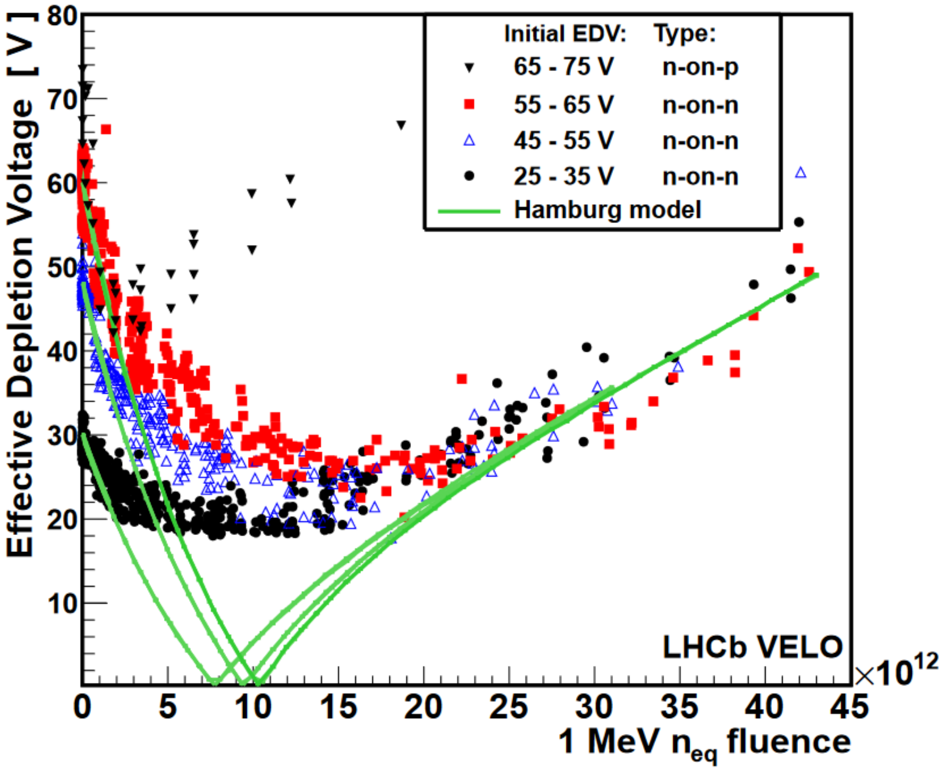

FIGURE 2.1: Depletion voltages versus fluence level, separated according different initial depletion voltages. Extracted from [47].

(IMB-CNM). Our primary focus is on electric characterization, involving a detailed analysis of I-V curves and C-Vs both before and after an irradiation campaign, during which the sensors were exposed to neutron radiation. The following chapters, Chapter 3 and Chapter 4, will extend this study. Chapter 3 will employ the Transient Current Technique (TCT) to measure their response to an infrared laser, while Chapter 4 studies their performance to a Sr90 source.

2.1 N-on-N technology and samples

The studied sensors are of 3D architecture from the run 10339 fabricated in the clean room in IMB-CNM, and are built on 200μm thick, high resistivity, n-type wafers. The columns are 180μm deep and have a diameter of 8μm in a double sided process, meaning that n-electrodes and the p-electrodes are etched from opposite sides of the wafer. A cross section of the sensors is shown in Fig 2.2.

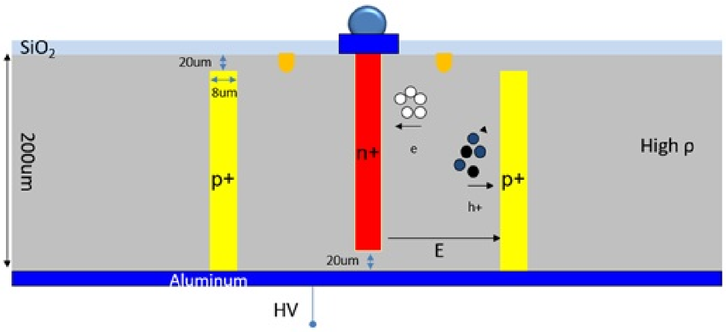

FIGURE 2.2: Schematic cross section of the 3D n-on-n architecture studied in this work.

Label	Geometry	Size (μm)	Pixel array
$1-X$	$50x50\mu m$, 1E	$20.42x10\ mm^2$	$400x192$
$2-X$	$25x50\mu m$, 2E	$20.42x10\ mm^2$	$384x200$
$3-X$	$25x100\mu m$, 1E	$20.42x10\ mm^2$	$384x200$
$5-X$	$50x50\mu m$	$6.2x6.2\ mm^2$	$100x100$
$6-X$	$50x50\mu m$	$4.0x4.0\ mm^2$	$50x50$
$7-X$	$25x50\mu m$	$6.2x6.2\ mm^2$	$200x100$
$8-X$	$25x100\mu m$	$6.2x6.2\ mm^2$	$200x50$

TABLE 2.1: List of the samples featured in the run 10339 and some of their key characteristics.

The run features a variety of samples, most notably RD53 sensors, with both $50x50\mu m$ and $25x100\mu m$ pixel pitches. The latter can have two configurations: a single pixel connected to one (1E) or two (2E) electrodes. Additionally, test devices are featured such as pad diodes of 50x50 and 100x100 pixels arrays, with pixel pitches of $50\mu m\ x50\mu m$, $25\mu m\ x\ 100\mu m$ and $25\mu m\ x\ 50\mu m$. Pad diodes are used to understand sensor behavior on a smaller scale to predict their performance in larger scale. Table 2.1 shows a list of the sensor and some their geometrical characteristics.

Test structures of a single pixel surrounded by eight pixels in an orthogonal geometry with a pitch of $55\mu m\ x\ 55\mu m$ are also included. These samples are crucial for time resolution studies because time resolution is affected by sensor capacitance by introducing noise. Connecting multiple pixels is equivalent to connecting capacitors in parallel, thereby increasing the total capacitance.

To study the large scale samples, such as RD53B sensors, without the need of specific ASICs or complex systems, a temporary metal deposition process is typically employed. This process consists of the deposition of two metal layers, titanium and aluminium, which cover the sensors entirely, which facilitates I-V and C-V measurements by providing a single contact for all electrodes. For RD53B sensors, no temporary metal was deposited, so only single pixels could be chatacterized.

For pad diodes (devices 5-X, 6-X, 7-X and 8-X), instead of the temporary metal, a highly doped layer of polysilicon is deposited to short all electrodes. Using highly doped polysilicon allows for laser measurements, as photons would be reflected on a metallized surface and no signal could be induced.

2.1.1 Re-metalization for the small test structures

For some test structures, the metalization on the contact pads was insufficient, having as a consequence no contact point for measurements. This was particularly significant for devices irradiated at the highest fluences, which are the most relevant for this thesis. Scanning Electron Microscope (SEM) images before and after re-metalization are shown in Fig. 2.3. Fig. 2.3-A shows that there was nearly no metal before being processed.

To repair them, a Focus Ion Beam (FIB) deposition was performed using platinum mixed with a low concentration of carbon. The result of the deposition is shown in Fig. 2.3-B. I-V measurements performed after the deposition showed a short between the pads for the central electrode and the guard ring. Mounting the sensors to a PCB for testing with the TCT setup (explained in Chapter 3) showed that the measured current versus applied voltage behaved like a resistor, hence the current was not coming from the sensor's bulk. A SEM image showed a halo of metal around the pads (Fig. 2.3-C). Typically, FIB processes deposit material in areas spanning a few microns, but the size of the pads was of a hundred microns. Therefore, a higher ion flow was needed to depost within a feasable timescale, which increased the amount of scattered ions.

To separate the channels, an etching step was performed, with the result shown in Fig. 2.3-D. Two perpendicular strips represent the etching performed. The resulting I-V curves will be shown in Section 2.2.2, which showed that while it was possible to measure separate currents from both pads a noisy current was measured, most likely due to the combination of poor contact and the alteration of the electric field by the metal halo.

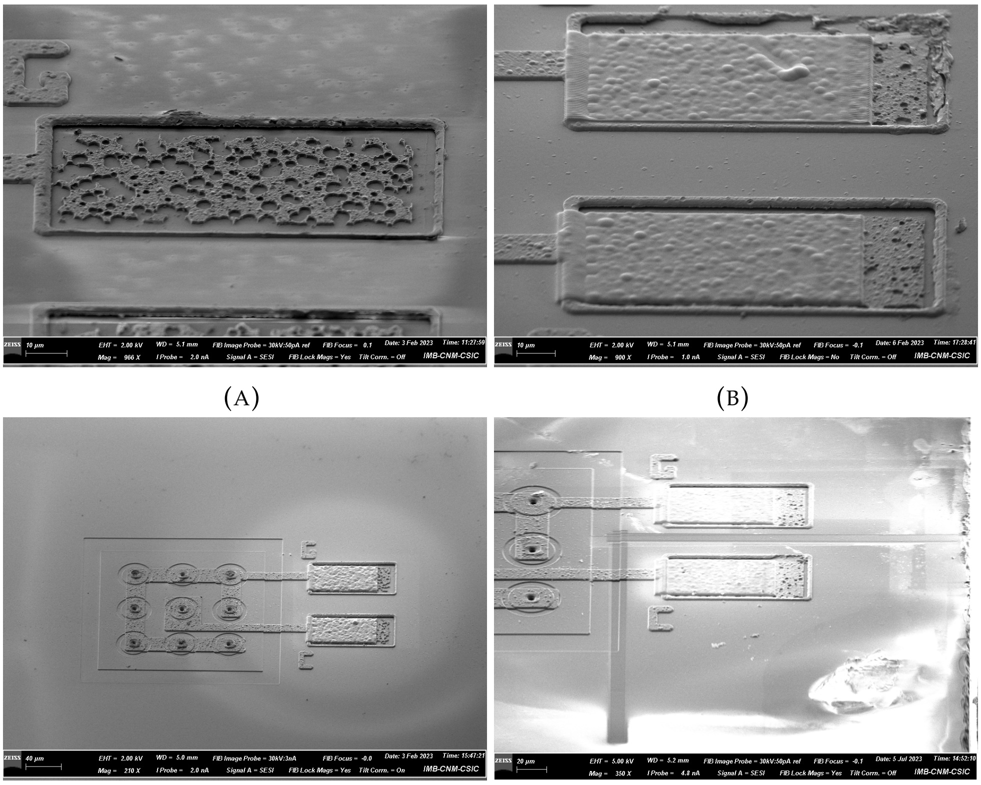

(A) (B)

(C) (D)

FIGURE 2.3: SEM images of the pads for the small test structures, showing that (A) there was no metal before depositing with FIB, (B) how the deposited metal looks like, (C) that there is a thin layer of metal around the area where the metal is deposited, and (D) the etching in the shape of strips to separate the channels.

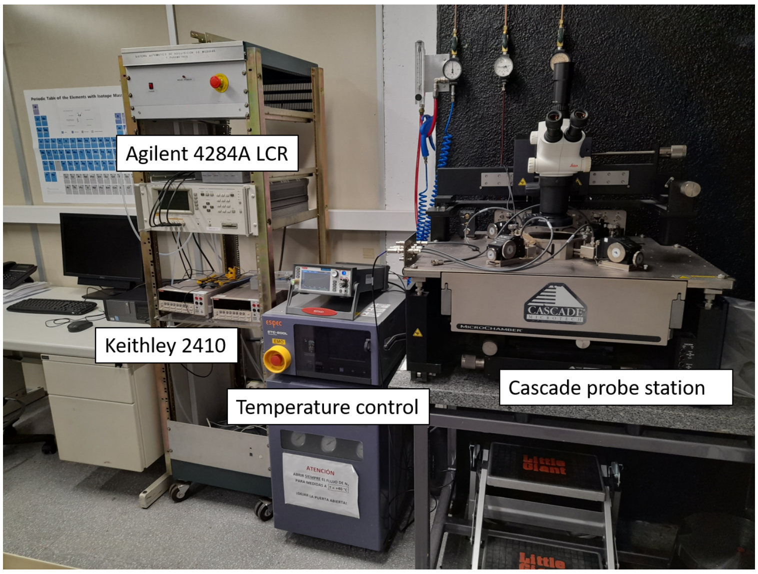
Agilent 4284A LCR
Keithley 2410
Temperature control
Cascade probe station

FIGURE 2.4: Image of the probe station setup at CNM, highlighting the different components.

2.2 Electrical characterization

Current-Voltage (IV) curves were obtained using the Cascade probe station at the Radiation Detectors Laboratory at CNM. It features probes that can be finely moved to make contact with the metal pads of each Device Under Test (DUT). They are connected to a Keithley 2410, which provides the necessary bias to the sensors and reads the output current. The power sources are remotely controlled via software that records the current for each voltage and can average multiple measurements per voltage to reduce noise contributions.

During biasing, the ground is set at the backside of the device, while the bias is applied through the probe at the contact pads, requiring a positive voltage to reversely bias the sensor. The probe station also includes an ESPEC ETC-200L, which regulates the temperature of the chuck, capable of ensuring a constant temperature -20ºC, which is the target for low temperature measurements. Additionally, a nitrogen gas flow kept maintained throughout all measurements to prevent humidity from interfering. While relative humidity does not change the leakage current, it affects the breakdown voltage of 3D sensors. In a humid enviornment, negative charges accumulate over the oxide region and aggregate around electrodes of the opposite sign [48]. Simulations have shown that the presence of a greater surface charge leads to a larger electric fields, lowering the breakdown voltage [49].

In addition to the IV curves, Capacitance-Voltage (CV) measurements were also carried out using the probe station. An Agilent 4284A LCR meter has been used together with a Keithley 2410, conected to a decoupling system that separates the sinusoidal signal from the LCR from the applied bias voltage. For all measurements, the AC voltage from the LCR was set to 500mV with a frequency of 10kHz, if not stated otherwise. An image of the probe station setup is shown in Fig. 2.4.

2.2.1 Before irradiation

Since no temporary metal was deposited on the RD53B sensors, measurements could not be carried out shorting all the pixels, so only a single pixel could be measured at a time. Therefore, results from the I-V curves are presented as quantities per pixel, rather than for the entire device. This approach make results more easily comparable across different device types.

The I-V curves for the RD53B sensors are presented in fig 2.5 as the current at room temperature for a single pixel. As expected for an n-on-n sensor, the

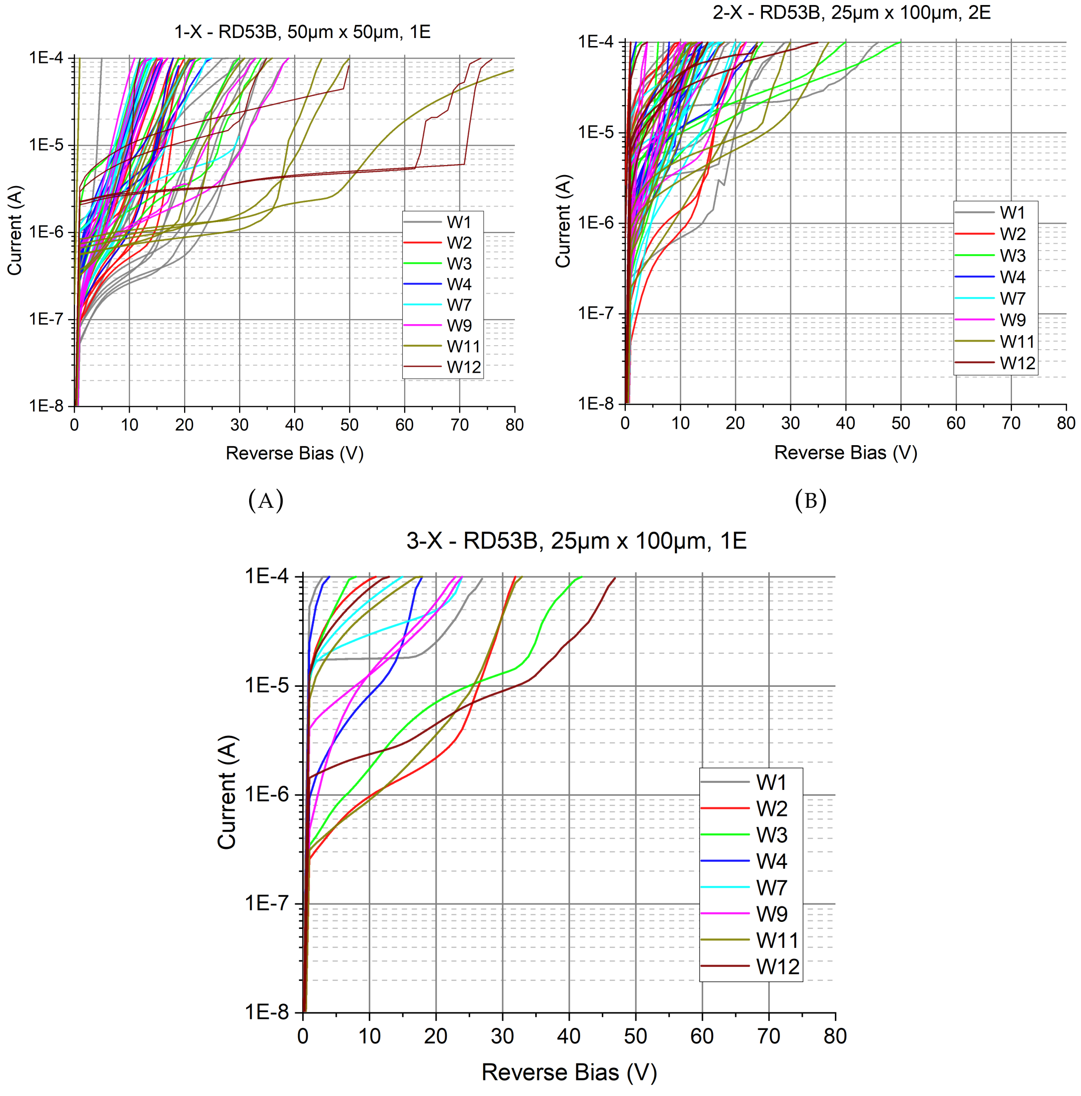

(A)

(B)

(C)

FIGURE 2.5: I-V curves measured at room temperature ($T = 20°C$) for the RD53B sensors of types 1-X (A), 2-X (B) and 3-X (C).

leakage current is high due to the lower energy barrier at the electrode-bulk junction.

The breakdown voltage varies depending on the sensor, ranging from just a few volts to approximately 70V in the highest case. However, a 3D detector can be fully depleted with just a few volts, making it operational. Despite the high leakage current being a concern it should be partially mitigated after irradiation due to substrate type inversion. Full depletion is shown in Fig. 2.7, where the $1/C^2$ curves are shown for devices 5-X and 8-X from wafers 1, 2 and 11. Both sensor types show a initial rapid increase in $1/C^2$ followed by a very slowly increasing curve given by the slower depletion at the backside.

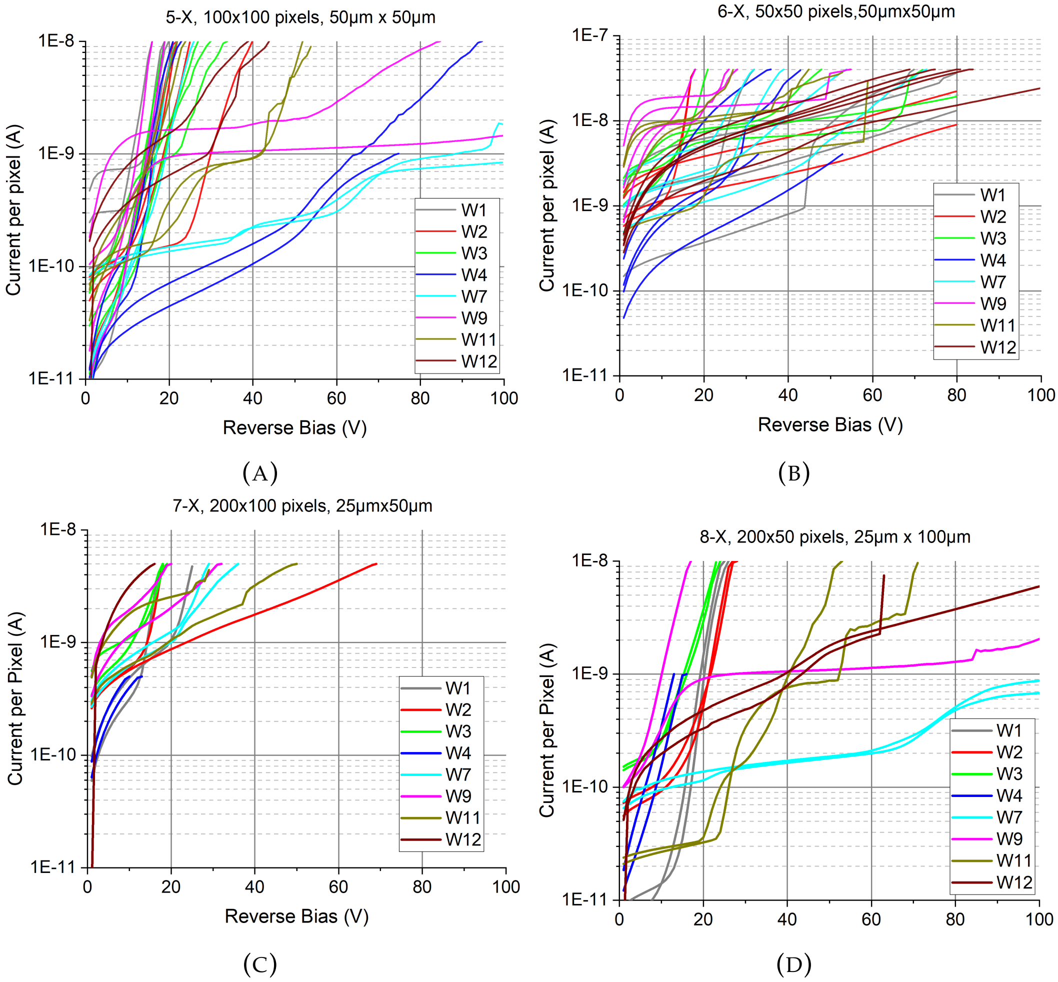

(A) (B) (C) (D)

FIGURE 2.6: I-V curves measured at room temperature ($T = 20°C$) for the pad diode arrays of 5-X (A), 6-X (B), 7-X (C) and 8-X (D).

In [50], simulations showed that a higher bias is necessary to fully deplete around the p-stop, hence having a slow decrease of capacitance after lateral depletion. Therefore, full lateral depletion is reached with less than 5V.

The I-V curves for test pad diodes are shown in Fig. 2.6, where currents are presented per pixel instead of the total measured current. When comparing the I-Vs from the RD53B sensors (1-X to 3-X) with the pad diodes (5-X to 8-X), the former exhibit larger leakage current. This is attributed to having floating neighbouring pixels when only one is biased, hence collecting carriers generated further away from the measured pixel, increasing the current as a result. Therefore, the current per pixel for sensor a fully covered with temporary metal would be lower.

In some cases of high leakage current, the main contribution comes from surface current due to defects or imperfections from fabrication steps. Since the temperature dependence to leakage current (Eqn. 1.7) is given by the

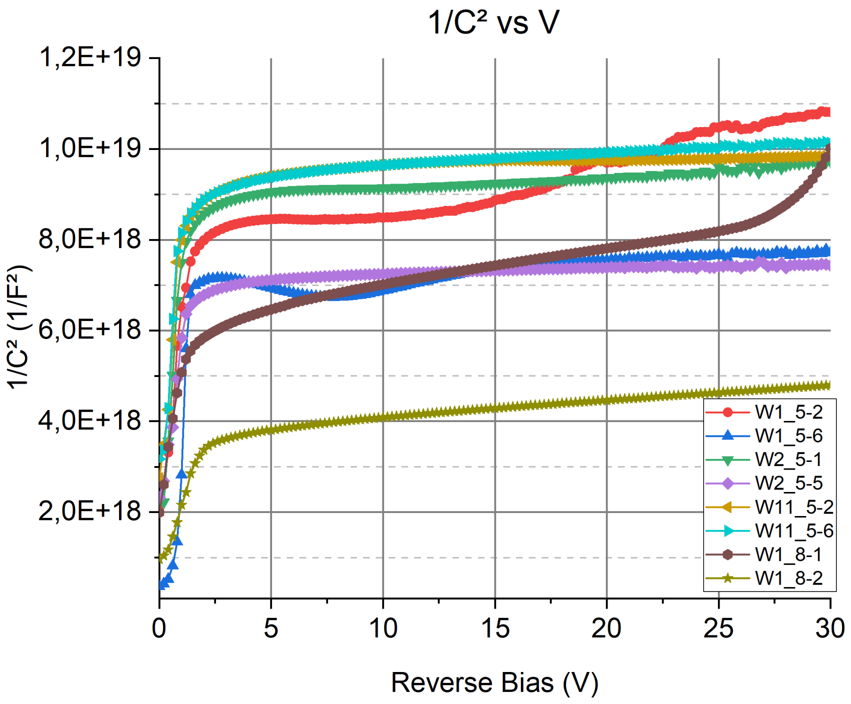

FIGURE 2.7: C-V curves of 5-X and 8-X devices, with the capacitance represented as quantity per pixel.

bulk contribution, a high leakage current that does not vary with temperature indicates a surface current. In Fig. 2.8 the I-V curves for 6-X and 8-X pad diodes are presented. Comparing them with Fig. 2.6-B and Fig. 2.6-D, the leakage current is an order of magnitude lower at lower temperatures, indicating that it is a bulk current.

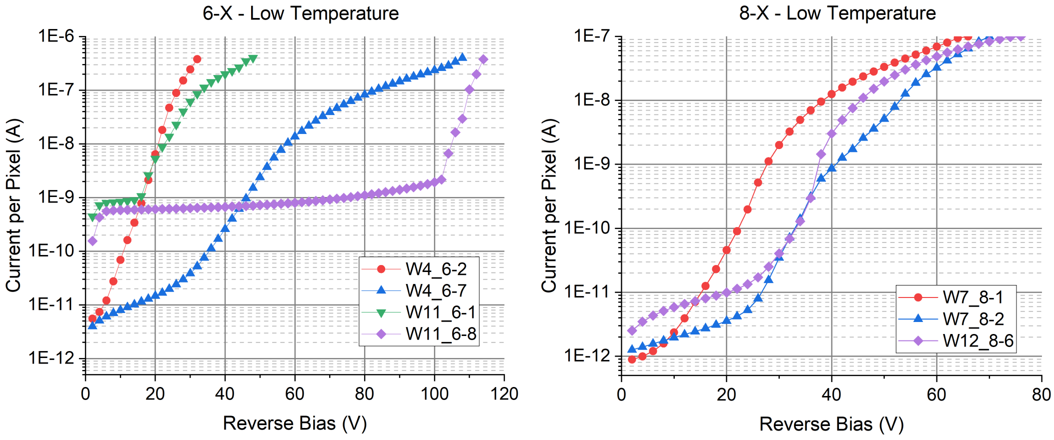

(A)

(B)

FIGURE 2.8: I-V curves taken at low temperature ($T = -20°C$) for the sensors of types 6-X (A) and 8-X (B).

For some devices, I-Vs curves with forward bias were recorded to verify that the behavior is that of a diode. The results are presented in Fig. 2.9, where the curves show an exponential behavior, appearing as linear curves in a logarithmic scale. Thus, they behave as diodes when the bias is applied in the forward mode.

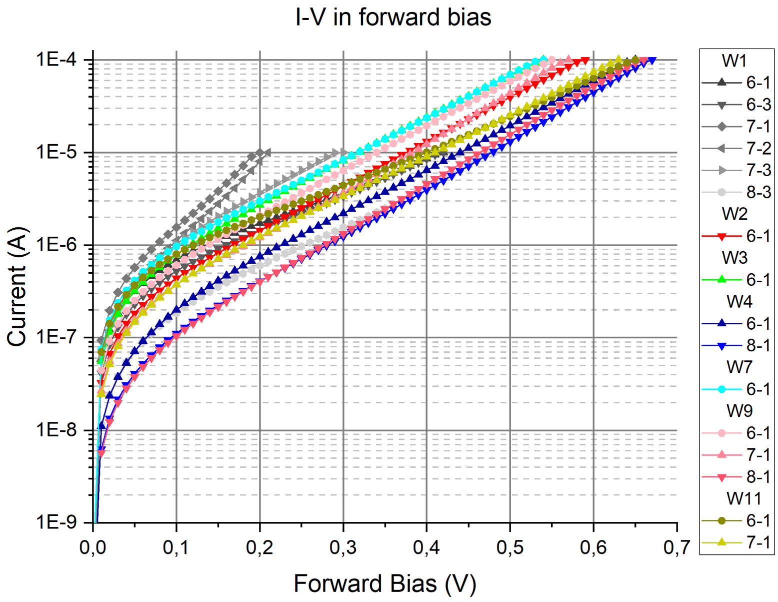

FIGURE 2.9: I-V curves of some diode arrays with different geometries and sizes from different wafers.

I-Vs curves were also taken for test structures with a single central column surrounded by eight neighboring pixels. The curves are presented in Fig. 2.10-B. When compared with the curves taken for 1-X to 3-X, the leakage current is slightly smaller, with a higher breakdown voltage. This is consistent with the fact that for the RD53B the surrounding pixels are floating, resulting in current from further distances, whereas for the small test structure there are at least eight working pixels surrounding it. However, the current per pixel is higher than that of the larger area diode arrays, indicating a surface contribution, likely due to a higher edge-to-area ratio.

2.2.2 After irradiation

To study the behavior of the senors after being irradiated, an irradiation campaign was carried at the nuclear reactor in the Jožef Stefan Institute (JSI) [51] using thermal neutrons. The list of sensors included 1-X, 2-X, 6-X, 8-X and some of the small test structures with a single central pixel. They were irradiated with up to the $1 MeV$ neutron equivalent fluence levels of $1 \cdot$

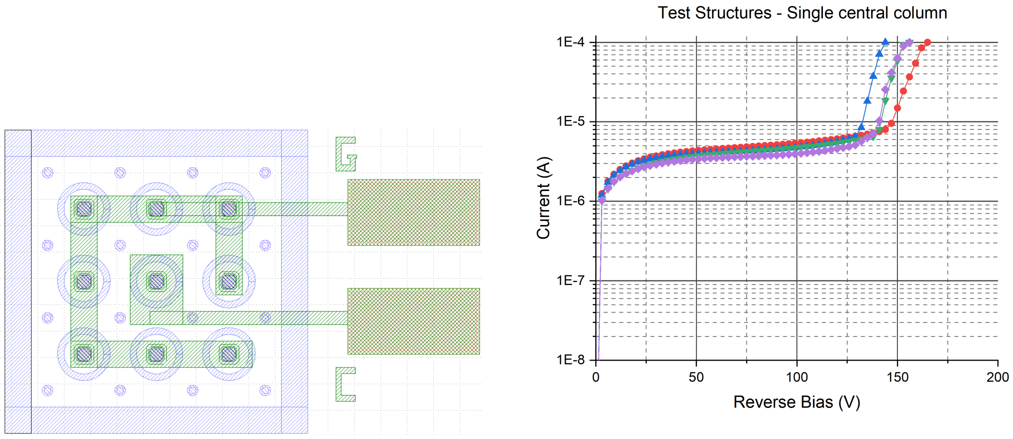

(A) (B)

FIGURE 2.10: Mask design for the test structures (A) and the I-V taken from a few samples from wafer 4 (B)

$10^{14} n_{eq}/cm^2$, $1 \cdot 10^{15} n_{eq}/cm^2$, $5 \cdot 10^{15} n_{eq}/cm^2$, $1 \cdot 10^{16} n_{eq}/cm^2$, $5 \cdot 10^{16} n_{eq}/cm^2$ and $1 \cdot 10^{17} n_{eq}/cm^2$. As a reference, the expected accumulated equivalent fluence level at the end of the HL-LHC upgrade is of $2 \cdot 10^{16} n_{eq}/cm^2$, while for the innermost part of the FCC, it is $8 \cdot 10^{17}$ [52]. Therefore, this work studies radiation damage levels before and beyond the currently expected limits for the HL-LHC, though not for the most extreme cases of the FCC. After irradiation, a beneficial annealing process was applied to all sensors by heating them for 60 min at a temperature of 80 $°C$.

To accurately measure the I-V characteristics of the irradiated sensors, it is necessary to perform the measurements at low temperatures. Defects act as generation points and introduce carriers which contribute to the leakage current, which can get compensated with a lower temperature. Thus, all measurements for irradiated sensors were carried out at a temperature of -20 $°C$ with a constant nitrogen gas flow. This is also the same order of magnitude as the operational voltage in particle accelerators, being $-25°C$ in the ATLAS ITk, for instance [6].

I-Vs for 1-X, 2-X devices are shown in Fig. 2.11, and for 6-X and 8-X in at Fig. 2.12 at various fluence levels. Due to an issue during shipping, the 1-X and 2-X sensors irradiated at fluence level of $5 \cdot 10^{16} n_{eq} cm^{-2}$ were damaged and could not be measured. For the 6-X and 8-X devices, the I-Vs at low temperature before irradiation are also plotted for easier comparison.

For 1-X and 2-X sensors, the leakage current shows a slight increase with fluence but maintaining the same order of magnitude. As discussed in section 1.5.2, there is a saturation of the leakage current versus fluence at levels

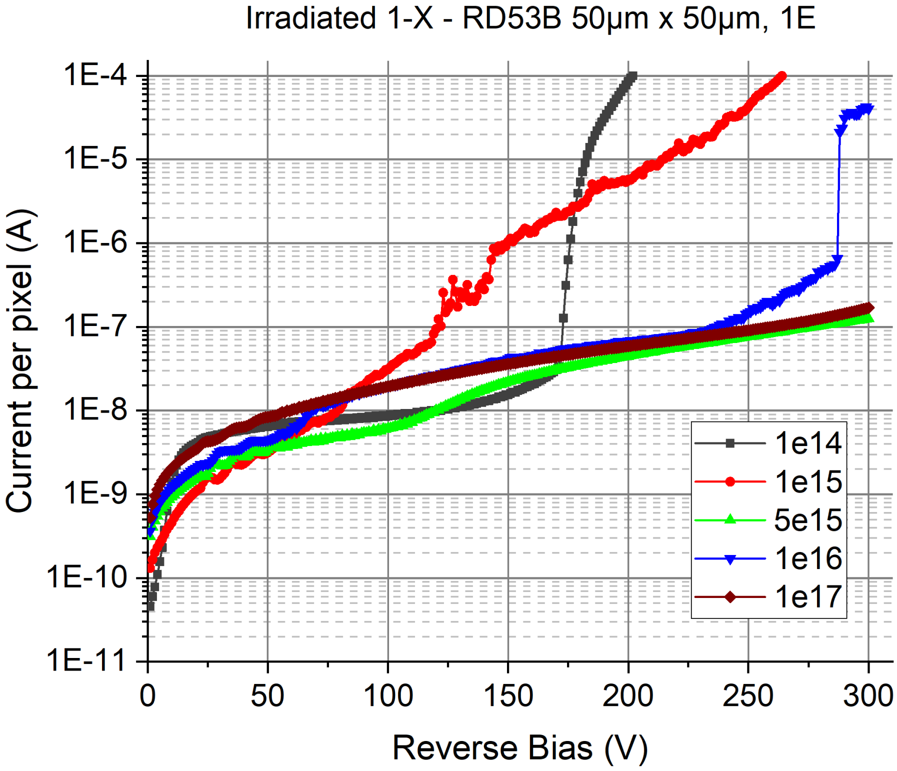

(A)

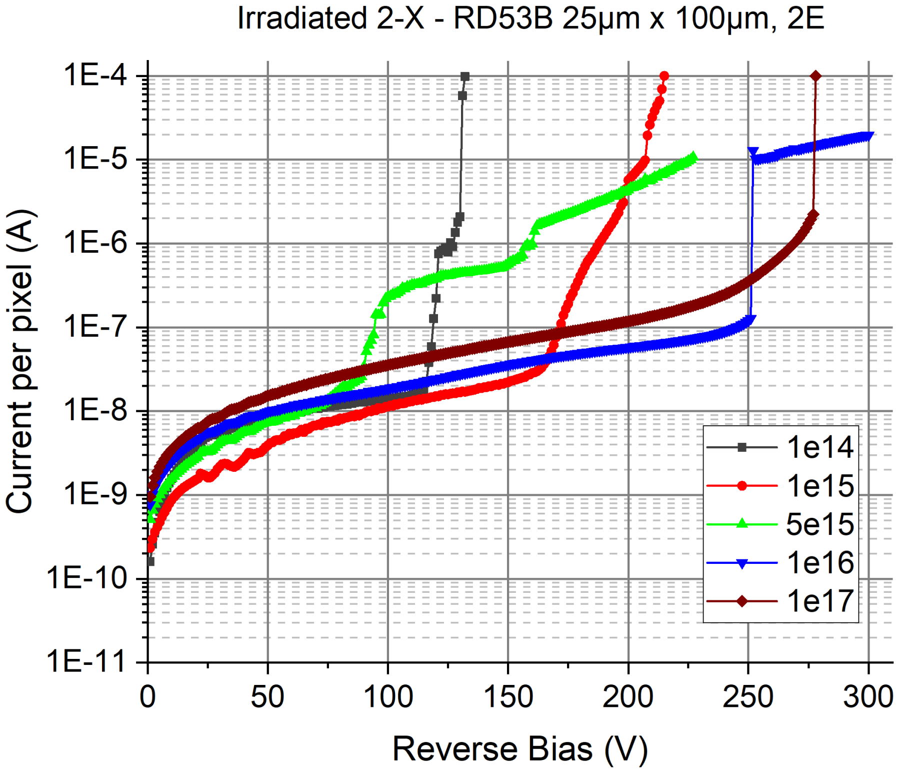

(B)

FIGURE 2.11: I-V curves for the 1-X (A), 2-X (B) at different fluence levels.

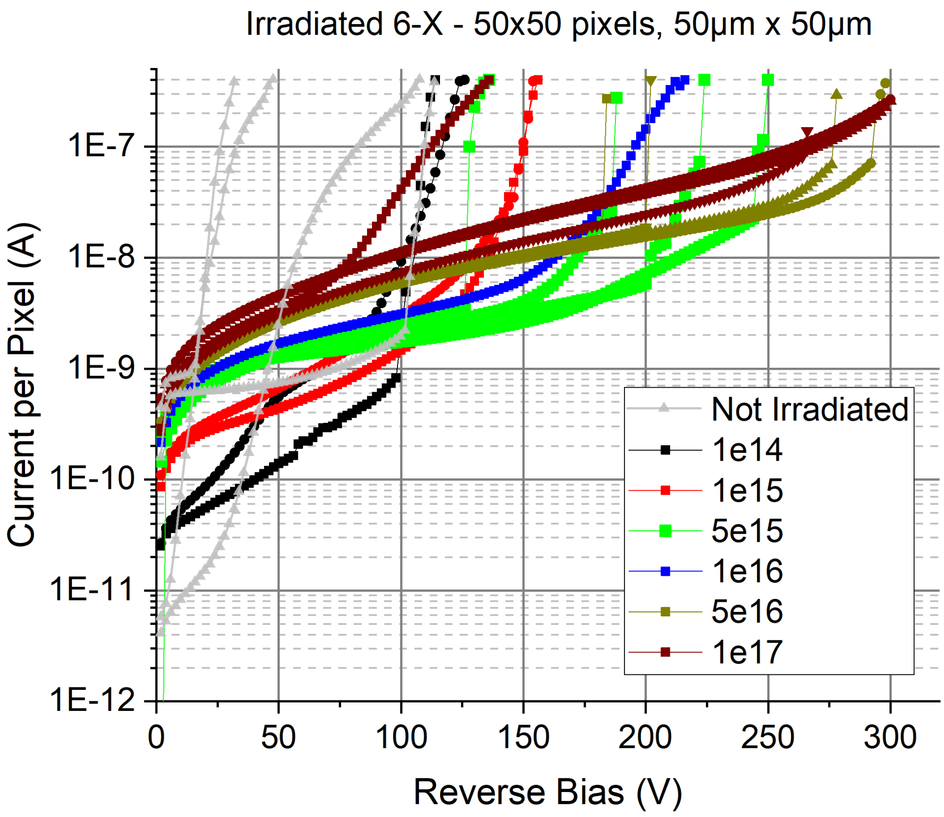

(A)

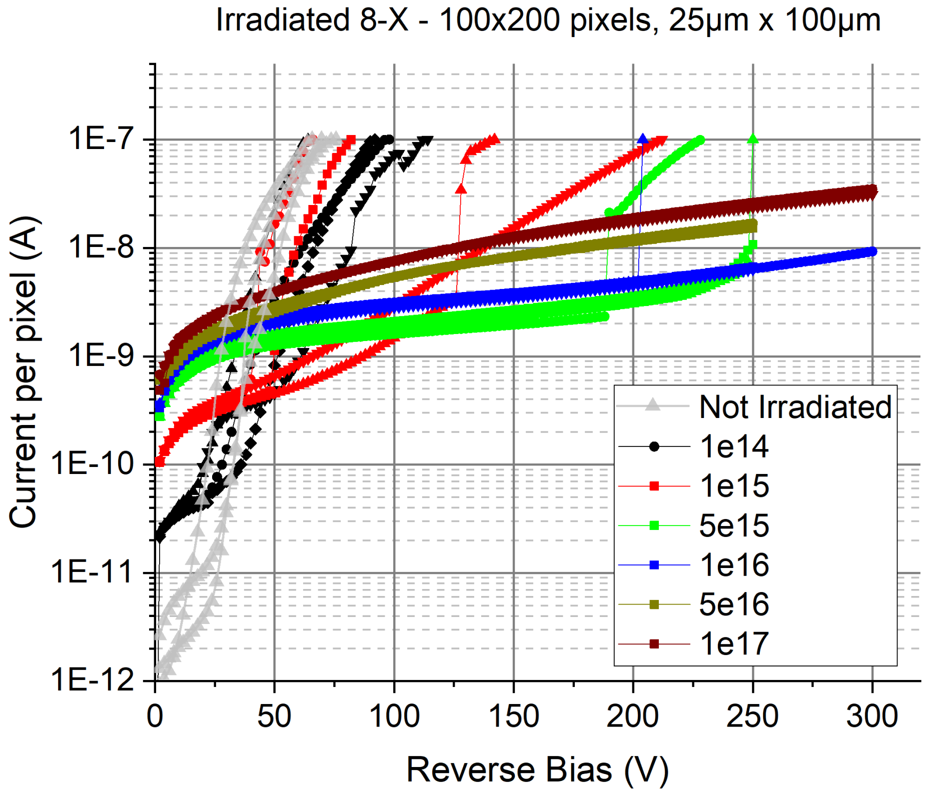

(B)

FIGURE 2.12: I-V curves for the 6-X(A) and 8-X (B) at different fluence levels.

higher than $1 \cdot 10^{15} n_{eq}/cm^2$. However, at $1 \cdot 10^{14} n_{eq}/cm^2$ the leakage current is not lower. On the other hand, 6-X and 8-X sensors show an increase of leakage current with fluence that saturates at levels above $1 \cdot 10^{15} n_{eq}/cm^2$, a phenomena discussed in section 1.5.2.

To better understand the depletion volume in irradiated sensors, C-V curves have been performed. Fig. 2.13 shows the inverse square of the capacitance per pixel ($1/C^2$) versus bias for 6-X sensors with a pixel pitch of $50\mu m$ x $50\mu m$ (left) and 8-X sensors with a pixel pitch of $25\mu m$ x $100\mu m$. The higher the equivalent fluence level, the slower the $1/C^2$ increases, indicating slower depletion. For example, at the fluence level of $1 \cdot 10^{14} n_{eq}/cm^2$, both devices reach saturation with just a few volts, while at $1 \cdot 10^{16} n_{eq}/cm^2$ full depletion is reached before $50V$. At $1 \cdot 10^{17} n_{eq}/cm^2$ for 6-X devices it reaches a maximum after which it decreases due to a much larger leakage current. As studied and explained in [53], a high leakage current can alter the capacitance of the sensor by effectively introducing a resistor in parallel making it difficult to determine the full depletion voltage at high fluence levels. At the fluence levels of $5 \cdot 10^{16} n_{eq}/cm^2$ and $1 \cdot 10^{17} n_{eq}/cm^2$ for 8-X devices it is only observed a constant increase without reaching a plateau. Further bias could not be applied due to reaching the compliance current, since 8-X devices are larger arrays of electrodes.

The full depletion voltage can be calculated by extracting the crossing point of the two straight-lines fits to the rapid initial increase and the plateau in the $1/C^2$ vs V curves. For the fluence levels of $5 \cdot 10^{16} n_{eq}/cm^2$ and $1 \cdot 10^{17} n_{eq}/cm^2$ for the 6-X, $1/C^2$ decreases before reaching a plateau, so the maximum value is taken. The same fluences for the $25\mu m$ x $100\mu m$ pixel pitch geometry do not show any maximum point and are not considered. Fig. 2.14 shows the full depletion voltage versus fluence level for both pixel pitches. In both geometries, the full depletion voltage increases with fluence. The $25x100$ μm pixel pitch geometry requires a slightly larger bias to fully deplete, due to the larger distance between n-type electrodes.

For the 1-X and 2-X devices, C-V curves could not be performed because the capacitance per pixel is of the order of $1 \cdot 10^{-13} F$, which is lower than the noise level of the system. Large devices need to be used to obtain a measurable capacitance.

Some of the small test structures with a single central channel were also irradiated at the same fluence levels. As discussed in Section 2.1, some of them required a re-metallization process to be measurable, specifically those irradiated at $5 \cdot 10^{16} n_{eq}/cm^2$ and $1 \cdot 10^{17} n_{eq}/cm^2$. The resulting I-V curves

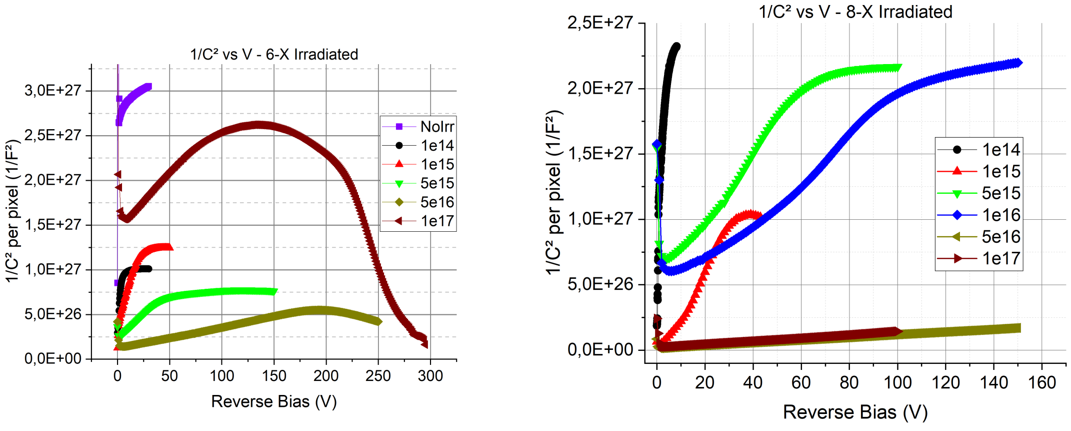

(A) (B)

FIGURE 2.13: $1/C^2$ versus V curves for irradiated pad diodes 6-X (A) and 8-X (B). The curve before irradiation was not included for the 8-X devices. The C-V for the 6-X devices were done at a frequency of 1kHz due to other frequencies not yielding reliable enough results.

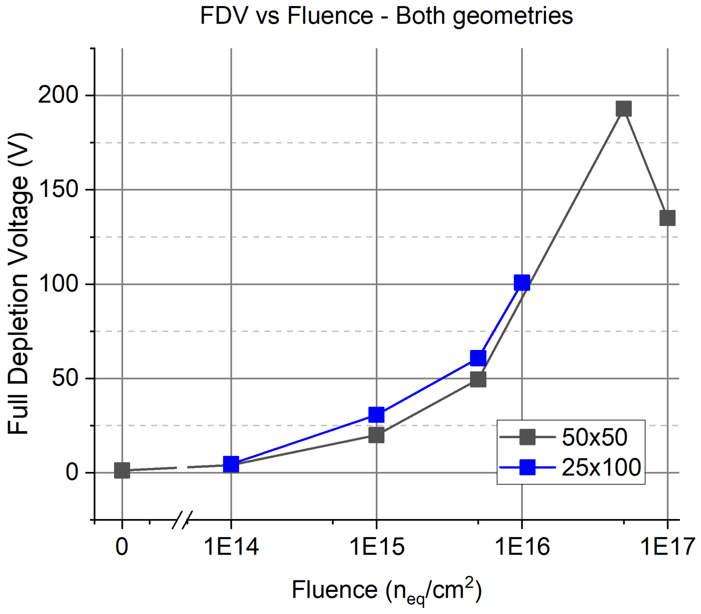

FIGURE 2.14: Full Depletion voltage for the 50x50 μm (black) and 25x100 μm (blue) geometries.

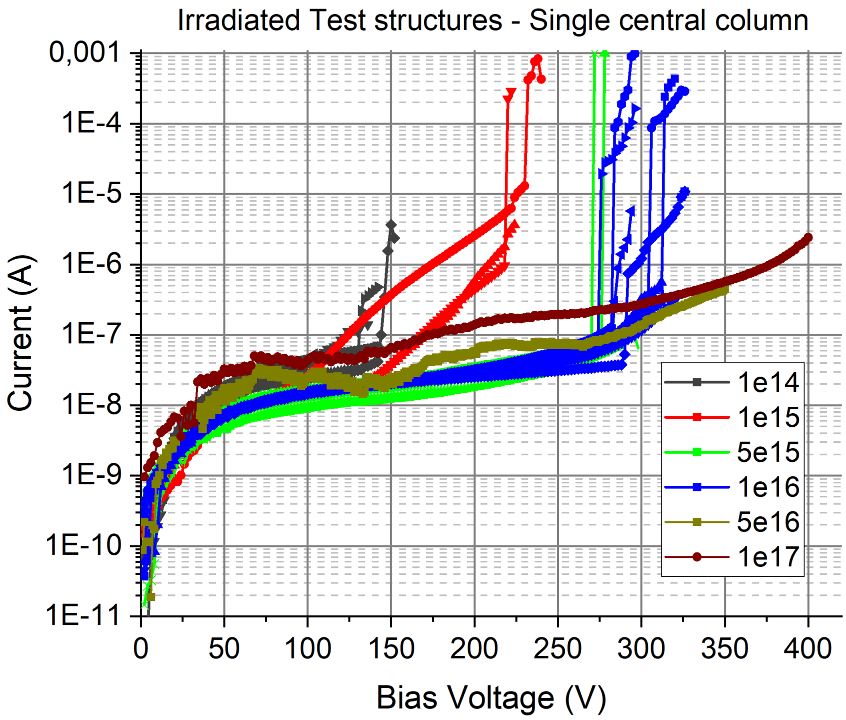

FIGURE 2.15: I-V curves of small test structures irradiated at different fluence levels.

are presented in Fig. 2.15. Similar to the case for 1-X and 2-X sensors, the leakage current does not significantly change with fluence, making it difficult to differentiate the dependence of the leakage current on fluence level. Sensors irradiated at $5 \cdot 10^{16} n_{eq}/cm^2$ and $1 \cdot 10^{17} n_{eq}/cm^2$ show a noisy behavior, attributed to the re-metallization process not yielding high-quality metal and leaving some non-uniform extra metal on the surface that could not be removed and may produce changes in the leakage current.

For a better comparison of the leakage current at different irradiation levels, Fig. 2.16 shows the mean value of the leakage current for all samples irradiated at the same fluence level, plotted against the fluence level. The values of the leakage current are taken at a bias of 100V to ensure full depletion for all sensors below $1 \cdot 10^{16} n_{eq}/cm^2$ (see Fig. 2.14). The error bars represent the spread of the measurements. The leakage currents for $5 \cdot 10^{16} n_{eq}/cm^2$ and $1 \cdot 10^{17} n_{eq}/cm^2$ are based on single measurements.

From $1 \cdot 10^{14} n_{eq}/cm^2$ to $1 \cdot 10^{15} n_{eq}/cm^2$, the leakage current decreases, increasing again at higher irradiation levels. This phenomenon, also observed for the 1-X and 2-X sensors, can be attributed to the substrate undergoing type inversion at a fluence around $1 \cdot 10^{14} n_{eq}/cm^2$.

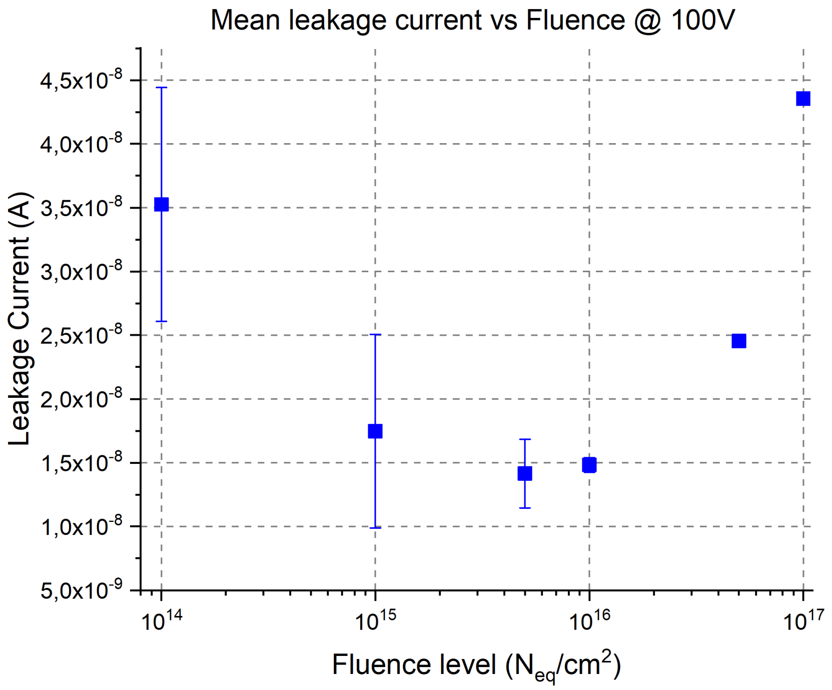

FIGURE 2.16: Leakage current of the test structures at a bias of 100V for the different fluence levels.

Chapter 3

Transient Current Technique (TCT) measurements

One way to characterize a radiation sensor is by measuring its response to a laser projected onto it while it is partially or fully depleted. By doing so, as explained in section 1.4.1, the photons will create free carriers that can be collected at the electrodes, resulting in a measurable signal as described by Ramo's theorem. A suitable experimental setup for this purpose is the Transient Current Technique (TCT). In this study, the top-TCT method was used, where the laser illuminates the top of the sensor. This method is particularly useful for 3D sensors, as it allows for the study of the non-uniformity of the electric field from the top view. The alternative method, edge-TCT, involves illuminating the sensor from the side and is most useful for studying the depletion volumes of planar sensors. However, this configuration is not considered in this work.

3.1 Setup

The TCT setup used for this work is the Particulars [54] top-TCT setup with some additional components for the time resolution measurements, shown in Fig. 3.1. The setup features an IR laser of 1064nm which is connected to an optical system that focuses the light on a supporting plate which holds the PCB that contains the sensor. According to Fig. 1.9, in the range of the 1064nm, the intensity of the beam will decrease a factor $1/e$ with some dozens of centimeters, which are orders of magnitude above the thicknesses of the silicon sensors under study. Therefore, lasers with a wavelength within the IR range allows the photons to go through the sensor with effectively not losing energy, hence allowing the study the behavior of the sensor throughout the whole sensor's thickness. The laser is sent by pulses with a duration ranging from 350ps to 4000ps with energy depositions up to the equivalent

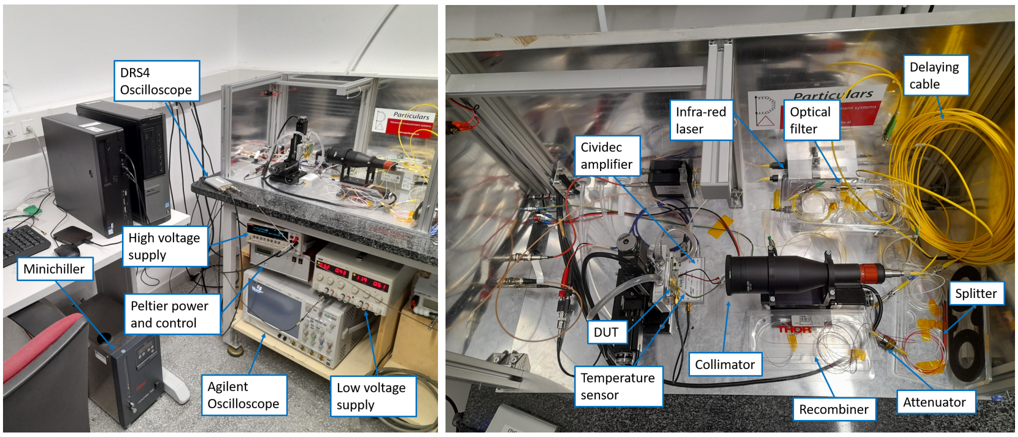
DRS4
Oscilloscope
High voltage
supply
Minichiller
Peltier power
and control
Agilent
Oscilloscope
Low voltage
supply
Infra-red
laser
Optical
filter
Delaying
cable
Cividec
amplifier
Splitter
DUT
Temperature
sensor
Collimator
Recombiner
Attenuator

(A) (B)

FIGURE 3.1: Photos of the TCT setup, of (A) the equipment for biasing, cooling down and the oscilloscope, and (B) the optics to create two signals, as well as the amplifier and the DUT.

of 1000 times a MIP particle [55], [56]. The frequency at which the pulses are sent can be changed in a range from 500Hz to 500kHz. Moreover, the laser features an output which sends a signal when a laser pulse is created which can be used as a trigger in the oscilloscope.

The PCB containing the DUT and used for the read-out was designed in DESY [57], and is shown in Fig. 3.2. It features a ground for both the backplane and the surounding strips, and a second connection used for both the bias and the read-out. In order to apply the bias and to collect the output of the sensor, a bias-T is needed. It has been used by means of the integrated bias-T that has the Cividec amplifier used for the measurements. It features a gain of 40dB and a bandwidth of 2GHz. In order to bias the DUT, a Keithley 2410 has been used as a power supply, while the TTi EX354Tv low voltage supply has been used to bias to the Cividec amplifier.

The PCB is mounted on a plane with motorized stages which move in the X and Y directions. A third motorized stage moves the focusing lens in the perpendicular direction of the plane of the sensor, used for focusing the laser beam on the DUT, with a procedure that will be explained in section 3.2. The stages can be controlled by the software designed by the company Particulars. Therefore, waveforms at specific positions can be taken by using the stages and the digitizer controlled by software and by using the trigger sent by the laser. The digitizer of choice is the PSI DRS4, featuring up to 5GSPS (Giga-Samples per second) with 1024 sampling points, and a bandwidth of 700MHz [58].

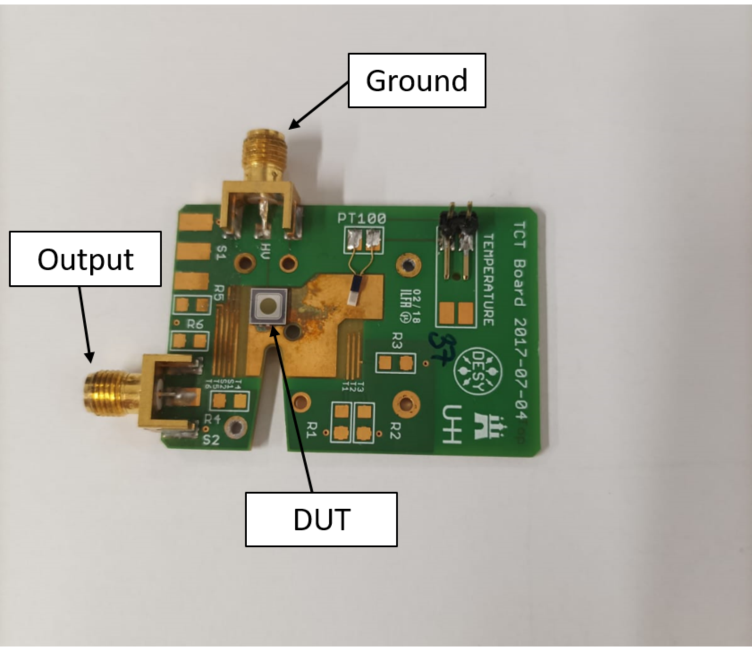

FIGURE 3.2: Image of the PCB board designed by DESY used for the TCT measurements. The DUT is a 300 μm thick PiN sensor used for signal calibration, explained in section 3.3.

As explained in section 1.7.5, two signals are required for timing measurements. In order to have two signals from a single sensor, the laser beam is split by means of an optical splitter. One of the resulting beams is delayed by passing through a 5m optical fiber cable, causing a delay of approximately 50ns, which ensures that both signals do not overlap while are still within the same frame of the oscilloscope. Both signals are then recombined by using a splitter in reverse, namely a combiner, producing in a single output that conform the two laser pulses. Due to an imperfect combining process, after the process there may be a signal higher than the other. Therefore, a tunable attenuator is introduced to equalize both signals in the oscilloscope, so that equation 1.31 holds. Additionally, since the first splitter does not have a coefficient of transmition of 1, some of the pulse would be reflected and go back to the laser generator, which could cause damage. To prevent this, a filter is introduced, which blocks any light from returning to the laser. A schematic representation to the different optical parts for the time resolution is represented in Fig. 3.3.

While for focus scan measurements and charge collection maps the PSI DRS4 is enough, for timing measurements it is crucial that the waveforms are correctly resolved in time. 3D sensors have rise-time of the order of the picoseconds [59]. So, in order to properly resolve the signals a bandwidth of the order of the GHz would be necessary. For that, the Agilent infiniium

SDA90804A oscilloscope has been used, featuring a bandwidth of 8GHz and 40GSPS.

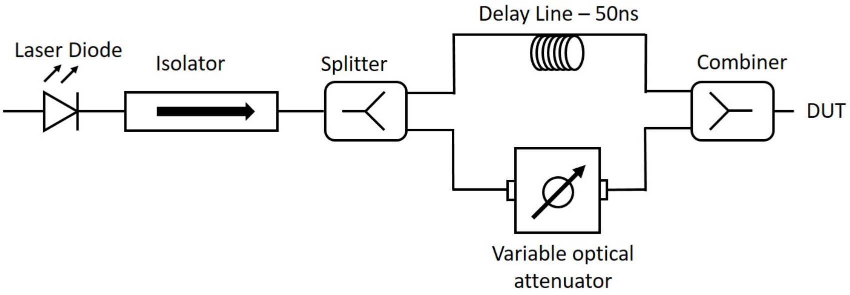

FIGURE 3.3: Schematic representation of the circuit with which the beam from the laser is separated in two different paths to induce two signals to the sensor.

3.2 Focus Scan

The first step to get high quality measurements in a TCT setup is to get a good focus of the laser beam in order to have the smallest beam spot size possible on the top of the sensor. To achieve so, the optical axis has to be moved so that the focus point from the optical system is found within the sensor. This is performed by means of a focus scan, where waveforms are taken at different points along one of the axis on the plane of the sensor, the scanning axis, at different positions in the optical axis. The scanning direction has to cross a region in which there is metalization, so that no charge is collected, towards another with active region where charge is collected, or viceversa. By doing so, there will be a transition from having no signal to having the signal in the sensor, which will depend on the size of the beam on the sensor. A smaller beam size will lead to a sharper transition, while a larger one will smoothen it. The FWHM of the beam size can then be extracted by means of the fit of the error function to the plot of the charge along the scanning axis at the region of the transition.

An example of a focus scan performed on a 3D test structure irradiated at a fluence level of $1 \cdot 10^{16} n_{eq}/cm^2$ is shown in Fig. 3.4. The regions A, B and C correspond to regions where alternate having a metal on top, hence having no charge collection, with having no metal and therefore having charge collected. The size of each region is, respectively, 40 μm, 25 μm and 35 μm. In Fig. 3.4-A the curves in black, red and green, being the first three curves, do not show any significant difference in charge collection along the scanning

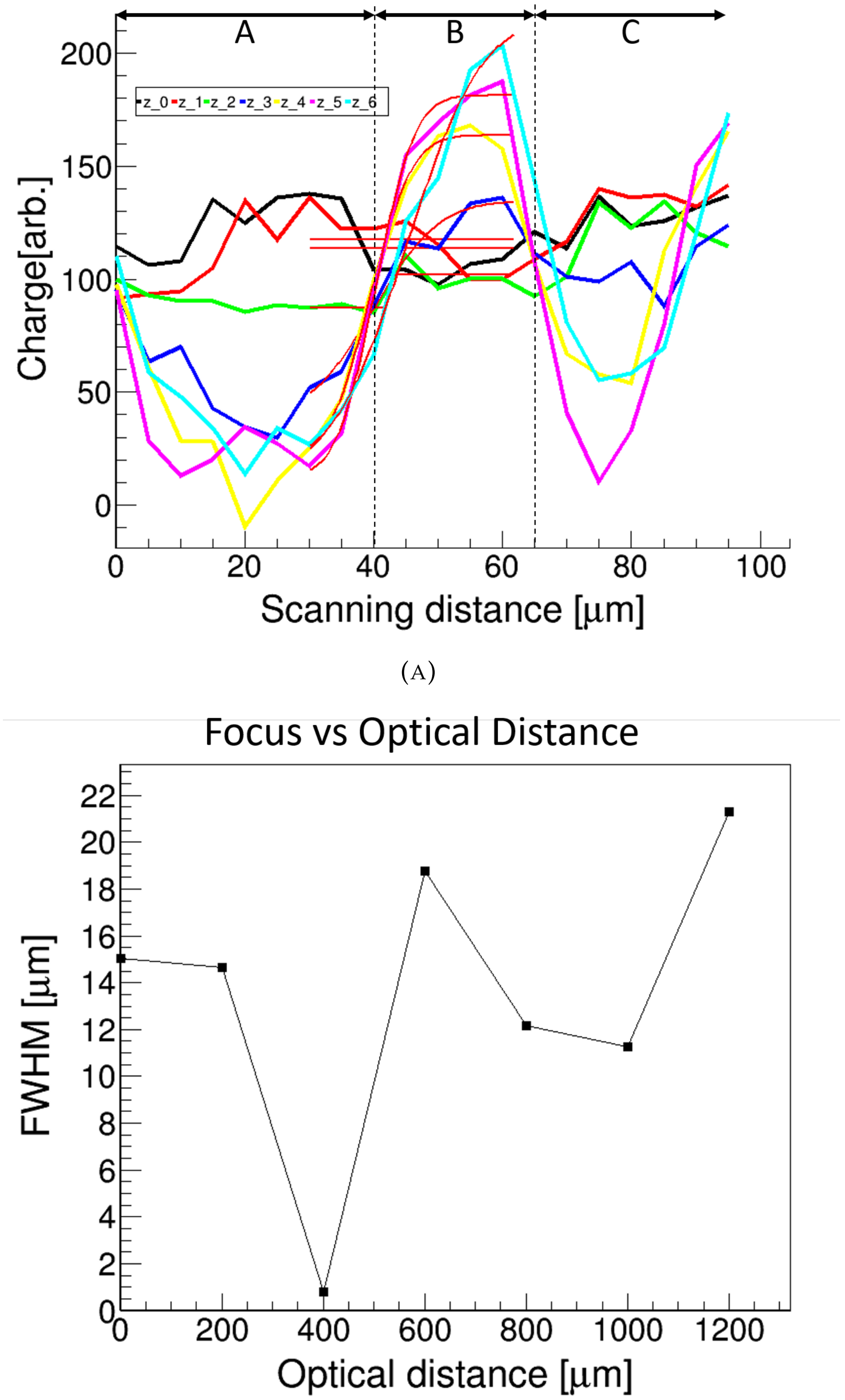

(A)

(B)

FIGURE 3.4: A: Charge collected along the scanning axis, corresponding to the direction represented in Fig. 3.5. B: The FWHM extracted from the fits for each of the taken curves in A.

distance. For that reason, no fit could be done on them and the script fails at fitting an error function, resulting in a flat curve. However, the curves in blue, yellow, pink and teal show the expected behavior, and the fits could be performed. In Fig. 3.4-B, the resulting FWHM from the error function fits are presented. The first three points are to be ignored due to corresponding to the flat curves to the first three curves. The remaining points correspond to the curves 4 to 6, and range from FWHM of 12 μm to approximately 22 μm.

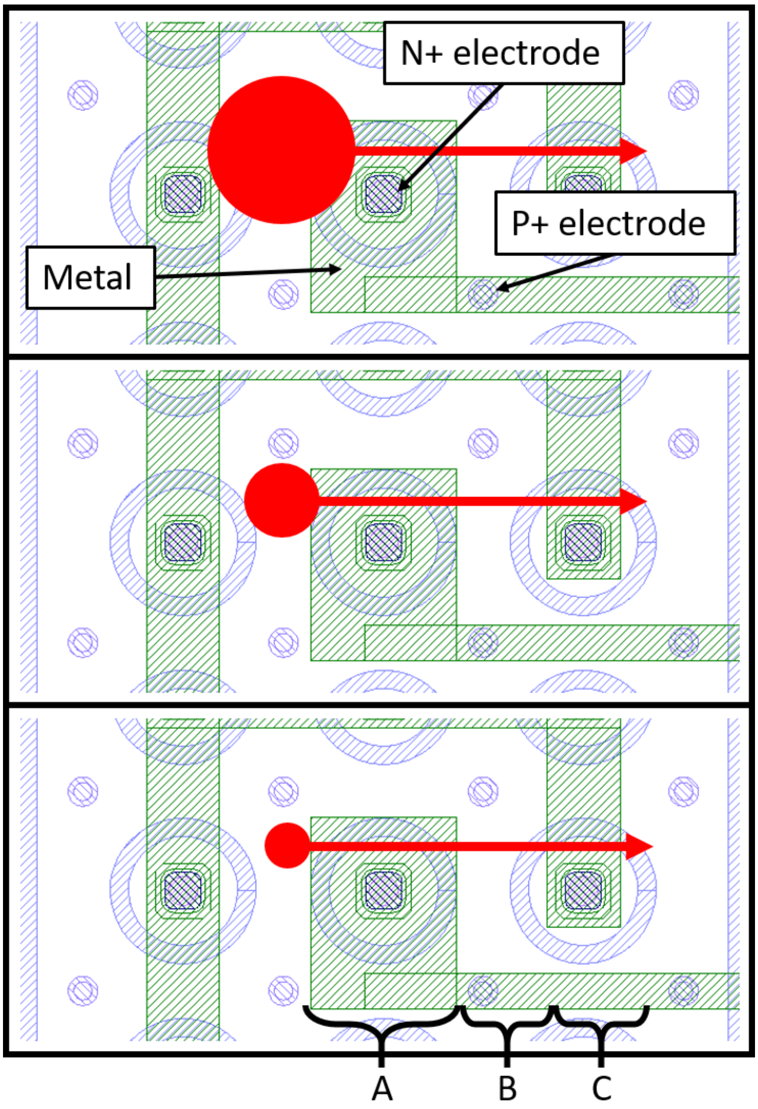

FIGURE 3.5: Graphical representation of different spot sizes with relation to the test structures and the travelled distance along the focus scan from Fig. 3.4. The diameters of the spot sizes correspond, in the scale of the mask layout and from top to bottom, to 40 μm, 20 μm and 12 μm.

In order to compare these sizes with the test structures, a representation in scale of different spot sizes on the mask layout of the sensors are shown in Fig. 3.5, with spot sizes corresponding to 40 μm, 20 μm and 12 μm. The three regions correspond to the same three regions differentiated in Fig. 3.4. Region B, which features the largest charge collection due to not having any metalization, has a width of 25 μm. Therefore, spot sizes of more than 25 μm would lead to having large reflection of the laser in the regions between pixels, leading to a smoothed curve instead of the sharp transition that would feature a small spot size.

3.3 Signal calibration with beta source

One of the studies conducted in this work is the time resolution of the n-on-n sensors. As discussed in section 1.7.1, one of the main contributions to the time resolution of a sensor is the jitter, which depends on the signal height of the sensor. Since the laser does not provide information about the number of emitted photons, and the aperture of the optical system cannot be quantified, it is important to have a reference for the laser intensity projected on the device under test (DUT) to avoid arbitrary biases toward higher or lower signal heights that may skew the results. For this purpose, a planar PiN sensor with a thickness of 300μm has been chosen as the reference.

Using the exact same equipment as in the TCT to read out the signal, a Sr90 radioactive source was used in order to create MIP-like signals. The waveforms were taken with the Agilent infiniium SDA90804A and analyzed with a python script. The histogram distribution of the signal height when operated at 300V at room temperature is shown in Fig. 3.6, with the Gausian fit in green. The number of bins in the histogram is given by using the Shimazaki Shinomoto algorithm [60]. It calculates the optimal number of bins by creating different possible histograms with a variety of binwidths and minimizes the Cost Function:

$$C(h) = \frac{2\bar{n} - \sigma^2}{h^2} \tag{3.1}$$

Where $\bar{n}$ is the mean number of samples per bin, σ^2 is the variance of the number of samples per bin, and h is the bin width. This method has been used for all the histograms within this thesis.

A Gausian fit on the histogram distribution shows a Most Probable Value (MPV) of 63mV. Therefore, prior to any performed measurements, the PiN reference sensor was mounted and the laser was set so that it creates a signal in the sensor as close as possible to 63mV. In the case that a higher signal has been used, it will be stated as a multiple amount of 63mV and will be referred as certain amount of times the signal of a MIP.

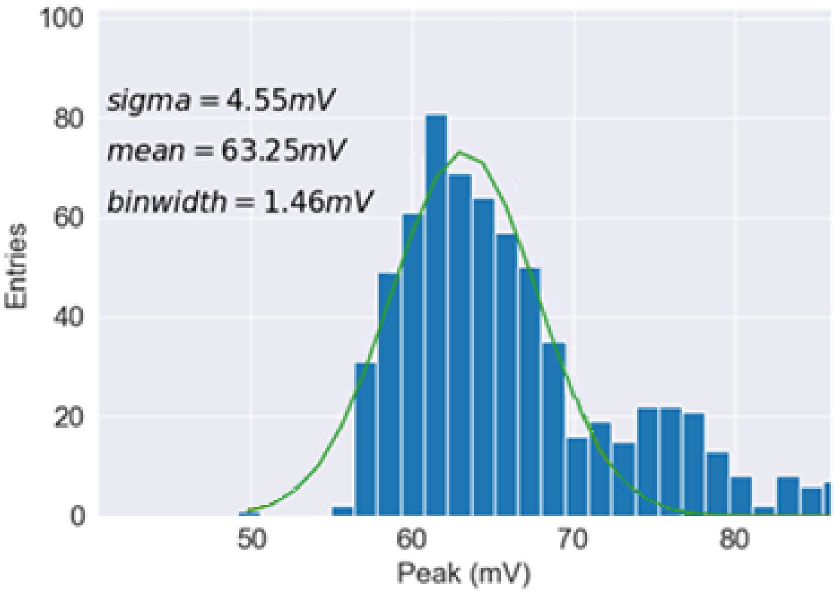

FIGURE 3.6: Histogram distribution of the signal height taken for the planar PiN reference sensor. The mean value of 63mV has been used as the charge generation resulting from the laser intensity and the iris opening of the optical focusing system.

3.4 Pad diode arrays

The first sensor that has been studied in the TCT setup are the pad diode arrays of 50x50 pixels with a pixel pitch of $50\mu m\ x\ 50\mu m$, labeled as 6-X, already introduced in section 2.1. An image of the mask is shown in Fig. 3.7. These pad diode have all pixels shortened by means of a layer of highly doped polysilicon in order to minimize the metalized area, since it would reflect all the photons coming from the laser. It is important to note that the highly doped polysilicon layer may induce some reflection due to the difference in refractive index. However, in [61], optical studies were carried out for highly doped polysilicon layers. A comparison of the measured refractive index is shown in 3.8, where at the range of $1060nm$ in wavelength, show approximately a refractive index of 3.35 for the doped polysilicon, while for crystalline silicon would be of 3.5450. The reflectance in the case of normal incidence, which is a good approximation for the top-TCT setup, can be calculated by means of Fresnel's equation:

$$R_0 = \left| \frac{n_1 - n_2}{n_1 + n_2}^2 \right| \tag{3.2}$$

Where R_0 is the reflectance in the case of normal incidence, and n_1 and n_2 are the refractive indexes of the two materials. This results in a reflectance of

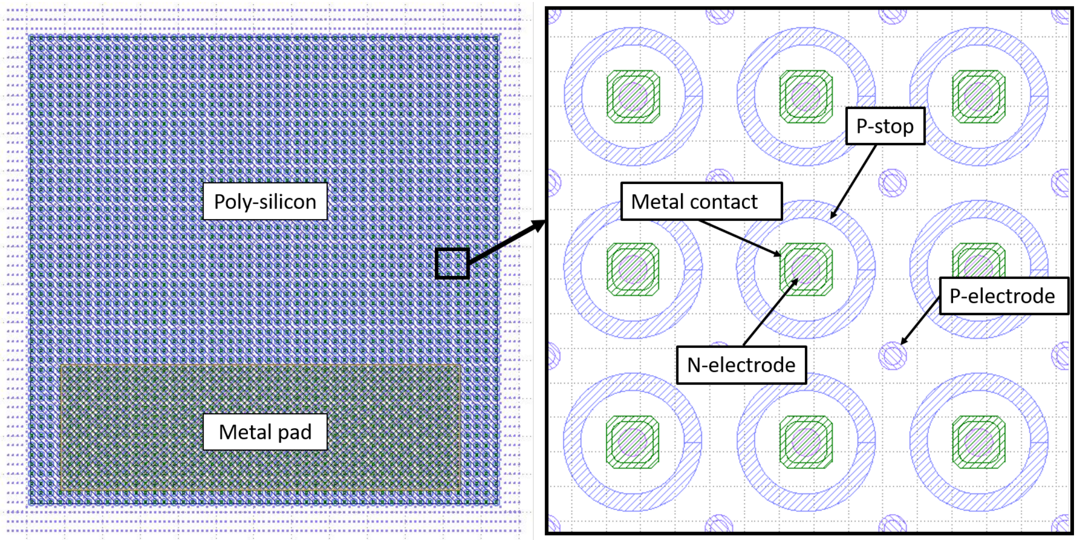

FIGURE 3.7: Representation of the mask for the 6X devices. A zoomed in region has been presented so that can be compared with the 2D charge collection map.

approximately 0.02%, which effectively is quite negligible.

The only featured metal in the pad diodes are placed as the contact for the n+ electrodes with the highly-doped polysilicon, as well as a metal pad at the bottom of the sensor used as a contact for I-V measurements at the probe station. Moreover, it is used as the wire-bonding place, which was connected to a single-channel PCBs from DESY, shown in Fig. 3.2.

3.4.1 2D charge collected map

One crucial aspect of studying 3D sensors for timing applications is the charge collection efficiency (CCE) of the sensor and how charge is collected at different positions within a cell lattice. One way to achieve this is by taking waveforms in a 2D scan and integrating the charge at various positions. Since the pad diode has no temporary metal and is fully covered with polysilicon, there should only be reflection at the metal contacts of the n-type electrodes. However, due to the noise observed during the focus scan, as discussed in section 3.2, the spot size may vary between $10\mu m$ and $20\mu m$. Such sizes mean that the beam spot might be too large relative to the spatial resolution required for certain information. For instance, a spot size of $20\mu m$ compared to a pixel pitch of $50\mu m$ represents a significant percentage of a pixel cell, resulting in a loss of resolution in the spatial information.

2D maps of the charge collection of a small region of the 6-X sensors

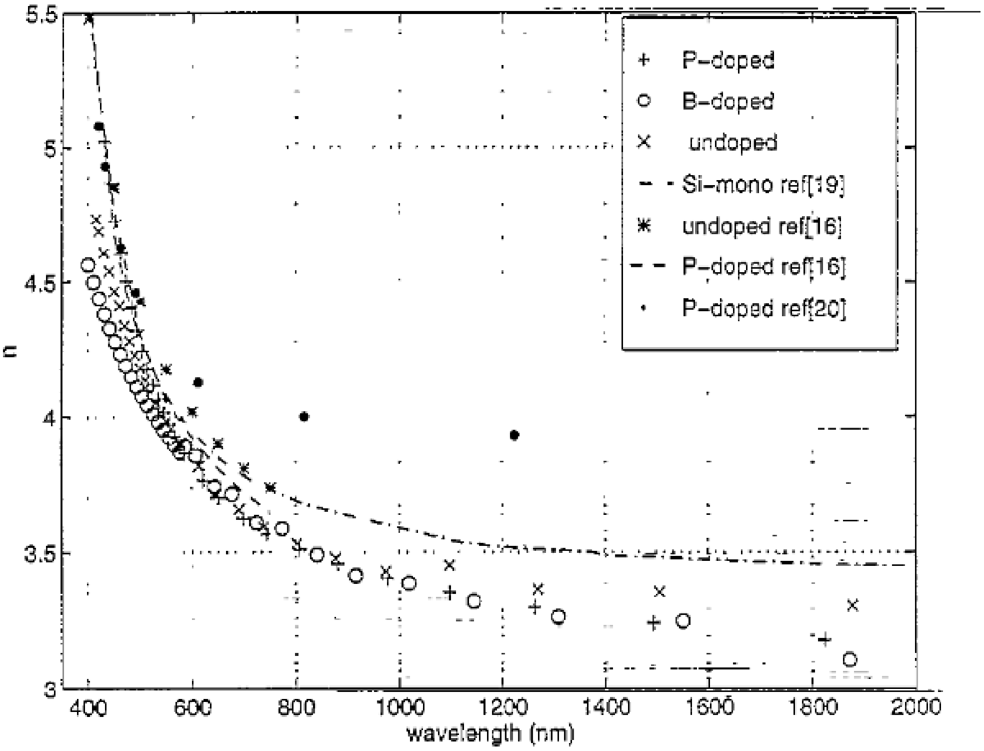

Fig. 9. Refractive index of undoped, P-, and B-doped polysilicon with thicknesses of 562 nm, 574 nm and 601 nm, respectively.

FIGURE 3.8: Plot of the refractive index for different doping concentrations in polysilicon . Graphic extracted from [61].

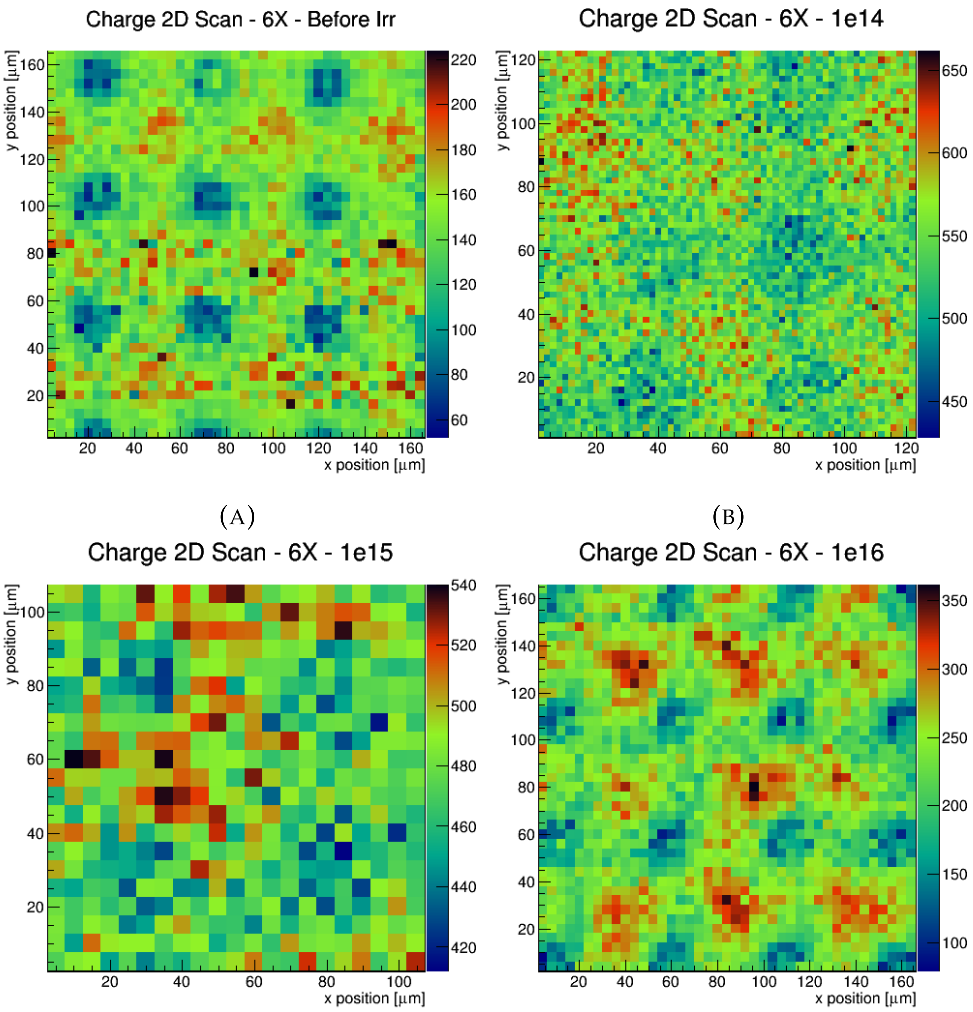

(A) (B)

(C) (D)

FIGURE 3.9: 2D maps of the charge collected for different fluence levels at different devices. Must be taken into account that some of them have different step size and total scanning distance for both directions.

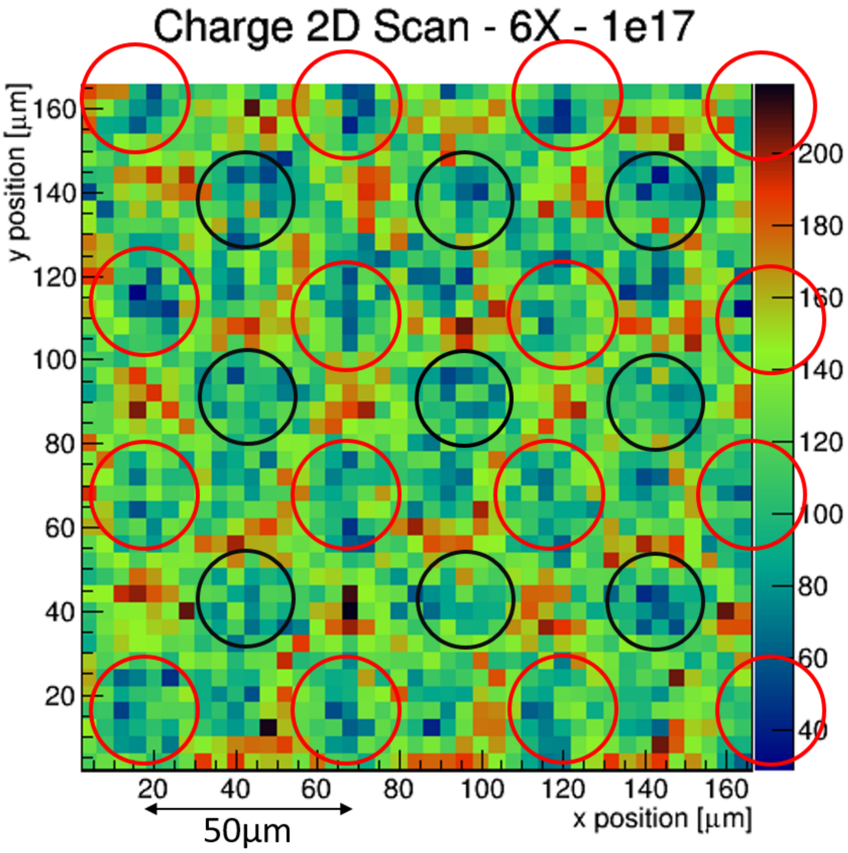

FIGURE 3.10: 2D map of the charge collected for the device irradiated at the fluence level of $1 \cdot 10^{17}$ n_{eq}/cm^2. Red and black circles highlight the intercalation of the n-type electrodes, with the positions equidistant to the n-electrodes coinciding with regions with low charge collection.

for fluences up to $1 \cdot 10^{16} n_{eq}/cm^2$ are represented in Fig. 3.9. The best-defined patterns are observed before irradiation and at a fluence level of $1 \cdot 10^{16} n_{eq}/cm^2$. For fluences of $1 \cdot 10^{14} n_{eq}/cm^2$ and $1 \cdot 10^{15} n_{eq}/cm^2$ the profiles are more diffused, primarily due to poorer focus which reduces the reflection of the laser spot from the metalization on top of the n-electrodes. Regardless of the sharpness of the transitions in the metalized region, the pattern between low and high charge collection has a pitch of $50 \mu m$, corresponding to the pixel pitch of the sensor. This indicates that the highest charge collection in a TCT setup occurs at positions equidistant to the n+ electrodes, which are near the p+ electrodes, due to the lower amount of light reflected by the metallization.

In Fig. 3.10-A, the 2D map of a 6-X sensor irradiated to an equivalent fluence level of $1 \cdot 10^{17} n_{eq}/cm^2$ is presented. The charge collection pattern shows two distinct 50 μm pitch patterns, shifted by 35 μm diagonally. These patterns are highlighted with red and black circles. This shift suggests that while the metal still reflects some light, reducing charge collection in those areas, regions furthest from the n+ electrodes also show reduced charge collection. This implies that the mean free path of the generated carriers in these regions is less than the 35 μm distance they must travel to reach the electrode.

3.4.2 Time resolution

Time resolution measurements have been conducted using the splitting system described in section 3.1, with the waveform analysis performed as outlined in section 1.7.5 over 2000 samples per measurement. These measurements were taken at locations with the highest charge collection by adjusting the stages to avoid laser reflection. Consequently, all time resolution measurements for the 6-X sensors were conducted in regions approximately on top of a p+ electrode, which is the furthest possible position from the n+ electrode. Given that such a large array of pixels generates high noise due to the resulting capacitance connected in parallel, this becomes a more dominant factor, especially with the inherently fast response of 3D sensors.

The sigma of the fit for the difference in Time of Arrival (ToA) of the two peaks, which determines the time resolution, for different fluences and bias voltages with a prior 1 MIP-like signal calibration is shown in Fig. 3.11. From the figure, it can be concluded that the best time resolution is achieved post-irradiation, likely due to the higher noise from the leakage current before substrate inversion. Additionally, higher operational voltage results in a stronger electric field, leading to faster signals and potential charge multiplication.

No measurements were possible at the fluence level of $1 \cdot 10^{17} n_{eq}/cm^2$ due to an insufficient SNR. This was attributed to the high noise from the combined effects of leakage current and capacitance, as well as significantly reduced charge collection efficiency due to radiation damage. To achieve timing measurements, a better SNR is necessary, which could only be obtained by increasing the laser intensity. Therefore, another time resolution measurement was performed with the PiN signal calibrated to double the intensity of the 1 MIP calibration, achieving an amplitude of 126mV compared to 63mV for 1 MIP calibration. The time resolution using a 2 MIP signal is shown in Fig. 3.12. Comparing the time resolutions with 1 MIP and 2 MIP signal calibrations, the 2 MIP calibration consistently yields a better time resolution, reducing from 255ps to 197ps before irradiation and more significantly from

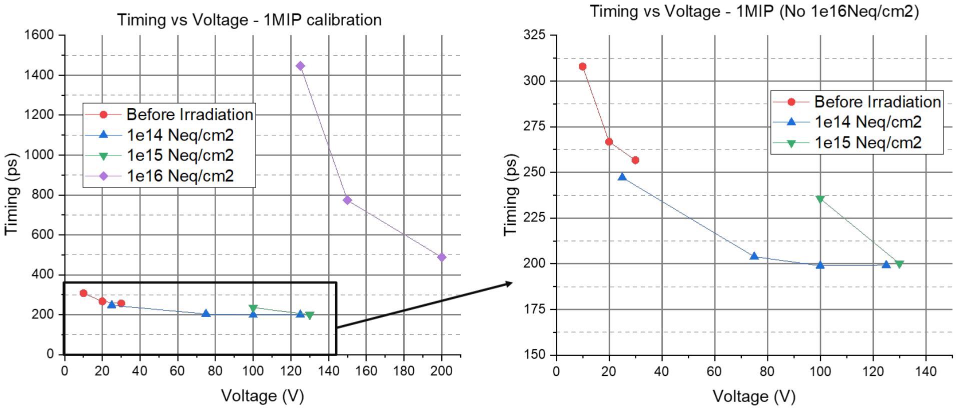

(A)

FIGURE 3.11: Time resolution for 6-X sensors irradiated at different fluence levels at different bias voltages for a 1 MIP-like signal calibration. Since the sensor irradiated at $1E16n_{eq}/cm^2$ has a much higher value for the time resolution a separate plot for the other fluences has been done so that the difference in time resolution with voltage can be better seen.

412ps to 248.6ps at the fluence level of $1 \cdot 10^{16} n_{eq}/cm^2$. With higher laser intensity, a time resolution of 688ps was achieved at the $1 \cdot 10^{17} n_{eq}/cm^2$ fluence level at $225V$.

Fig. 3.13 shows a study of the time resolution for different multiple a MIP calibration, where time resolution was measured for various fluence levels with controlled amounts of laser intensities. The plot indicates that as laser intensity increases, the time resolution improves but eventually reaches a plateau, with other factors such as field distortion and rise time becoming more dominant contributors to the time resolution, as further explained in section 1.7.

Given the significant impact of electric field distortion on time resolution in 3D sensors, a preliminary 2D map of the time resolution of a pixel cell was created by performing time resolution measurements at various positions of the 6-X sensor irradiated at $1 \cdot 10^{17} n_{eq}/cm^2$ with a 3-MIP calibration. In Fig. 3.14-A the timing distribution is presented, with time resolution measured in steps of $10\mu m$. When compared with the amplitude map (Fig. 3.14-B), a clear dependence of time resolution on amplitude is observed, where higher signals yield better time resolutions. Thus, the limiting factor for time resolution in these devices at high fluence levels is the SNR, due to the high capacitance of the large array combined with reduced signal from charge trapping at extreme radiation doses.

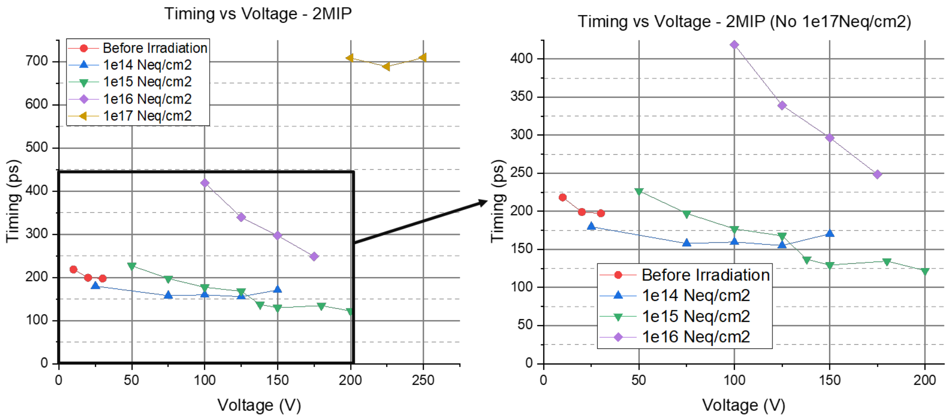

(A)

FIGURE 3.12: Time resolution for 6-X sensors irradiated at different fluence levels at different bias voltages for a 2 MIP-like signal calibration. Since the sensor irradiated at $1 \cdot 10^{17} n_{eq}/cm^2$ has a much higher value for the time resolution, a separate plot for the other fluencies is provided to better illustrate the variation in time resolution with bias voltage.

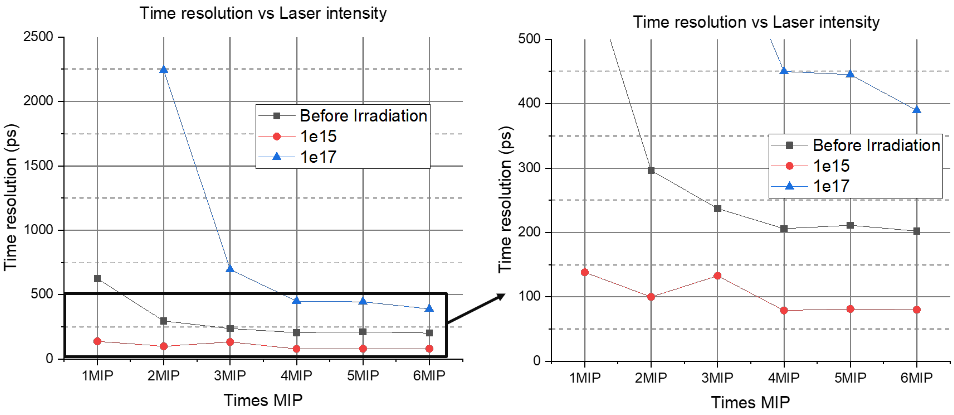

(A)

FIGURE 3.13: Time resolution versus bias for 6-X sensors irradiated at different fluence levels, with the laser intensity set at different multiple times 1-MIP.

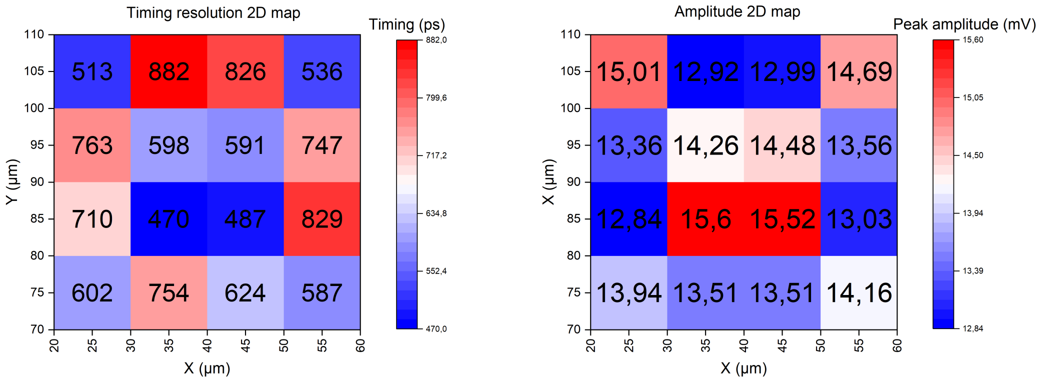

(A) (B)

FIGURE 3.14: 2D map of the time resolution (A) and peak amplitude (B) taken for a 6-X sensor irradiated at an equivalent fluence level of $1E17n_{eq}/cm^2$ and biased at 250V. The laser intensity calibration was of 3-MIP.

3.5 Small test structures

As seen in section 3.4.2, achieving good time resolution, especially with 3D detectors, requires a high signal-to-noise ratio (SNR), as it is the most limiting factor. One way to decrease the noise is by using smaller arrays of pixels, which reduces the capacitance contribution and thus improves the SNR. In this section, test structures featured in the run 10339 and introduced in chapter 2 with the mask diagram in Fig. 2.10, are characterized using a TCT setup with the same methodology as described in the previous section. In these samples, the central column and the neighbouring pixels are connected in two different pads (mask diagram in Fig. 2.10). Since the PCB has a single readout, see section 3.1 for more details, it is necessary to connect it to both pads simultaneously. For that reason, a wire-bonding process was employed, in which the soldering was placed between both pads, ensuring that a sufficiently large solder joint was used to make contact with both pads concurrently.

As discussed in section 3.2, performing a focus scan requires a metallized region to ensure a rapid transition from signal to no signal. In this case, unlike the 6-X sensors, there is no metal pad on top of the sensor. The region used was the metalization on top of the n+ electrode from the central pixel which has a size of $40\mu m x 50\mu m$. A sample focus scan with this type of sensor was shown in Fig. 3.4, where a focus scan on a test structure irradiated with a fluence level of $1 \cdot 10^{16} n_{eq}/cm^2$ yielded a spot size with a FWHM of approximately $12 - 13\ \mu m$.

3.5.1 2D charge collection map

Using the same procedure as the 6-X sensors, 2D charge collection maps have been performed for the test structures at different equivalent fluence levels, and different bias voltages, shown in Figs. 3.15 and 3.16. In them, the metalized regions can clearly be identified as the regions with a lower charge collection, while both the external and internal active area have a higher charge collection, with also the mask design matching the patterns observed.

Before irradiation, the charge collection is considerably uniform across the active area of the central pixel and the surrounding pixels. However, the higher noise prevented achieving a sufficiently sharp focus, resulting in less distinct transitions on the metallized regions compared to other scans.

For the fluence level of $1 \cdot 10^{14} n_{eq}/cm^2$, the metal transitions are more defined, and charge is collected in regions beyond the surrounding pixels. This can be attributed to the much higher operational voltages, which create a stronger electric field, while the radiation damage is not yet sufficient to cause significant charge trapping. At $1 \cdot 10^{15} n_{eq}/cm^2$, there is a very high signal close to the metal pad region, which should not be considered relevant for ionizing particle measurements. However, the signal generated in the regions between the central pixel and its neighboring ones is consistently higher compared to lower fluences. This increase may be due to a multiplication effect caused by the higher reverse bias voltage.

For the fluences of $5 \cdot 10^{15} n_{eq}/cm^2$ and $1 \cdot 10^{16} n_{eq}/cm^2$ the profiles appear quite similar. The former exhibits less defined regions and lower charge collection, likely due to the use of a reverse bias of $150V$. Despite reaching full depletion, this voltage is insufficient to trigger an avalanche effect as seen at $1 \cdot 10^{15} n_{eq}/cm^2$. In contrast, at $1 \cdot 10^{16} n_{eq}/cm^2$, a reverse bias of $220V$ provides more optimal performance.

At $5 \cdot 10^{16} n_{eq}/cm^2$, a high reverse bias of $300V$ induces a multiplication mechanism similar to that observed at $1 \cdot 10^{15} n_{eq}/cm^2$, resulting in significantly higher charge collection. However, due to increased trapping of drifting carriers, little charge is collected in regions beyond the neighboring pixels, as their travel distance is greater.

Lastly, at a fluence of $1 \cdot 10^{17} n_{eq}/cm^2$, charge collection decreases significantly. Similar to the previous fluence level, collection is primarily limited to regions near the pixels, indicating a higher probability of carrier trapping and thus shorter mean free paths for free drifting carriers

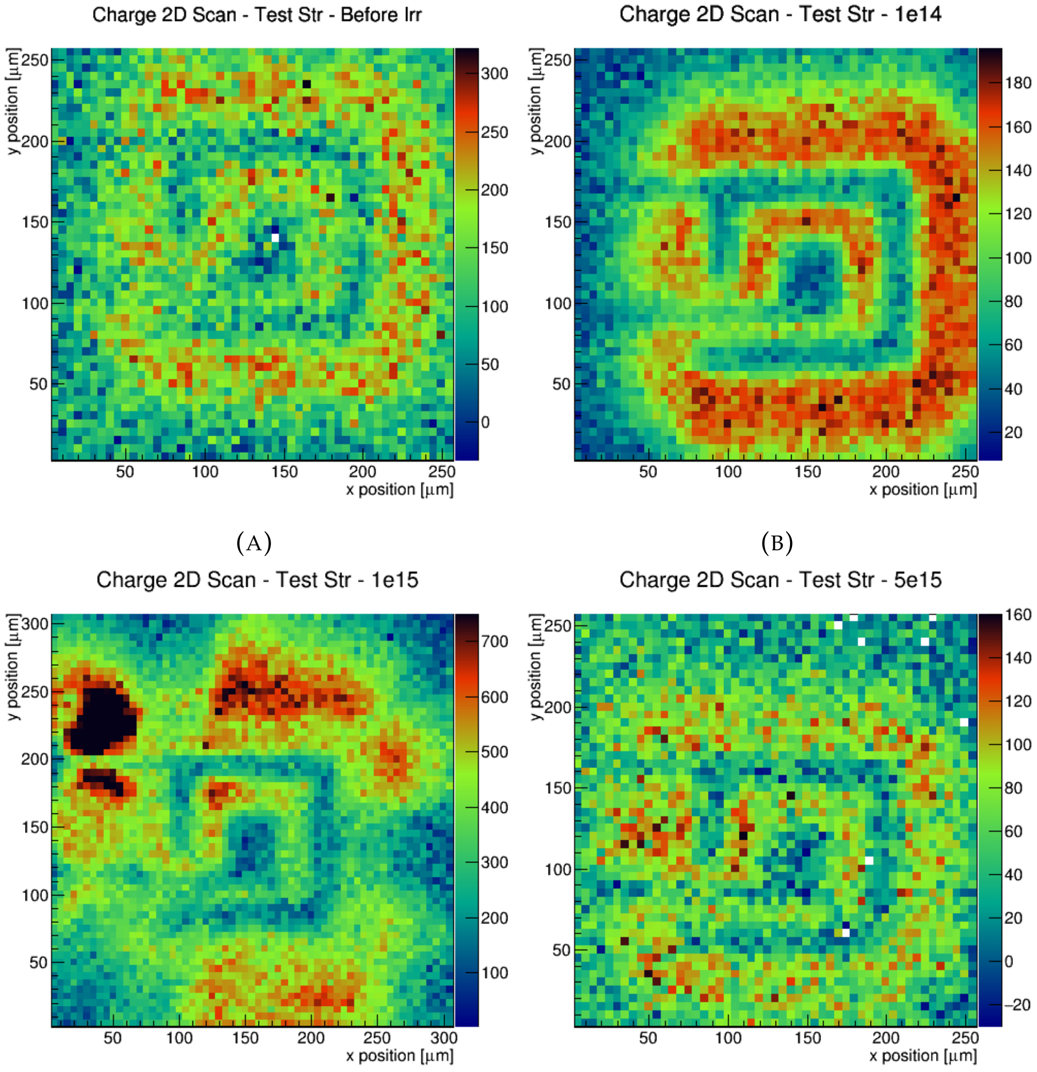

(A) (B) (C) (D)

FIGURE 3.15: 2D maps of the charge collected for different fluence levels for the test structures. The operational voltages from no fluence to higher fluence levels were 30V (Before Irr), 30V ($1 \cdot 10^{14} n_{eq}/cm^2$), 150V($1 \cdot 10^{15} n_{eq}/cm^2$) and 150V ($5 \cdot 10^{15} n_{eq}/cm^2$).

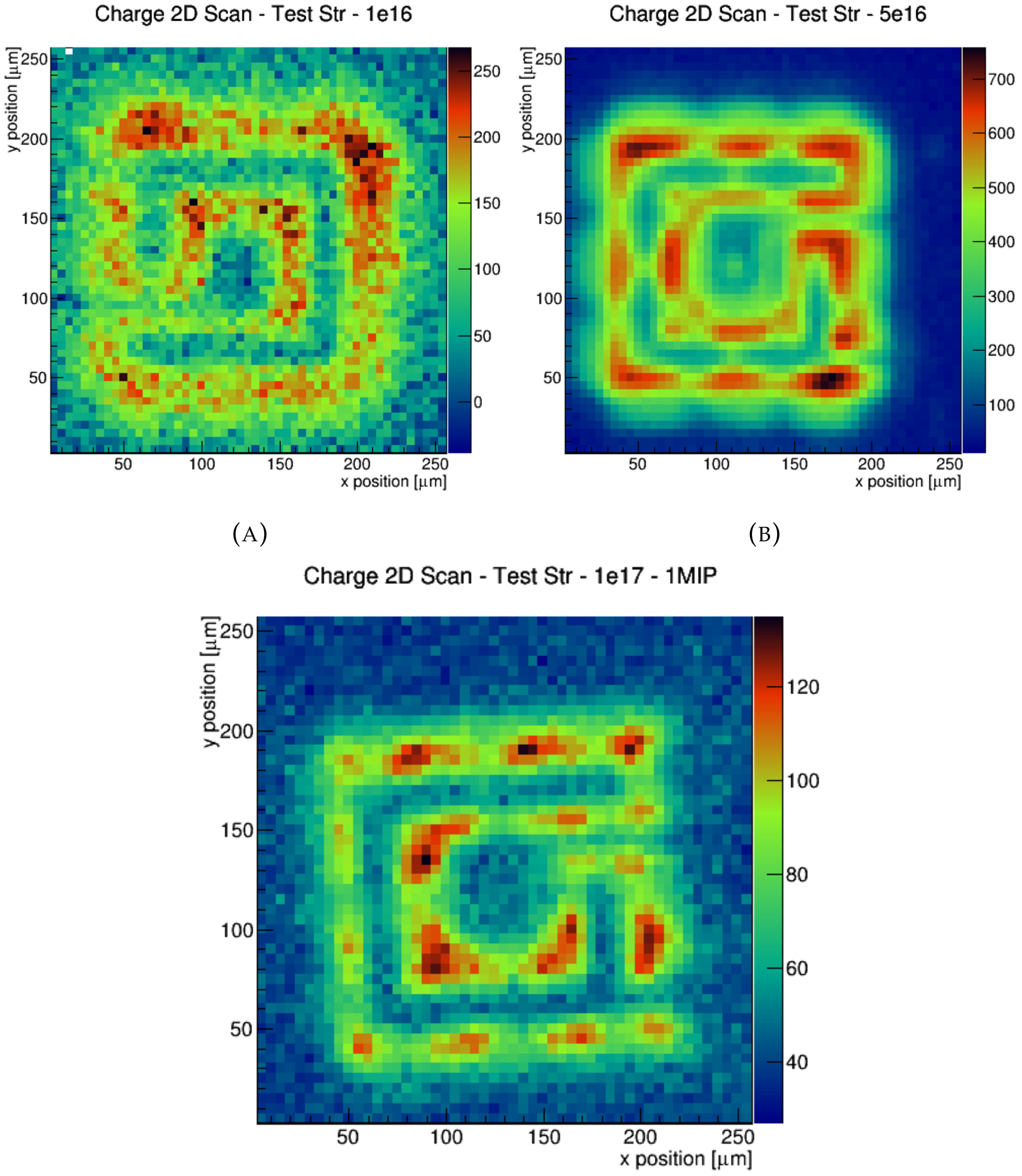

(A)

(B)

(C)

FIGURE 3.16: 2D maps of the charge collected for different fluence levels for the test structures. The operational voltages from lower to the highest fluence level 220V ($1 \cdot 10^{16} n_{eq}/cm^2$), 300V ($5 \cdot 10^{16} n_{eq}/cm^2$) and 350V ($1 \cdot 10^{17} n_{eq}/cm^2$)

3.5.2 Time resolution

After obtaining the charge collection maps, the stages were moved so that the focus of the laser was placed between the central pixel and the one directly above it, based on their positions in the 2D charge collection maps. Subsequently, 3000 waveforms were recorded and analyzed by means of the method discussed at section 1.7.5. The results of time resolution measurements at a 1-MIP calibration are presented in Fig. 3.17-A. The error bars are given by the square root of the covariance matrix of the parameters resulting from the Gausian fit in the histogram distributions. A comparison with time resolutions of 6-X devices shows noticeable improvement, particularly for the sensor irradiated at a fluence equivalent to $1 \cdot 10^{16} n_{eq}/cm^2$, where the resolution improved from 412ps to 52ps. The resolutions are even around 30 ps for fluences ranging from $1 \cdot 10^{14} n_{eq}/cm^2$ to $5 \cdot 10^{15} n_{eq}/cm^2$, with the non-irradiated sensor performing worse due to higher leakage current attributed to the n-on-n configuration before substrate inversion.

At the fluence level of $1 \cdot 10^{15} n_{eq}/cm^2$ there is a minimum time resolution value after which it begins to increase. This increase is due to a soft-breakdown process where the leakage current rises significantly but still allows for time resolution measurements. The avalanche effect is evident when examining the representation of peak amplitudes vs. voltage in Fig. 3.17-B, where a significant increase in amplitude at 150V indicates a charge multiplication mechanism, as well as an increase of the noise RMS shown at Fig. 3.18-A for this fluence level.

At the equivalent fluence level of $5 \cdot 10^{15} n_{eq}/cm^2$, the capacity of biasing towards a high voltage of $250V$ allows for a time resolution of $32ps$, while for $1 \cdot 10^{16} n_{eq}/cm^2$, it increases up to $53ps$. However, at the equivalent fluence level of $5 \cdot 10^{16} n_{eq}/cm^2$ the time resolution deteriorates to $106ps$. This degradation can be attributed to a longer rise time, as observed in Fig. 3.18-B which is approximately three times longer compared to the other sensors. It was not feasible to obtain the time resolution at the fluence level of $1 \cdot 10^{17} n_{eq}/cm^2$ due to a SNR insufficient for accurate analysis by the script.

3.5.3 Charge Collection Efficiency

In order to get the charge collected at each fluence level, the integral of the charge for each waveform was performed. A histogram of the distribution of the charge was performed, and a Gausian fit was done. The mean value of the fit was considered as the MPV of the charge for each point. The square

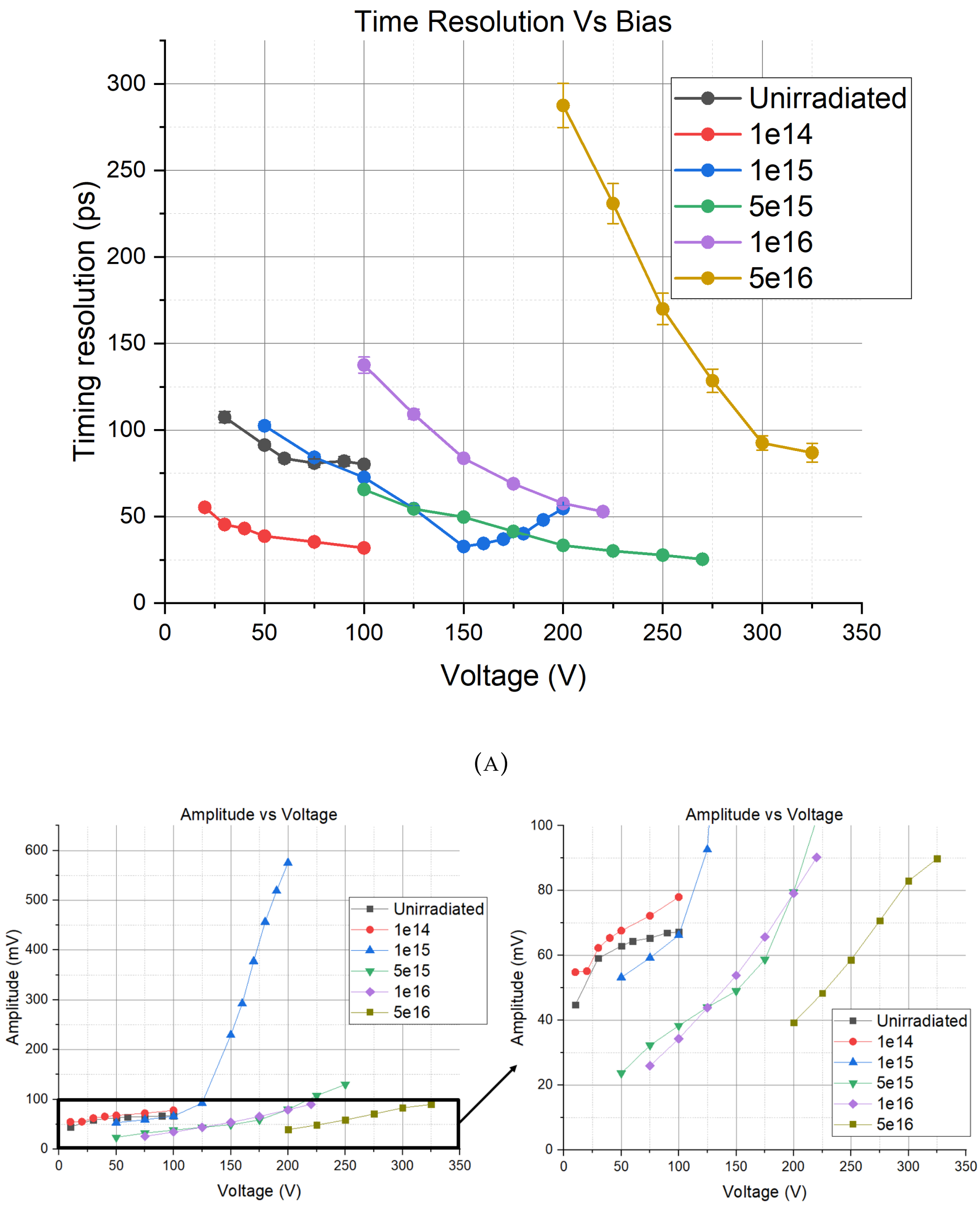

(A)

(B)

FIGURE 3.17: In A, time resolution of the test structures irradiated at different fluence levels at different bias voltages for a 1 MIP-like signal calibration. In B, amplitude of the signal peak for the different fluence levels at different bias voltages.

root of the sigma was taken as the error bar. The charge collection efficiency (CCE) was then calculated by means of the relation CCE = Charge before irradiation/Charge after irradiation. The resulting plot is shown at Fig. 3.19.

Before irradiation and the fluence level of $1 \cdot 10^{14} n_{eq}/cm^2$ have very similar charge collections efficiencies, due to them being at approximately the

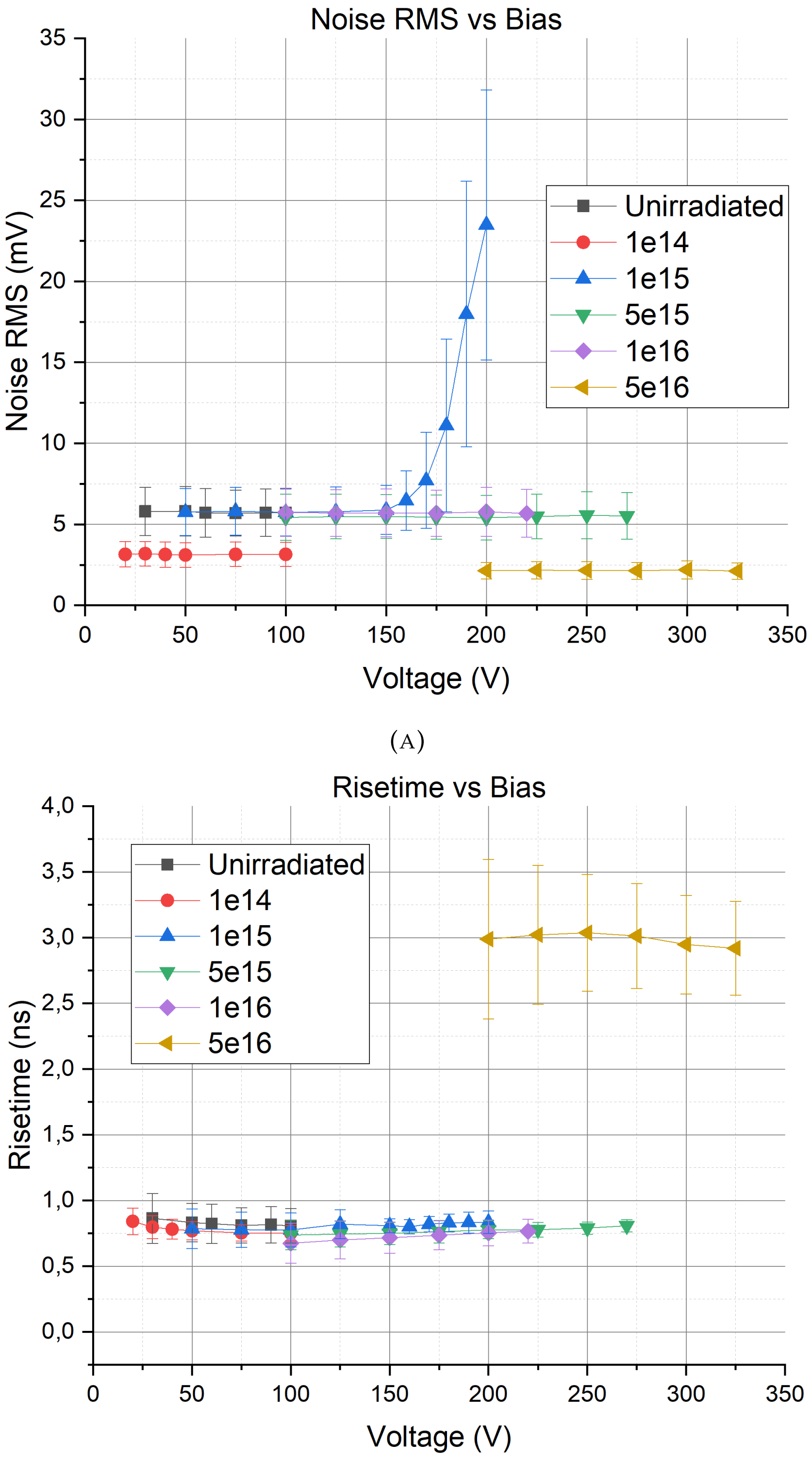

(A)

(B)

FIGURE 3.18: Noise RMS (A) and risetime (B) values versus bias at the different equivalent fluence levels.

same range of biases. However, similarly as with the amplitude plot, Fig. 3.17-B, at equivalent fluences ranging from $1 \cdot 10^{15} n_{eq}/cm^2$ to $5 \cdot 10^{16} n_{eq}/cm^2$, it is possible to achieve higher charge collections due to charge multiplication at higher biases. Conversely, the bias required to reach these values increases with fluence, potentially increasing the power consumption. Fig. 3.20 showcases the bias required to have the same charge collection as a non-irradiated sensor, showing the increase of bias required to reach the same amount of charge collected.

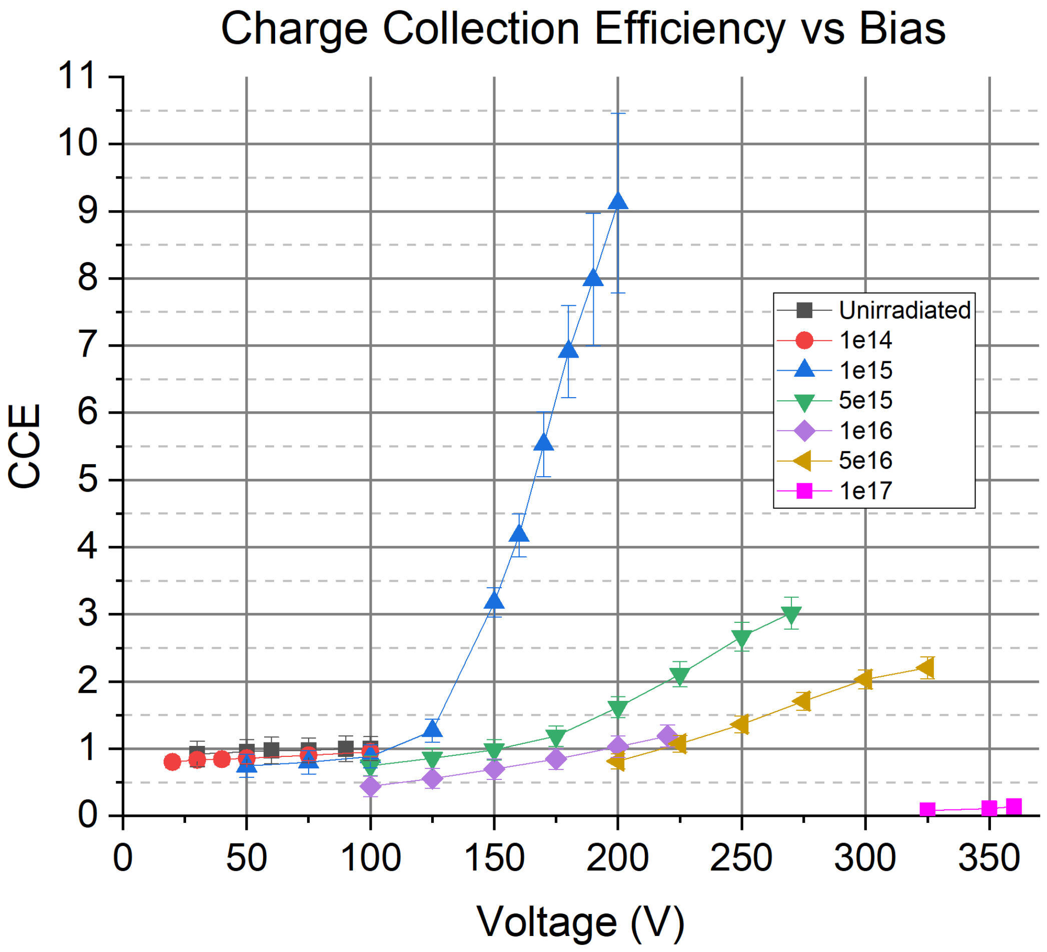

(A)

FIGURE 3.19: Charge collection efficiency versus bias at the different fluence levels.

Similarly to the time resolution analysis, it was not possible to analyze individual waveforms for the sensor irradiated at the equivalent fluence level of $1 \cdot 10^{17} n_{eq}/cm^2$. Despite of this, unlike the time resolution analysis, noise does not affect the charge collection calculations. Therefore, integration was performed on waveforms averaged over the 3000 recorded measurements. Comparing the integrated charge, a charge collection efficiency of 13% was determined, as also shown in Fig. 3.19.

A potential contributing factor to the low charge collection at the fluence level of $1 \cdot 10^{17} n_{eq}/cm^2$ could be that, as discussed in Section 2.1.1, a re-metalization process had to be performed in order to repair the damage contact pads. It was observed that this processes deposited a metal thin film around the area of the contact pads. If this metal film was as well deposited in the area where the measurements were performed, it would absorb light, thereby reducing the number of incident photons on the active area.

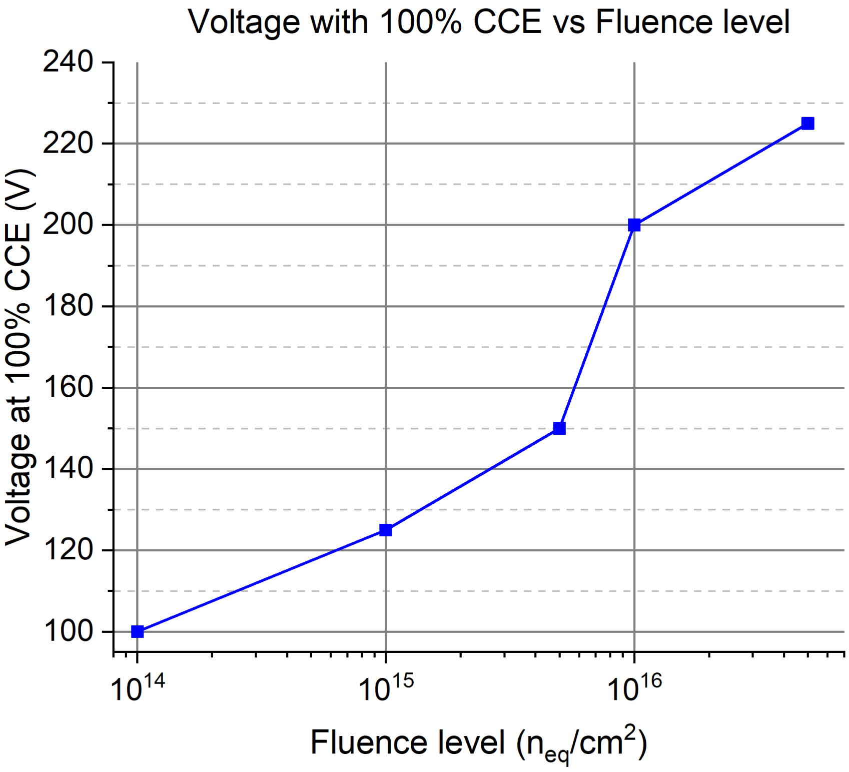

(A)

FIGURE 3.20: Voltage at which a 100% CCE is reached at the different fluence levels.

3.5.4 Conclusions and Future work on TCT measurements

In this chapter, TCT measurements were conducted on arrays of $50x50$ pixels with a pixel pitch of $50\mu m x 50\mu m$, and test structures of $3x3$ pixels with a pixel pitch of $55\mu m x 55\mu m$. The CCE for both configurations have shown to be high when operated at optimal voltages, occasionally exceeding 100%. These results are consistent with previous studies where CCEs of 90% were achieved for $50\mu m x 50\mu m$ pixel pitch 3D sensors [62] and 65% for a fluence of $1.7 \cdot 10^{16} n_{eq}/cm^2$ [63], both measured using radioactive sources.

Thus, TCT proves to be a reliable method for studying 3D sensors, demonstrating agreement with measurements using radioactive sources. It is important to note that variations in light absorption with fluence have been observed, [64] which could potentially lead to an overestimation of charge collection and time resolution at extreme fluences. These observations highlight the necessity for validation through comparisons with measurements using radioactive sources.

Moreover, timing measurements have been carried out with both type of sensors. For the 6-X, the time resolution with a 1-MIP previous calibration have been extracted up to the fluence level of $1 \cdot 10^{16} n_{eq}/cm^2$, showing a time resolution ranging from around 200 ps to around 450 ps, due to the high noise attributed to the capacitance. By increasing the intensity of the laser, the time resolution can be improved significantly, demonstrating how dependent the signal-to-noise ratio (SNR) can be in the case of 3D sensors, where the rise time does not change enough to be a dominant factor. Additionally, timing measurements were conducted on a sensor irradiated at the fluence level of $1 \cdot 10^{17} n_{eq}/cm^2$, yielding a time resolution of around $700 ps$ when using a previous 2-MIP calibration. While this is a high value for time resolution, it should be noted that the large array configuration used for the measurements would not be typical for actual ASIC connections, which would feature much lower noise and hence better time resolution. A study on the signal height showed that the time resolution depends on the laser intensity up to a point of saturation, even at the highest fluence level of $1 \cdot 10^{17} n_{eq}/cm^2$, indicating that at extreme fluences, rise time or electric field distortion becomes more dominant than the jitter contribution.

Time resolution measurements have also been performed on the test structures, all with 1-MIP calibration, up to the fluence level of $5 \cdot 10^{16} n_{eq}/cm^2$. These measurements showed a time resolution of $80 ps$ before irradiation, which improved to $30 ps$ up to the fluence level of $5 \cdot 10^{15} n_{eq}/cm^2$, after which it increased to $50 ps$ and $100 ps$ at the fluence levels of $1 \cdot 10^{16} n_{eq}/cm^2$ and $5 \cdot 10^{16} n_{eq}/cm^2$ respectively. Previous results reported in [65] are within the same range of time resolutions, being of the order of $50 ps$ before irradiation and $80 ps$ at the fluence level of $1 \cdot 10^{16} n_{eq}/cm^2$. Additionally, in [66], time resolutions of the order of $30 ps$ have been reported, showing improvement after irradiation due to higher electric fields and potential multiplication mechanisms.

Lastly, a charge collection efficiency study has been performed on the test structures. It was found that the charge multiplication at high bias for irradiated sensors yield charge collection efficiencies of more than 100% for fluence levels ranging from $1 \cdot 10^{15} n_{eq}/cm^2$ to $5 \cdot 10^{16} n_{eq}/cm^2$. Before irradiation and at fluence level of $1 \cdot 10^{14} n_{eq}/cm^2$ show lower charge collection due to lower bias levels which yield lower electric field. For the fluence level of $1 \cdot 10^{17} n_{eq}/cm^2$ the study had to be carried for a waveform averaged over 3000 samples taken at the measurements. In it, a CCE of 13% was observed, although could be attributed the potential presence of a thin metal film deposited during a the process of repairing the metal pads for the contact.

As future work, to further investigate the dependence of time resolution on the position within the sensor, a 2D map of the time resolution should be generated by setting up an automated system to take waveforms at controlled multiple positions, similar to the 2D charge collection maps. This approach would provide more detailed information about the contribution of electric field distortion, which is not adequately accounted for when the sensor is in a fixed position. Additionally, it has been observed that noise from external sources at the CNM facilities may underestimate the time resolution measurements, which should be investigated and removed. Furthermore, improving the control over the laser intensity would be advantageous, as the beam intensity changes with the laser temperature, and potential changes cannot be monitored after calibration.

Chapter 4

Beta-source setup

In the previous chapter, the performance of n-on-n 3D silicon sensors was tested using an infrared laser to create electron-hole pairs in the bulk, generating signals in the electrodes. While this method is convenient for studying the spatial performance related to the electric field or the charge collection range, and for understanding the order of magnitude of time resolution and charge collection efficiency (CCE), the calibration of the laser intensity is not ideal and may lead to biased results. Additionally, it neglects the Landau fluctuations of a minimum ionizing particle (MIP). Although the effects of these fluctuations are mitigated by the architecture of 3D sensors, they should not be completely ignored. In this chapter, measurements using a beta source setup will be introduced. The commissioning and calibration of the new setup at the CNM Radiation Detector Laboratory will be presented, followed by a discussion of the DUTs and the results obtained from these measurements.

4.1 Setup

To perform time resolution measurements, two signals from the same particle must be recorded within the same timeframe on the oscilloscope. To achieve this, a radioactive source is placed in front of both sensors, supported by metal plates designed to hold the sensors and the source. These plates are mounted on a gridded plane inside a metal box that acts as a Faraday cage, and includes a small aperture for dry air flow to prevent freezing or condensation during cooling down or warming of the system. The metal box is placed inside a freezer that reaches temperatures around $-30^{\cdot}C$ to achieve low temperatures. Strontium-90 (Sr^{90}) is used as the radioactive source due to its emission energy of 0.546, which is close to the energy range of a MIP of 1-2MeV.

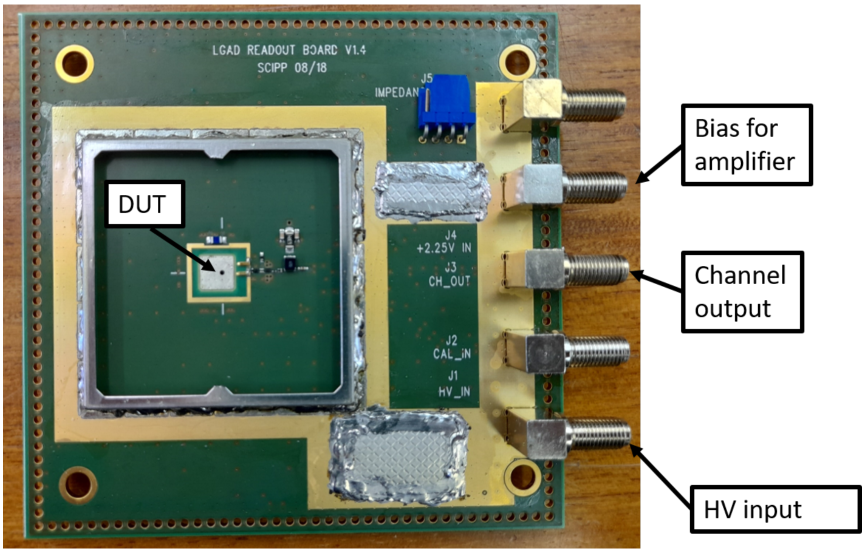

FIGURE 4.1: Picture of a UCSC board used for the Sr90 source setup.

The PCBs used were developed at the University of California Santa Cruz (UCSC). They feature discrete components that provide a wide bandwidth of 2GHz and maintain low noise levels, even in noisy environments [67]. This low noise level is crucial due to, as the time resolution of 3D sensors strongly depends on the signal-to-noise ratio. The board also features an internal first stage amplifier with a gain of 10, supplied with a voltage of 2.25V. A picture of the board, highlighting its principal connections, is shown in Fig. 4.1, with more technical details available in [68]. The board has separate channels for both biasing and readout to the oscilloscope, eliminating the need for a bias-T. The sensors are biased using a Keithley 2410 for the DUT and a Keithley 2470 for the reference sensor. After the first-stage amplifier, each board uses a Cividec amplifier, as introduced in section 3.1, as a second-stage amplifier. All the amplifiers are powered by a TTi EX354Tv low-voltage supply. The signal is read out on an Agilent infiniium DSA90804A oscilloscope, with a bandwith of 8GHz and a sampling rate of 40GSa/s. Images of the setup can be found in Fig. 4.2, and a schematic representation of the system connections is shown in 4.3.

The bias on the DUT at the PCB is applied from the back side, and ground must be set connected to the top of the sensor to properly apply the reverse bias. Additionally, the readout is performed from the same part as the ground, allowing for bias to be applied to different channels while reading out a single one. This possibility is crucial for measurements on the 3D test structures studied in the previous chapter, as it allows for the measurement of individual pixels. Reading out all the pixels simultaneously would result

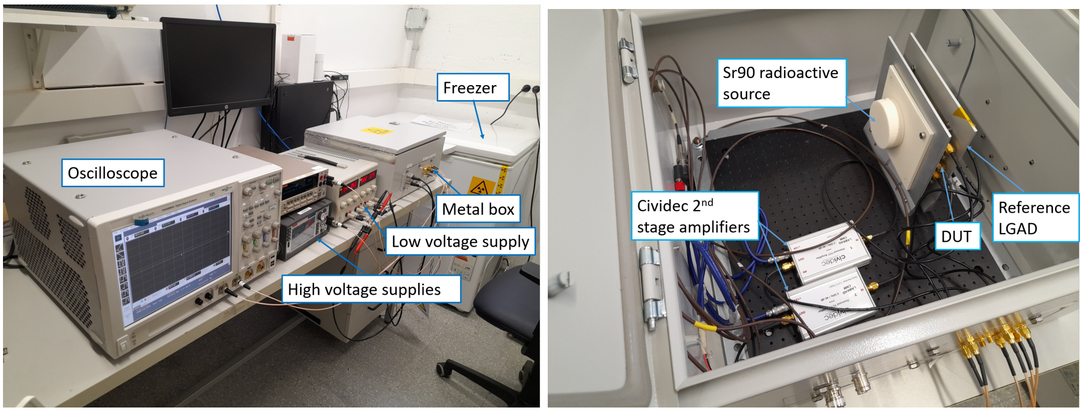
Freezer
Oscilloscope
Metal box
Low voltage supply
High voltage supplies
Sr90 radioactive source
Cividec 2nd stage amplifiers
DUT
Reference LGAD

(A) (B)

FIGURE 4.2: Pictures from the Sr90 source setup. On the left, the used equipment for biasing, the oscilloscope, the metal box and the freezer, and on the right where the sensors are placed, the amplifiers and the sensor used to monitor the temperature.

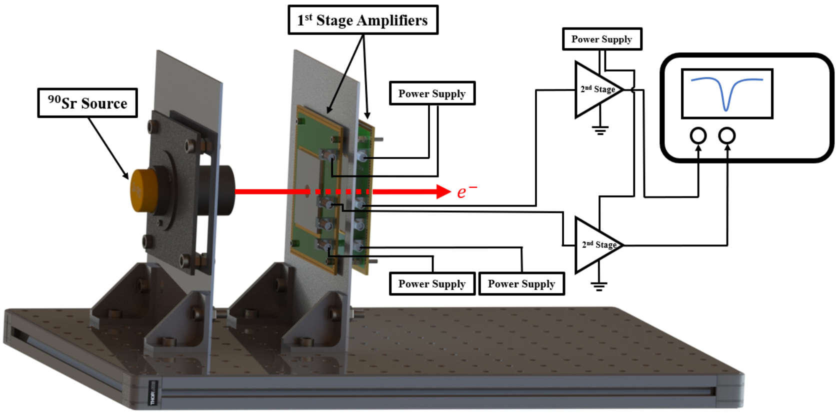
1st Stage Amplifiers
90Sr Source
Power Supply
Power Supply
2nd Stage
e−
2nd Stage
Power Supply
Power Supply

FIGURE 4.3: Schematical representation of the Sr90 source setup.

in signals being measured over distances larger than the inter-pixel spacing, leading to slower signals.

4.2 Timing Calibration

As was discussed in section 1.7.5, the time resolution of a sensor from a system formed by two sensors can be expressed as:

$$\sigma_{DUT} = \sqrt{\sigma_{Total}^2 - \sigma_{ref}^2} \tag{4.1}$$

Where σ_{ref} is the time resolution of the reference sensor, and σ_{Total} the time resolution of the sensors system. Since the Sr90 setup at CNM was not yet used, there was no characterized reference sensor for the system. Therefore, it was necessary to determine the time resolution of a sensor to measure the DUT's time resolution. One way to obtain a sensor's time resolution is by measuring the time resolution of a system consisting of two identical sensors and applying equation 1.31. The usual choice for reference sensors are unirradiated LGADs due to their proven good timing performance before irradiation.

For this setup, two LGADs from the CNM, which will be named A and B, were used as the reference sensors. The gain and the I-V curve of a sensor from the same wafer, which should perform very similarly, are shown in Fig. 4.4. The current (A) and the gain (B) are plotted against the reverse bias voltage in green. These sensors are expected to have a breakdown at about 400 V at room temperature, with a lower breakdown voltage at colder temperatures, and a gain of around 15 at maximum voltage. In [69], similar devices were tested and reported to have time resolutions of the order of 30 ps.

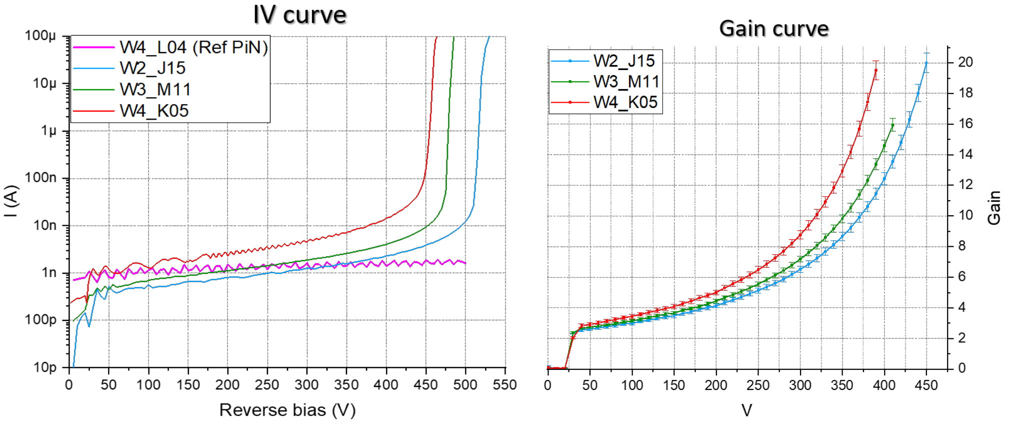

(A) (B)

FIGURE 4.4: Gain (A) and current at rom temperature (B) versus reverse bias voltage from devices from the run 13002 for devices from different wafers. The sensors used for the calibration are from the same run as the sensor in green. Measurements and graphs done by Mr. Jairo Villegas.

The sensors were wire-bonded to the UCSC PCBs by connecting the guard ring to the grounding plane and the central pad to the readout channel, thereby reading only the central pad. The mask diagram of the sensors is shown in Fig. 4.5. Measurements were carried out at low temperatures, and since the cooling process is slow, it was possible to perform measurements at various temperature steps before reaching the final minimum temperature of $-32 \cdot C$.

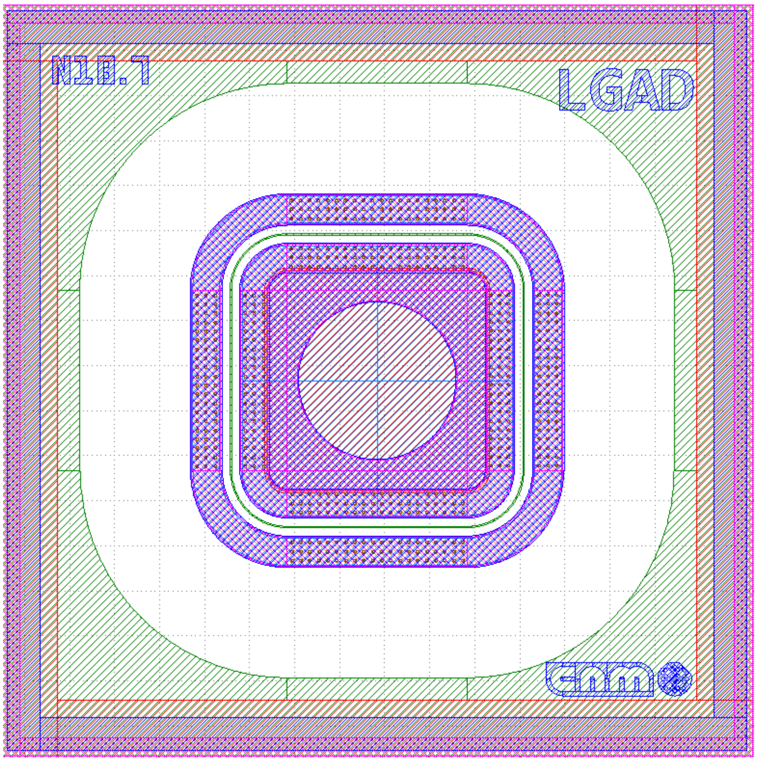

FIGURE 4.5: Mask diagram of the LGAD sensors used for the Sr90 source setup calibration.

The trigger logic system on the oscilloscope was configured so that signals from the channels connected to the sensors had to surpass a threshold of $100mV$ within the same time frame to record the waveforms. Coincident events were enforced to ensure that only waveforms at which a particle crossed both sensors were recorded. The threshold was set high enough to avoid recording noise events, yet low enough to capture valid signals.

In Fig. 4.6 the time resolution (A) and charge collection (B) are presented. At the same bias, both sensors show different charge collections, likely due to variations in gain given by different doping concentrations during fabrication processes. However, charge collected primarily affects the jitter contribution, as Landau fluctuations remain constant with gain [70].

In Fig. 4.6-C, the jitter contributions at each voltage are shown, calculated with $\sigma_{jitter} = t_{rise}/SNR$. The difference in jitter decreases with bias, with a difference lower than 1ps at a bias of $363V$ and a temperature of $-32°C$. Therefore, it is assumed that the time resolution is consistent for both sensors.

From Fig. 4.6, the time resolution of either sensor is determined to be $32.34ps$ at a bias voltage of $363V$, and $35.67ps$ at $375V$. Charge collection

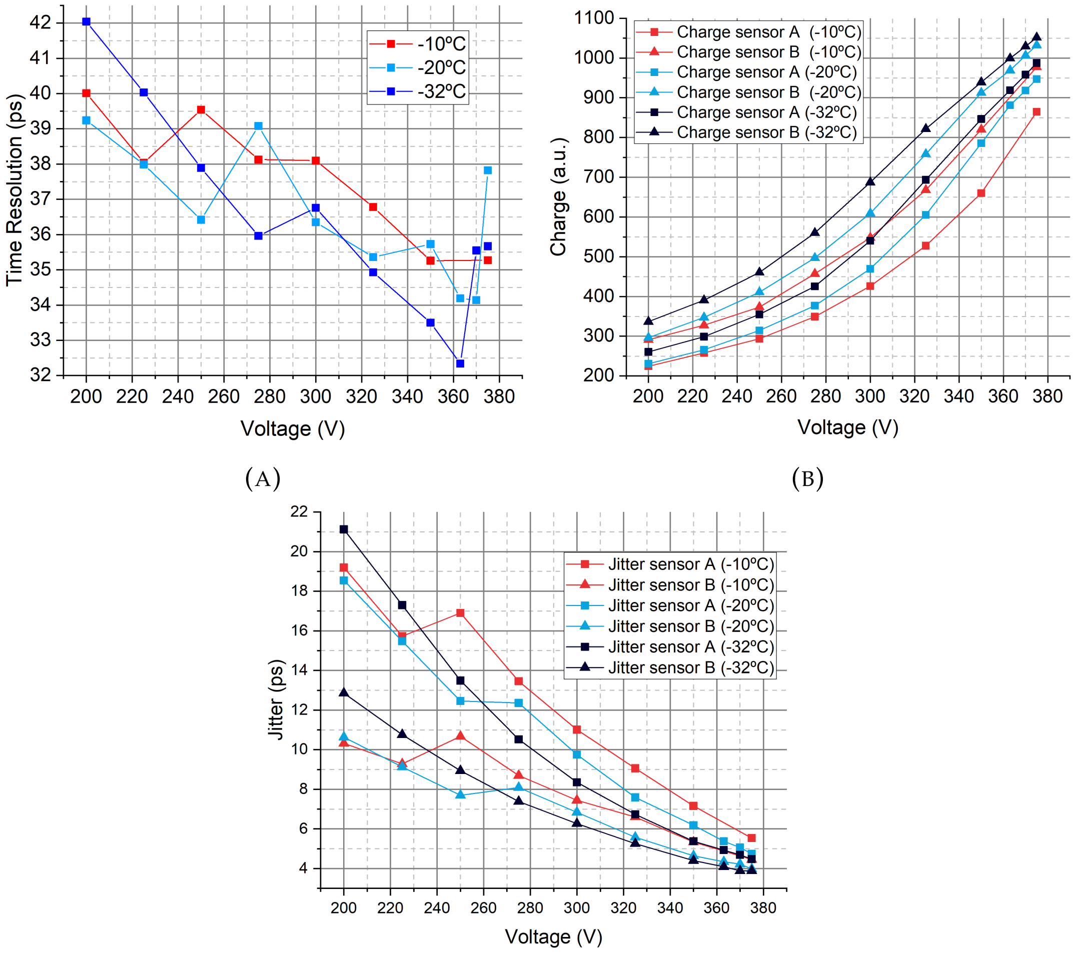

(A)

(B)

(C)

FIGURE 4.6: Time resolution (A), charge collected (B) and the jitter contribution (C) from the CNM LGADs used as reference sensors.

increases as temperature decreases. Additionally, breakdown voltage decreases with temperature, causing noise attributed to leakage current to increase more rapidly at higher applied voltages, thereby degrading time resolution. Therefore, a bias of $363V$ will be applied to the DUT for time resolution measurements.

If a DUT with a time resolution lower than $32.34ps$ is being measured, the reference sensor could bias the results by providing a higher value. However, 3D sensors typically do not achieve time resolutions significantly below this number, so it is considered that the reference LGAD do not change considerably the time resolution of the DUTs studied in this thesis.

4.3 3D Test Structures

The DUTs for this study are the same test structures than those examined with the TCT setup in section 3.5. In contrast with the previous study, the central pixel is connected to the readout channel while the surrounding 8 channels are connected to the ground. Therefore, while all pixels are biased, only the central one is read out.

For meaningful events, a single track of a beta particle must cross both the DUT and the reference sensor. The event rate directly depends on the size of each sensor and their alignment. The LGAD reference has a size of 1.3mm, but the signal from the DUT only originates at the area surrounding the central pixel, which is approximately $55\mu m x 55\mu m$. This results in a low event rate due to the low probability of a beta particle crossing both sensors.

To compensate, a high active radioactive source with an activity of 280MBq was used. Additionally, since each dice contains four samples, two test structures were wire-bonded to the PCB. It was not possible to wire-bond more test structures due to space limitations in the boards resulting from the wire-bonding process.

4.4 Results

Around 3000 waveforms were taken for each fluence level per bias level, and the data analysis was conducted as explained in section 1.7.5, extracting the time resolution of the DUT as follows:

$$\sigma_{3D} = \sqrt{\sigma_{Total}^2 - \sigma_{ref}^2} \tag{4.2}$$

The resulting time resolution, along with the weighting field contribution, jitter and rise times is shown in Fig. 4.8. The study was performed on a non-irradiated devices, and devices irradiated at fluence levels of $1 \cdot 10^{15} n_{eq}/cm^2$ and $1 \cdot 10^{16} n_{eq}/cm^2$. The time resolution is the sigma extracted from the fit to the histogram of ToAs, while the error in the plots are associated with the covariance in the fitting parameters. An example histogram with its fit is presented in Fig. 4.7, corresponding the measurements performed at a fluence level of $1 \cdot 10^{15} n_{eq}/cm^2$ in a bias of 100V, with CFD of 60% for the DUT and 10% for the reference LGAD.

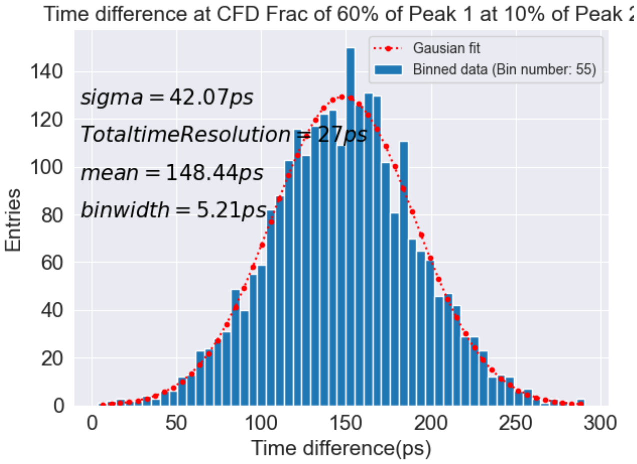

FIGURE 4.7: Sample histogram distribution of the difference in ToA together with the Gaussian fit.

The jitter and rise time are determined from the mean value of the Gaussian fits to the histograms of each measurement, with error bars representing the spread of the Gaussian fit. The weighting field contribution is calculated by considering that, according to equation 1.27, the Landau contribution can be negligible and the time walk effect is highly mitigated by the CFD optimization process. This leaves only two contributions: the electric field/weighting field distortion and the jitter, yielding equation 4.3. The error is calculated by the error propagation from the total time resolution and the jitter plots.

$$\sigma_{wf,3D} = \sqrt{\sigma^2_{Total,3D} - \sigma^2_{jitter,3D}} \tag{4.3}$$

Unirradiated		$1 \cdot 10^{15} n_{eq}/cm^2$		$1 \cdot 10^{16} n_{eq}/cm^2$	
30V	69.02ps	80V	29.09ps	150V	93.54ps
50V	67.98ps	100V	26.77ps	200V	96.86ps
90V	74.84ps	120V	27.03ps	225V	82.51ps
		140V	30.50ps	250V	85.29ps
		160V	43.98ps		

TABLE 4.1: List of the obtained time resolutions with different biases at various fluence levels.

For better readability, time resolutions are listed in Table 4.1. The best time resolution is achieved at fluence level of $1 \cdot 10^{15} n_{eq}/cm^2$, reaching the order of $30ps$. As discussed in section 4.2, the reference sensor's time resolution may bias the results from the DUT. Before irradiation and at fluence level of $1 \cdot 10^{16} n_{eq}/cm^2$ time resolutions are of the order to $70ps$ and $80ps$ respectively, showing that improves after being irradiated, but higher fluence levels worsens its performance. The behaviors are supported by the risetime graph, where a faster risetime is given at $1 \cdot 10^{15} n_{eq}/cm^2$ and a slower for the unirradiated and $1 \cdot 10^{16} n_{eq}/cm^2$.

It is observed for the sensors unirradiated and irradiated at $1 \cdot 10^{15} n_{eq}/cm^2$ that there is an optimal operational bias for time resolution. This is attributed to an increasing noise with higher biases, particularly noticeable at 160V for the fluence level of $1 \cdot 10^{15} n_{eq}/cm^2$, given by a soft breakdown, while maintaining the same risetime. Therefore, what ends up determining the trend of its time resolution is the weighting field distortion, which at higher biases has a greater contribution due to the enhancement of the difference of ToA for the 3Ds at the different hit positions.

Finally, for the fluence level of $1 \cdot 10^{16} n_{eq}/cm^2$ the limiting factor is the jitter, similarly to the unirradiated sensor. While the weighting field distortion factor is kept at a value similar to the previous fluence levels, the higher leakage current and the slower rise times lead to a bigger jitter.

In Fig. 4.9, the signal amplitude and the CCE versus applied bias at different fluence levels are represented. At a fluence level of $1 \cdot 10^{15} n_{eq}/cm^2$ the signal amplitude is higher, similar to the behavior observed in the TCT measurements. However, at the fluence level of $1 \cdot 10^{16} n_{eq}/cm^2$, the signal decreases unless a high bias of $250V$ is applied, which provides the amplitude levels similar to those before irradiation. Regarding CCE, at the fluence level of $1 \cdot 10^{15} n_{eq}/cm^2$ the charge collected decreases compared to before irradiation. In contrast, at the fluence level of $1 \cdot 10^{16} n_{eq}/cm^2$, the CCE increases significantly, reaching between 200% and 300%, indicating charge multiplication given by higher biases.

The discrepancy between the total charge collected and the signal peak height at the fluence level of $1 \cdot 10^{15} n_{eq}/cm^2$ can be attributed to waveform characteristics. A representative waveform is shown in Fig. 4.10. An oscillating reflection noise is observed, which narrows both the integration window and the signal width, resulting in a reduced charge collection compared to the case without reflection contributions. However, the noise occurs after the peak of the signal, and the study of time resolution focuses on the rising edge. Therefore, it is expected that the final time resolution is not affected by the reflection noise, as the signals should be fast even without it. The source of the reflection is yet unknown and requires further investigation.

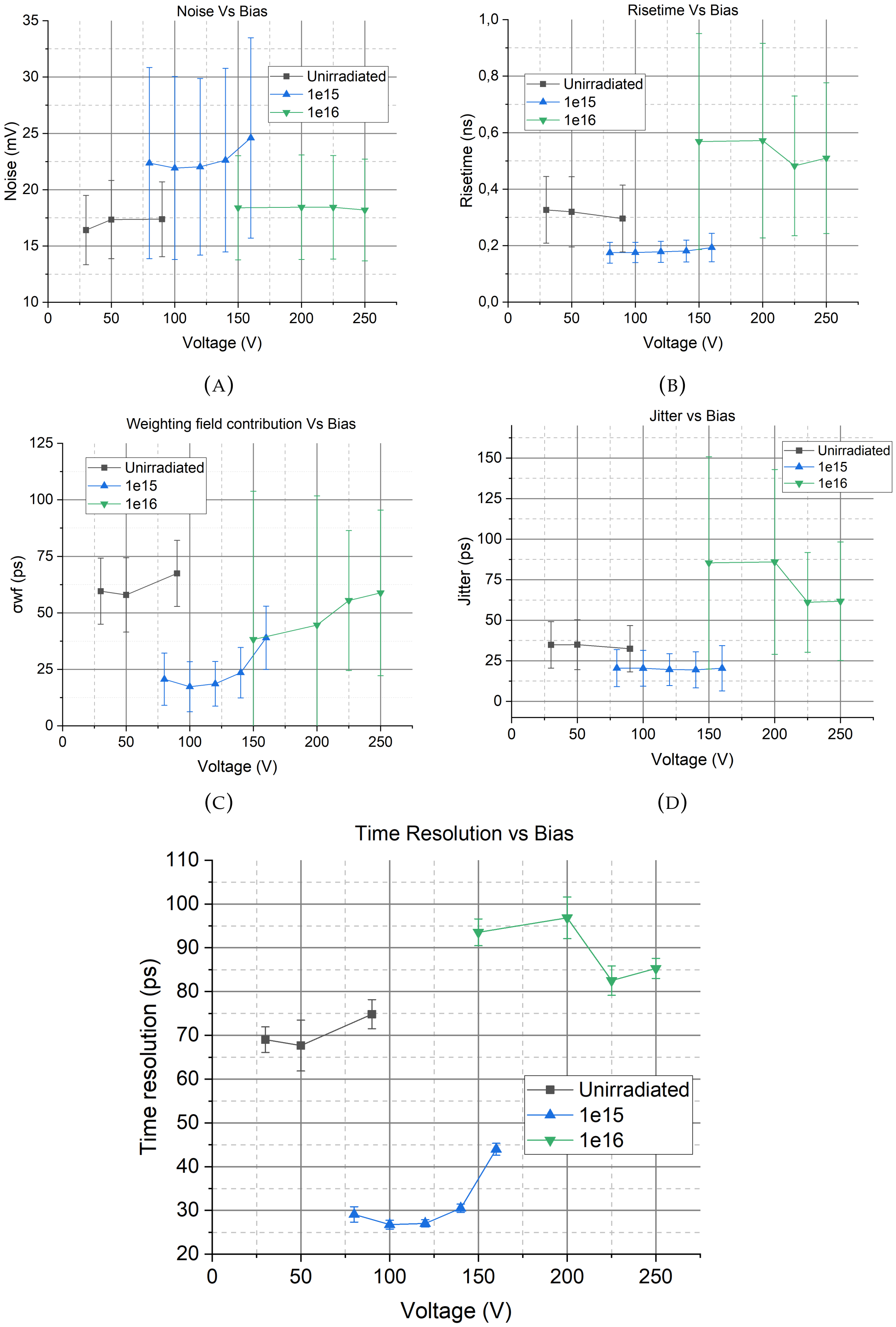

(A) (B)

(C) (D)

(E)

FIGURE 4.8: Graphical representation versus the reverse bias for different fluence levels of: the noise RMS (A), the risetime (B), the weighting field distortion contribution (C), the jitter (D) and the time resolution (E) of the DUT.

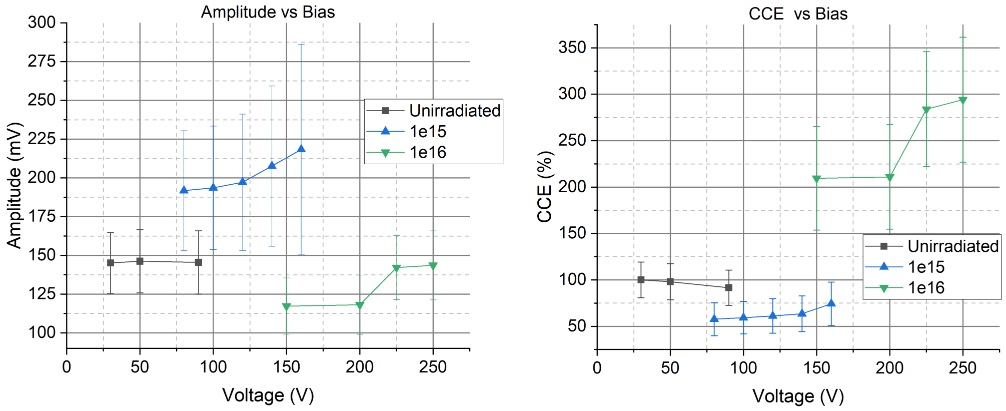

(A) (B)

FIGURE 4.9: Graphical representation versus the reverse bias for different fluence levels of the peak amplitude (A) and the CCE (B).

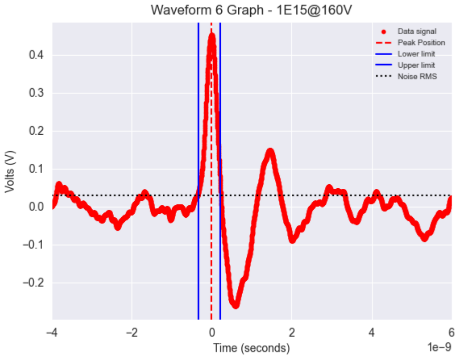

FIGURE 4.10: Sample waveform for the fluence levels of $1 \cdot 10^{15} n_{eq}/cm^2$ (A) at 100V.

4.5 Discussion and future work

In this chapter, the calibration of LGAD sensors in the new radiation source setup at CNM, as well as the first measurements using 3D test structures have been presented and discussed. The sensor used for calibration was an LGAD fabricated at the CNM facilities with a time resolution of $32.5 ps$ at -32ºC and a bias voltage of $363V$, determined by analyzing coincident signals from two identical sensors from the same run. One of these sensors was later used as the reference sensor for future measurements, with the DUTs in this work being the 3D n-on-n test structures. These test structures were irradiated at neutron equivalent fluence levels of $1 \cdot 10^{15} n_{eq}/cm^2$ and $1 \cdot 10^{16} n_{eq}/cm^2$, as well as a non-irradiated sample to compare the performance before and after exposure to harsh radiation environments. The time resolution for these sensors ranged from $27ps$ to $93ps$, depending on the fluence level and the bias.

Time resolution studies also show that until the highest fluence levels, the most dominant contribution to the time resolution is the weighting field distortion, which refers to the dependence of the time resolution on the hit position of the impinging particle. At the fluence level of $1 \cdot 10^{16} n_{eq}/cm^2$ the dominant factor was jitter, due to a a combination of the slower rise time and the higher noise attributed to the increased leakage current coming from the bulk defects.

The charge collection efficiency was shown to be more than 100% for the fluence level of $1 \cdot 10^{16} n_{eq}/cm^2$ due to charge multiplication. For the fluence level of $1 \cdot 10^{15} n_{eq}/cm^2$ it was found to be lower, which was attributed to the deformation of the tail in the waveforms due to signal reflection that made the signal narrower. The signal amplitude was found to be much larger for this particular fluence level, so it is expected that for a cleaner signal, the charge would be above 100% as well.

The charge collection efficiency was shown to be more than 100% for the fluence level of $1 \cdot 10^{16}\ n_{eq}/\mathrm{cm}^2$ due to charge multiplication. For the fluence level of $1 \cdot 10^{15}\ n_{eq}/\mathrm{cm}^2$, it was found to be lower, which was attributed to the deformation of the tail in the waveforms due to signal reflection that made the peak narrower. The large signal amplitude suggests that a signal with no reflections would result in a CCE above 100%.

As future work, it would be essential to eliminate the signal reflection observed at the fluence level of of $1 \cdot 10^{15} n_{eq}/cm^2$, which may be due to an impedance missmatch along the transmission line [71]. The fact that this issue was only found on the board from this specific fluence level suggests that the board may have a different total impedance than the others due to a fabrication issue or degradation effect, resulting in signal reflection that cuts off the tail and misleads charge collection efficiency studies. Furthermore, studies on other fluence levels should be conducted, especially for the highly irradiated samples, as they are the closest to the expected accumulated radiation doses in the FCC collider.

Chapter 5

3D sensors for Timing Applications

As discussed in section 1.1.3, the FCC is estimated that will feature an instant luminosity of more than $10^{34} cm^{-2} s^{-1}$. The high luminosity imply that in order to resolve events in time, as well as in space, the silicon sensors built within the experiments must have a time resolution of the order of $30 ps$ [72], which has to be fulfilled throughout the whole lifespan of the runs, hence requiring as well an excellent radiation hardness. As highlighted in the previous chapters, 3D silicon sensors are considered the best candidate to withstand the high radiation doses in the FCC. Despite of that, its time resolution does not fulfill the requirement at all stages, specially after receiving substantial radiation exposure. In this chapter, a new configuration for 3D sensors designed to improve its time resolution is going to be explored, by means of electrical characterization and complemented with simulations.

5.1 Architecture and Geometry

In 3D devices, the active thickness is independent of collection time. However, the amount of charge generated by an ionizing particle is not independent since the charge generation occurs within the active thickness of the sensor. Thus, a greater active thickness results in more charge generation and a larger induced signal. As observed in run 10339, signal height significantly influences both charge collection efficiency and time resolution by providing a better signal-to-noise ratio (SNR). Therefore, a production run at CNM has produced 3D silicon sensors built on $285 \mu m$ thick wafers using a double-sided process. In this process, electrode holes are etched from both sides of the wafer, making its entire thickness the active thickness. One of the complications in a double sided process in a thicker wafer is the necessity of a high Aspect Ratio (AR) for the DRIE process, that is, the ratio between the depth of the etched column and its width.

In the clean room facilities at CNM, the highest aspect ratio achieved is approximately 25. To prevent a short between the frontside and the backside, it is crucial that the columns and the diffusion of dopants from the highly doped electrodes do not penetrate through to the other side. Therefore, a column depth short of about $30 - 40\mu m$ from the total thickness is necessary. Given that the wafers are $285\mu m$ thick, the column depth would be approximately 250 μm. To achieve an AR of 25, a column diameter of $10\mu m$ is required.

The most widely used pixel distribution for sensors is in an orthogonal array, due to the direct translation from a pixel hit position to Cartesian coordinates, and hence having specific read-out chips to be tested with. Despite of that, it is known that the most space-optimized pixel distribution is an hexagonal one, for with this configuration the maximum distance from the n+ electrode is then reduced by 88% when compared with the usual orthogonal distribution [73]. This distance reduction would then be translated into faster signals (and larger signals), less charge trapping probability and a lower full depletion voltage, thus improving both radiation hardness and time resolutions. Moreover, the reduction of the furthest distance also would slightly decrease the difference in electric field over a single pixel cell, which would decrease as well the weighting field contribution to the time resolution of the sensor. In order to study the difference between both geometry distributions, test sensors with hexagonal and orthogonal geometries have been fabricated in a production run at CNM, built in different pixel arrays and sizes with p-type wafers. The distance between pixels in an orthogonal geometry is defined as the pixel pitch. Since there is not a pitch in the X and the Y axis for an hexagonal geometry, the same labeling cannot be used. In order to reference the size of a pixel cell, the radius of a circle that intersects the p+ electrodes with the n+ electrode at its center is used. For this run, p-n radius distances of $30\mu m$ and $50\mu m$ were used. The mask design for the hexagonal geometry with the two different p-n radius distances are shown in Fig. 5.1.

This production run successfully fabricated 3 wafers including devices with different pixel arrays and geometries. It features 7 different types of test structures: two of them (1-X and 2-X) consist of a single pixel surrounded by a guard ring, in the same fashion as the ones studied in the n-on-n case (section 2.1), being one with an orthogonal 55 x 55 μm pixel pitch with 8 surrounding pixels, and the other a hexagonal distribution with a p-n radius distance of 50 μm and the central column surrounded by 6 pixels. The other

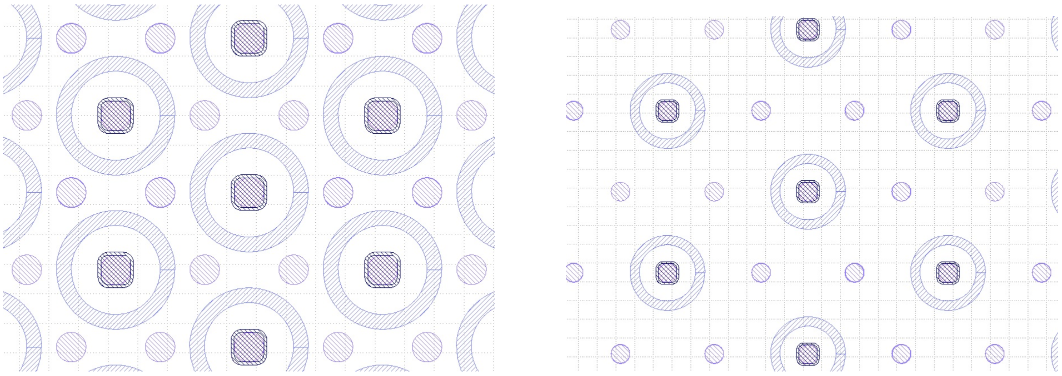

(A) (B)

FIGURE 5.1: Mask designs for the hexagonal distribution of electrodes for the 3D sensor with a p-n radius distances of 30μm (A) and 50μm (B).

test structures consist of pixel arrays with both orthogonal geometry with a pixel pitch of 50 x 50 μm and a hexagonal with a p-n radius distance of 30 μm in arrays of 5 x 5 and 10 x 10 pixels. Additionally, two pad diode are featured with an array of 100 x 100 pixels in an orthogonal geometry with a pixel pitch of 50 μm x 50μm, with all pixels shorted with a highly doped polysilicon in order to reduce laser reflection with a TCT setup.

Besides the test structures, samples designed to be mounted on specific ASICs have been fabricated, specifically for ALTIROC and MEDIPIX:

- ALTIROC: Fast timing readout chip with a time resolution of 25ps designed to fit pixels with an area of 1.3 x 1.3mm^2 [74]. Since the distance between pixels for 3Ds is coupled with the distance between electrodes, therefore a large area for a pixel would require large travelling distances for the drifting carriers, hence losing the short inter-electrode distance that make 3D sensors radiation hard sensors. For that, shorted arrays of electrodes have been created in order to test 3D sensors with a fast timing ASIC such as the ALTIROC, including hexagonal arrays with p-n distances of 30μm and 50μm.

- MEDIPIX 3: array of 256x256 pixels with a pixel pitch of 55 $\mu m x$ 55μm and including a guard ring. The device fits for a readout chip designed for medical imaging by acting as a camera with the capability of colour imaging and free of dead time [75]. This sensor does not have the pixels shorted with temporary metal, so it is not going to be considered for this thesis.

5.2 Electrical Characterization

I-V and C-V curves have been taken for some of the samples of the 3 fabricated wafers, which are labeled as wafer 4, 5 and 6. Measurements were carried out with the Cascade probe station at the Radiation Detector Laboratory at CNM, using a Keithley 2410 for biasing and readout of the current, an ESPEC ETC-200L for temperature control, and Agilent 4284A LCR for capacitance measurements, more detail in section 2.2. The studied devices have been the 1-X and 2-X devices, for they allow for the study of single pixels. Moreover, some of the arrays within the ALTIROC pixels have been measured in order to study the effect of different amount of pixels in arrays, including arrays from 5 x 5 pixels to 20 x 20 pixels. Finally, the 3-X have been measured in order to study the behavior in the case of a large array of 100 x 100 pixels.

In Fig. 5.2 the I-Vs for devices 1-X and 2-X, which correspond to a single central n+ column surround by 6 (8) n+ electrodes, with hexagonal (orthogonal) geometry with 50μm of p-n distance (55 x 55 μm of pixel pitch). The shown currents are the ones taken for the single central column, although the measurements were taken with the corresponding guard ring connected as well, in order to replicate an electrode fully surrounded by working pixels. When comparing the results from Fig.5.2 with the ideal I-V curve from a p-n junction (see Fig. 1.7), the current does not reach a saturation value, but does keep increasing with bias, and for some cases the current reaches the compliance value with less than 10V in some cases.

The I-V curves for some of the samples for the ALTIROC chip featuring different pixel array sizes, are shown in Fig. 5.3, with the current normalized as the current per pixel. In contrast with the curves in Fig. 5.2, some of the devices do have a diode-like I-V curve. When comparing the array size, the ones with fewer amount of pixels per sample (represented with green tones) have a larger amount of current with respect to larger arrays, specially being noticeable with the 20x20 array having the lowest of the currents. The dependency of the current per pixel with the sample size can be attributed to a surface current contribution.

I-V curves were also taken at low temperature, shown in Fig. 5.4. Similarly as in Fig. 5.2, the current rapidly increases not showing the expected saturation current from an ideal diode, specially at high biases. At low biases, some of the devices do show a saturation that eventually increases getting to the same current as the ones with high leakage current. At these low biases

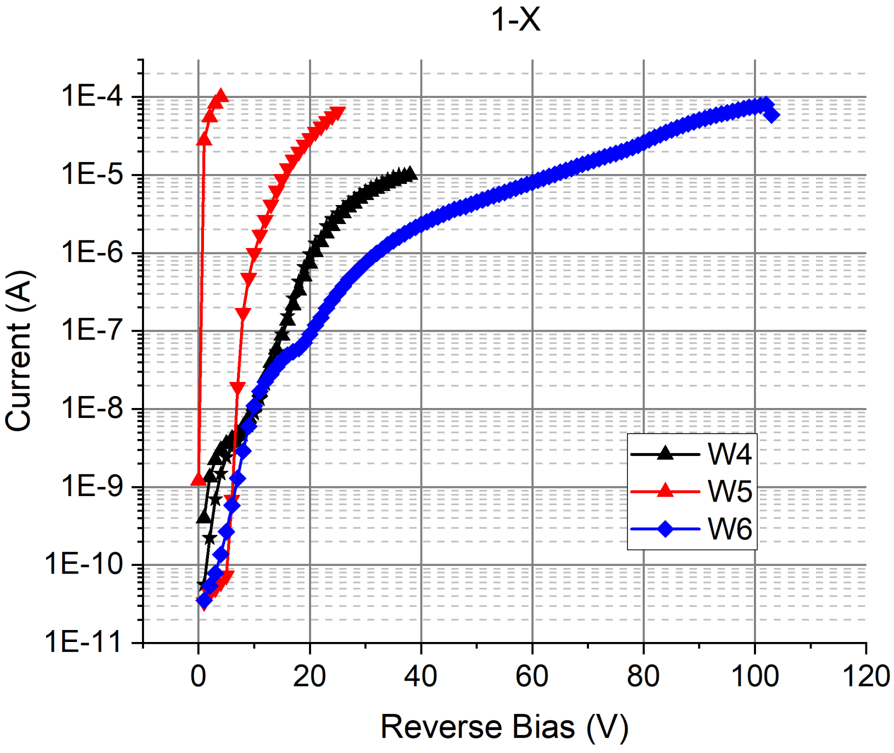

(A)

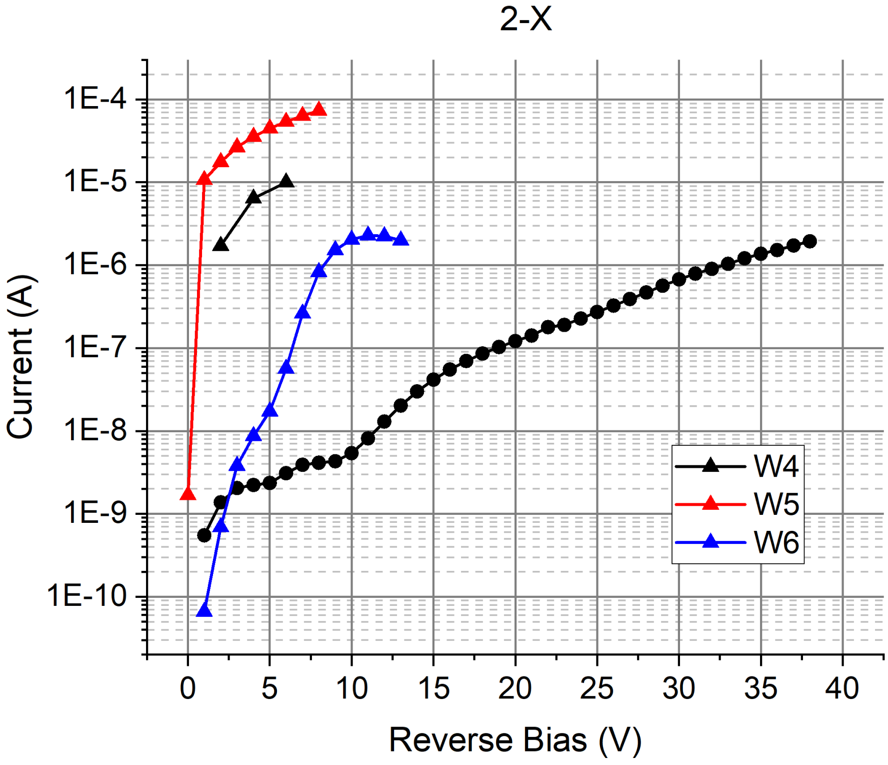

(B)

FIGURE 5.2: I-V curves taken from 1-X (A) and 2-X (B) devices from wafer 4, 5 and 6. Attention must be paid to the scale of the x-axis, being the one for the 1-X (hexagonal) larger than the ones for the 2-X (orthogonal).

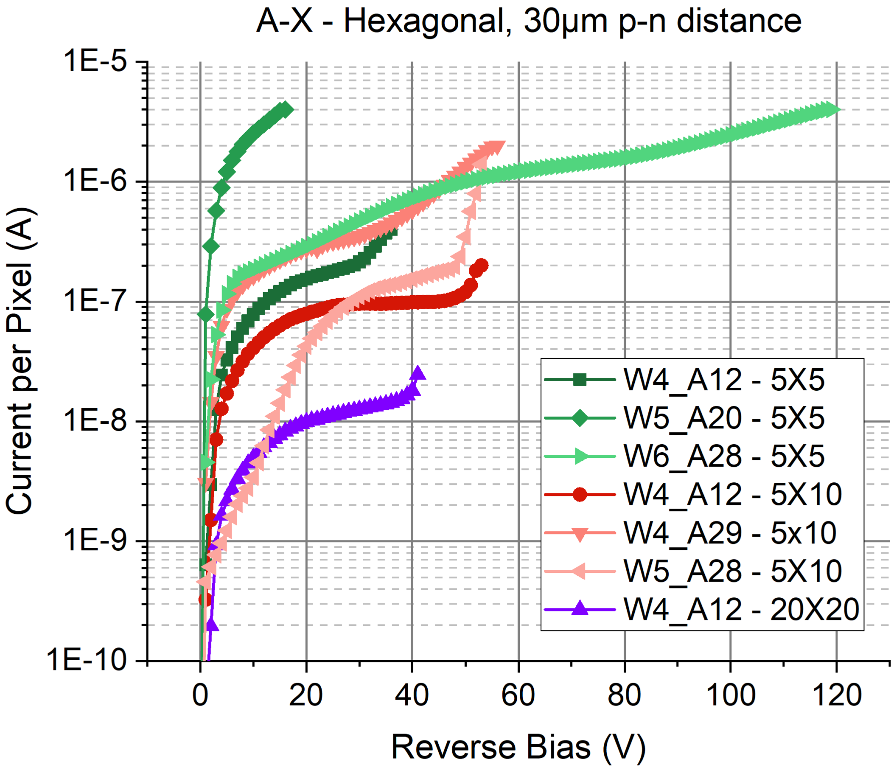

(A)

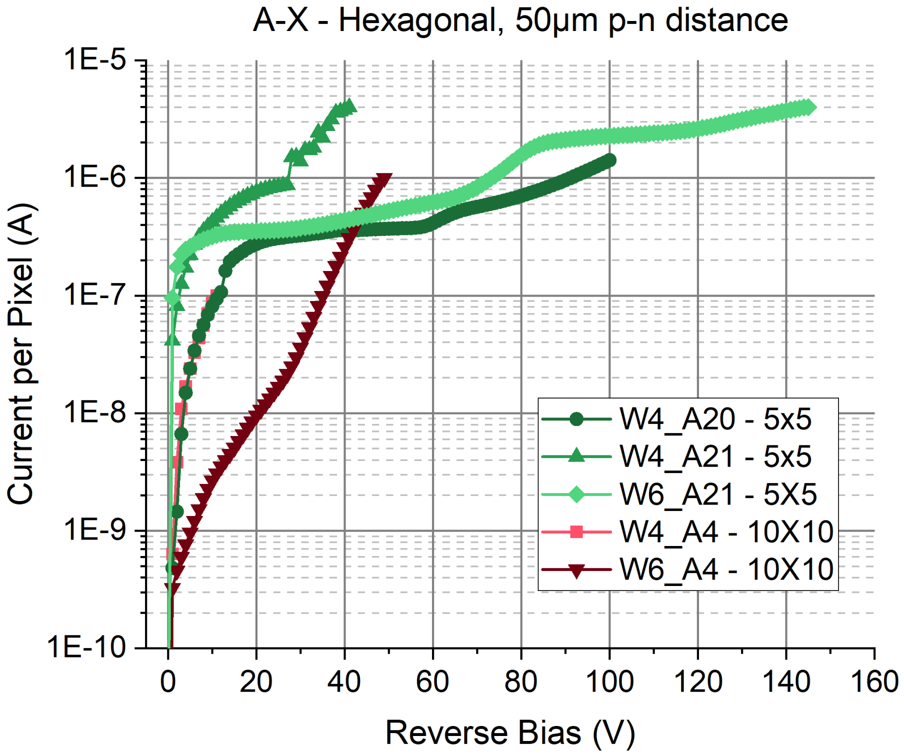

(B)

FIGURE 5.3: I-V curves taken from ALTIROC pixels, which feature different array sizes, with electrodes in hexagonal arrays with p-n distances of 30 μm (A) and 50 μm (B).

at which there is some saturation, there is difference between the current at room temperature and low temperature, while at high biases, there is almost none. Therefore, the high leakage current that does not depend on temperature indicate a surface current that becomes dominant in higher electric field.

Despite the high surface leakage current, the devices should be able to operate correctly if the maximum bias is higher than the full depletion voltage of the sensor. The $1/C^2$ vs V curves show the evolution of the depletion volume with increasing bias. Since the capacitance of a single column is lower than the noise capacitance of the measuring setup, it is more convenient to measure the capacitance with the biggest array possible, due to the fact that the total capacitance of an array of 3D pixels shorted all together is the sum of each individual capacitance within the array since they are connected in parallel. The largest pad featured in the mask are the $100x100$ arrays with orthogonal geometry, with a pixel pitch of 50 μm. The resulting curves are shown in Fig. 5.5. Within a range of $20V$, the curve does not reach a fully flat plateau, although the slope of the curve decreases with voltage, meaning that in the first place there is a quick depletion, but afterwards the depletion volume increases slowly. This can be attributed to a fast lateral depletion between columns, a slower depletion occur at the bottom of the n+ electrode. This effect will be further explored and studied in the simulations, in section 5.3.2.

$1/C^2$ vs V curves were also taken for some of the ALTIROC pixels, featuring the hexagonal geometry with 30 μm p-n distance, including different array sizes. The capacitance was normalized for the amount of pixels within the sample, and since the value of the capacitance mostly depends on the geometry, all of them should have a very similar value. The ones with the lower $1/C$ are the ones that have the lower amount of pixels per array, being the one with the lowest with 25, followed by 5x10 and 10x20 and with the highest, 20x20. This can be attributed to the larger leakage current per surface area found in Fig. 5.3, since the higher leakage current may lead to a behavior less similar to a capacitor, hence decreasing the capacitance and decreasing the $1/C$ value.

5.3 TCAD Simulations

In order to further understand the difference in depletion volume with bias, as well as the electric field distribution and uniformity, TCAD simulations have been carried out for the hexagonal geometries with p-n radius distances

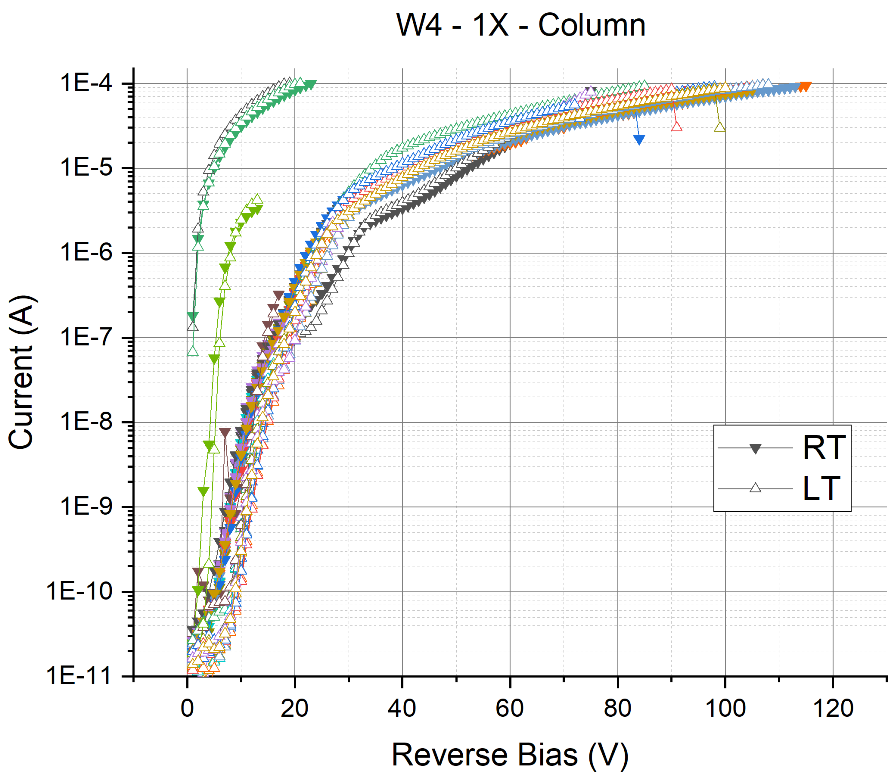

(A)

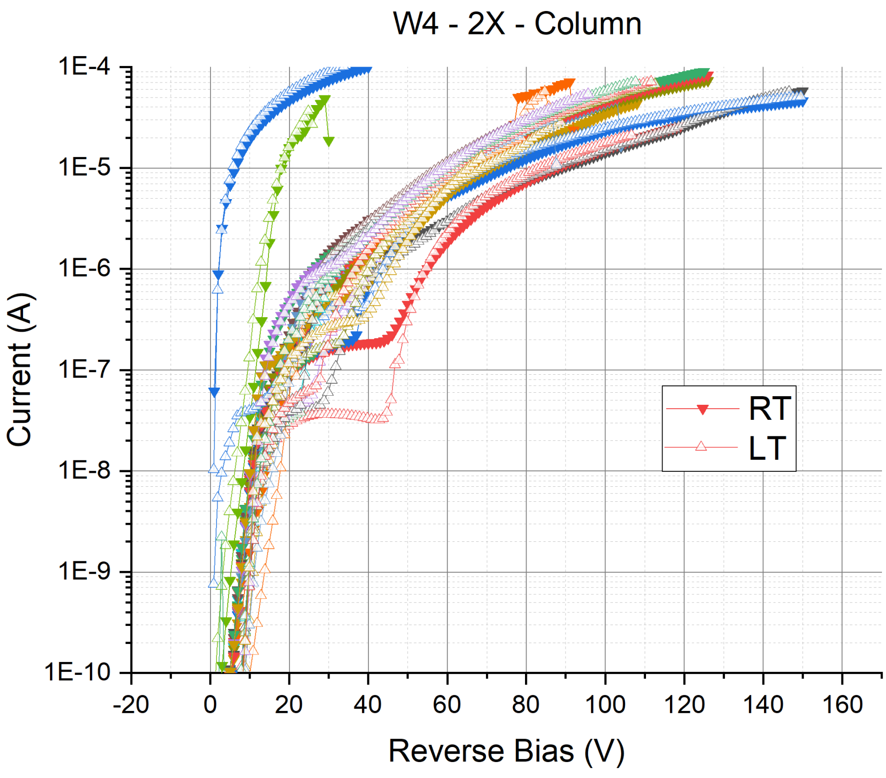

(B)

FIGURE 5.4: I-V curves taken from test structure with hexagonal (A) and orthogonal (B) geometries, taken at room temperature (red) and low temperature (blue).

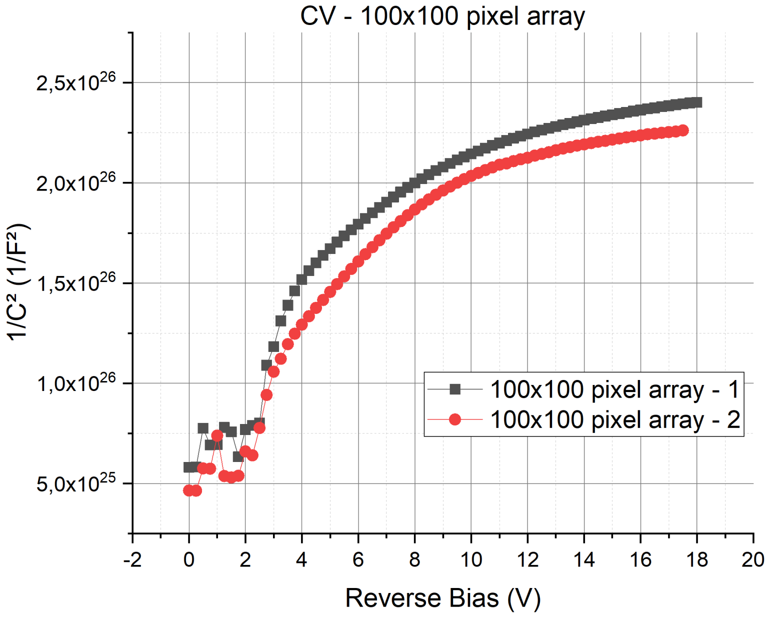

FIGURE 5.5: Representation of $1/C^2$ versus bias for 100x100 pixel arrays, represented as the quantity per pixel.

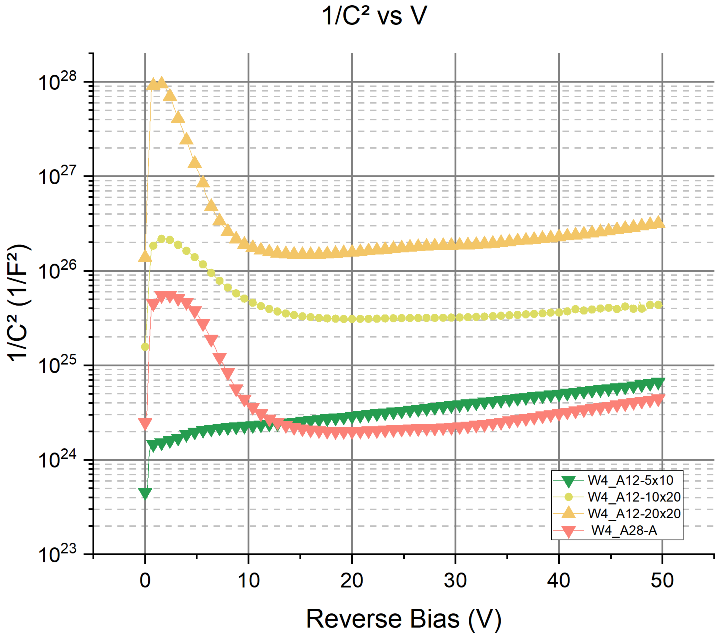

FIGURE 5.6: Representation of $1/C^2$ versus bias for different pixel arrays within the ALTIROC devices, represented as the quantity per pixel.

of 30 μm and 50 μm, as well as for the orthogonal geometry with a pixel pitch of 50 μm. All simulations have been set at a temperature of $-20°C$ and the electrical simulations have been performed by using the models described in section 1.8 and further described in appendix A.

5.3.1 Structure models

To simulate the behavior of a sensor with a specific architecture, the mesh of the materials along with their doping concentrations must be created. The structures have been simulated in 3 dimensions, for 3D sensors have higher electric fields close to the p-stop and at the tips of the columnar electrodes, which should not be neglected. The bulk has been defined as a rectangular prism 285μm thick of silicon with the lateral dimensions that are characteristic for each geometry and configuration, and the electrodes have been defined as poly-silicon cylinders 250μm deep and 10μm wide. For all the devices, the peak doping concentration is $1 \cdot 10^{20}\ cm^{-3}$ for the n-electrodes, $5 \cdot 10^{19}\ cm^{-3}$ for the p-electrodes, $4 \cdot 10^{16}\ cm^{-3}$ in the p-stop and $1 \cdot 10^{12}\ cm^{-3}$ for the bulk doping concentration. These specific values are the ones aimed for during the production of the sensors, which should represent a realistic case. Additionally, a Gaussian diffusion profile has been established so that dopants diffuse from regions of high doping concentration to regions of lower concentration. The diffusion depth is set as 1 μm deep, meaning that the doping concentration decreases a factor $1/e$ at a distance of 1 μm from the point of maximum doping concentration.

One of the potential issues in the simulations of 3D structures is the long computational time due to the larger amount of meshing points to be considered. Therefore, it is preferable to make use of the symmetries within the geometry in order to reduce the amount of meshing points. For the orthogonal distribution, with only a quarter of a single pixel it is possible to recreate a lattice of pixels by applying mirror symmetries to the X and the Y axis. The hexagonal pattern, however, can not be reproduced in the same way. Instead, the region to be simulated is the one involving from the center of an n-type column to a neighbouring one, as shown in Fig. 5.7. With a two-pixel configuration, then it is possible to reproduce the full lattice with a hexagonal geometry.

By applying the doping concentrations to the structures defined with their respective materials, the resulting devices are the ones shown in Fig. 5.8 with an outside view, while a cross-section is shown in Fig. 5.9. In the legend,

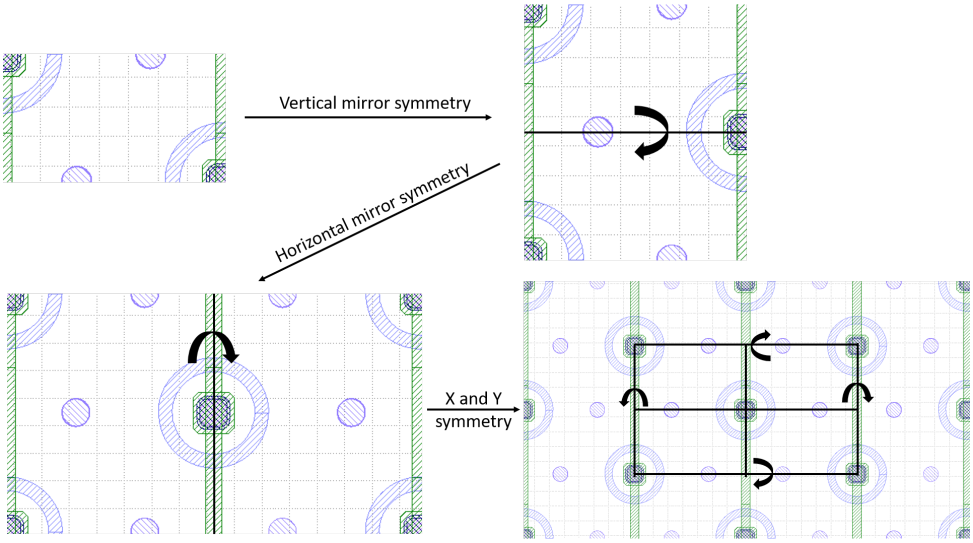
Vertical mirror symmetry
Horizontal mirror symmetry
X and Y
symmetry

FIGURE 5.7: Graphical representation of the symmetries applied by using images of the mask layout. The n-type electrodes are inside the p-stop while the p-type are found in between them.

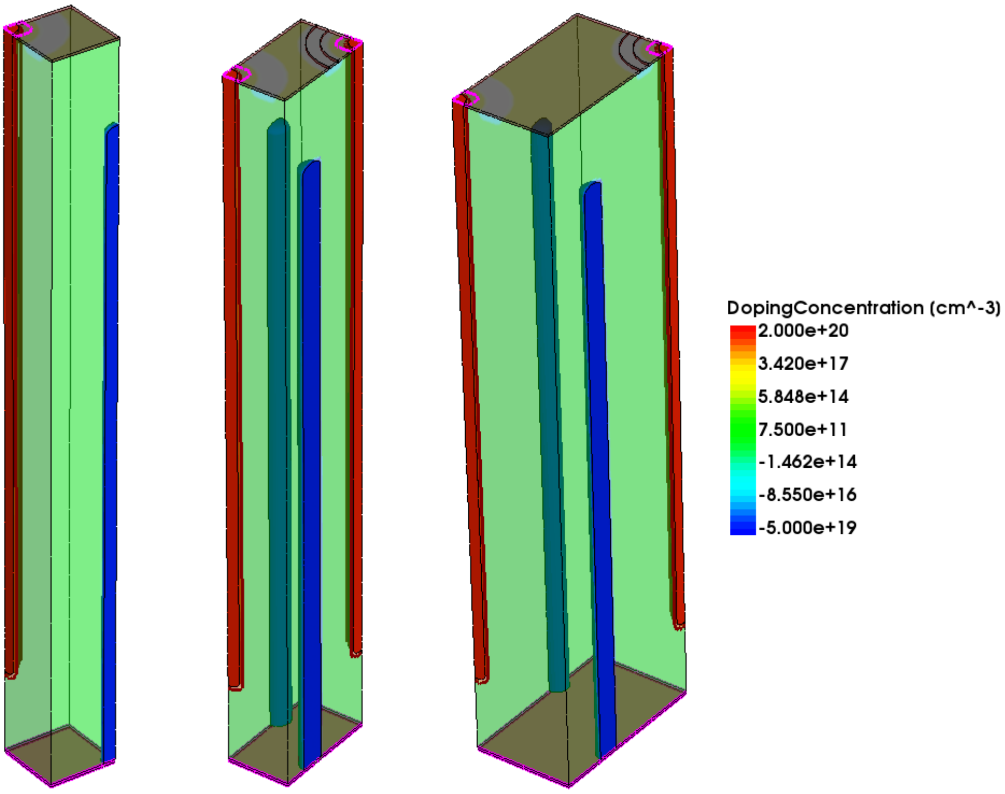
DopingConcentration (cm^-3)
2.000e+20
3.420e+17
5.848e+14
7.500e+11
-1.462e+14
-8.550e+16
-5.000e+19

(A) (B) (C) (D)

FIGURE 5.8: Simulated structures for the orthogonal geometry (A) and hexagonal geometries with p-n distances of 30 μm (B) and 50 μm (C). A legend for the doping concentrations is presented (D).

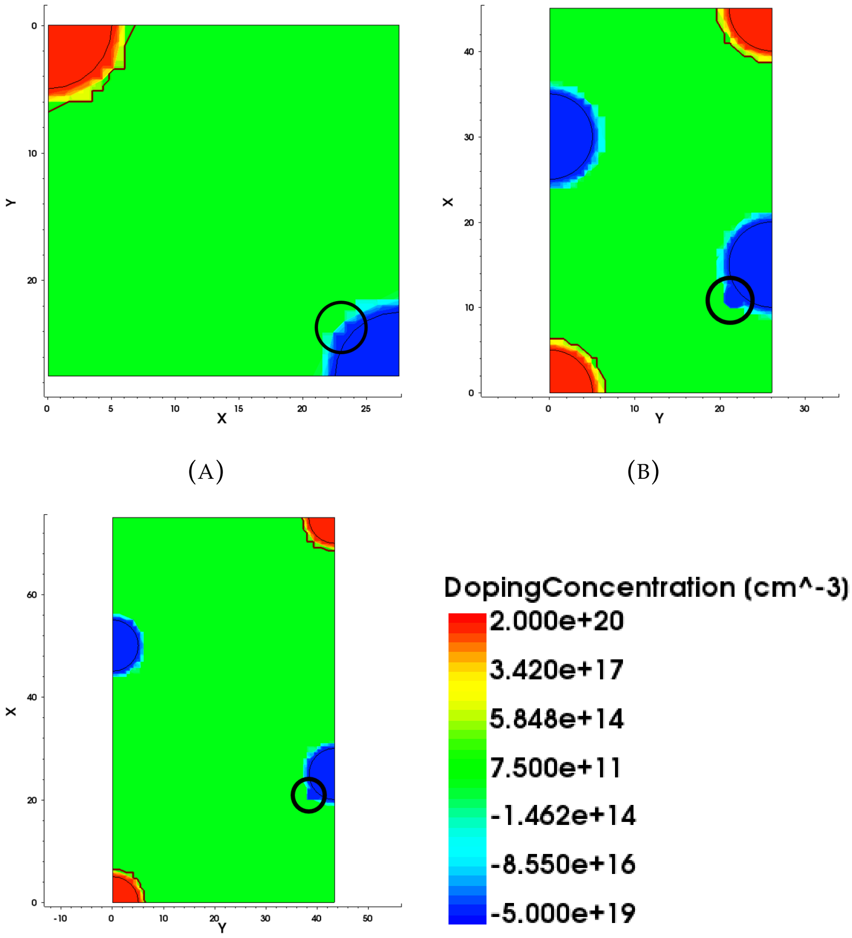

(A)

(B)

(C)

(D)

FIGURE 5.9: Cross sections of the doping concentration from the simulated structures of Fig. 5.8 for the orthogonal geometry (A) and hexagonal geometries with p-n radius distances of 30 μm (B) and 50 μm (C). A legend for the doping concentrations is presented (D).

positive values indicate phosphorous (n-type) doping concentrations represented in red, while negative values represent boron (p-type) doping concentrations in blue. The green region denotes the doping in the bulk region, while the magenta color highlights the contour of the contact metallization area, in which the voltage is applied as well as the acting as the read-out area.

In the cross-section view it is highlighted with circles that there are some protrusions of the doping concentration at the p-type electrodes, which does not represent a real case. These artifacts are due to the adaptation of the meshing at the tip of the column, resulting in inaccuracies that could not be eliminated despite various adjustments to the meshing. Despite of that, as will be seen in the next section, this artifact does not translate to a significant effect in the electric field. Therefore, its effect should be neglected and should not affect the final outcome and conclusions for which this chapter aims for.

5.3.2 Electrical Characteristics

In order to simulate the electrical properties, the sdevice module from the Sentaurus software has been used. It solves the Poisson equation with specified contour conditions, which in this case is the electrical potential applied in each of the contacts defined within the structure. Therefore, by setting a voltage of 0 at the p-type electrodes and a positive voltage at the n-type electrodes, it effectively puts the p-n configuration in a reverse mode. The resulting electric fields are shown in figures 5.12 for the orthogonal, 5.14 for the hexagonal with a p-n radius distance of 30 μm, and 5.16 for the hexagonal with a p-n radius distance of 50 μm, with their respective cross-sections in figures 5.13, 5.15 and 5.17. In them, a scale of colors for the absolute value of the electric field is represented from lower values in blue to the larger in red. A white line represents the depleted region, originating from the n-type column which can be distinguished from the p-type electrode by the p-stop surrounding it.

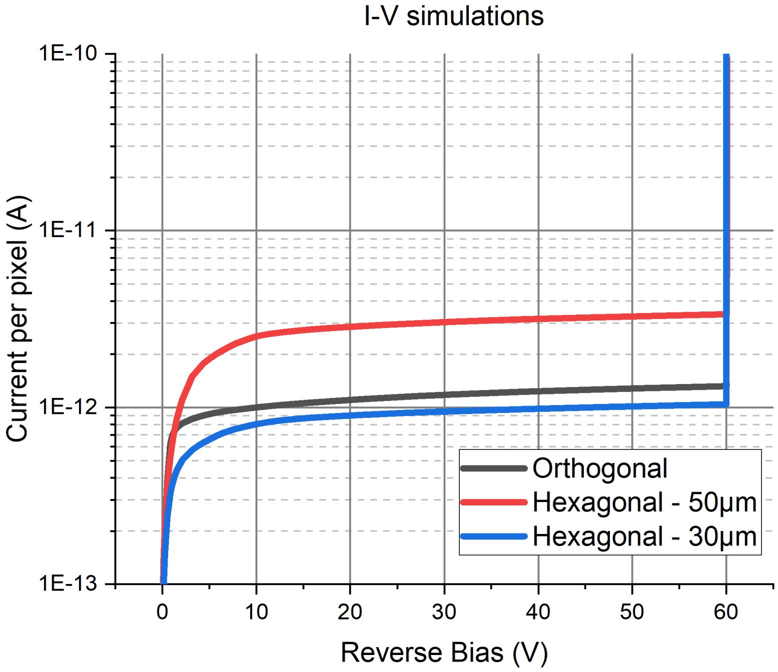

FIGURE 5.10: I-V curves resulting from the simulations for the different geometries. The leakage current saturates at below 10V while the breakdown occurs at 60V.

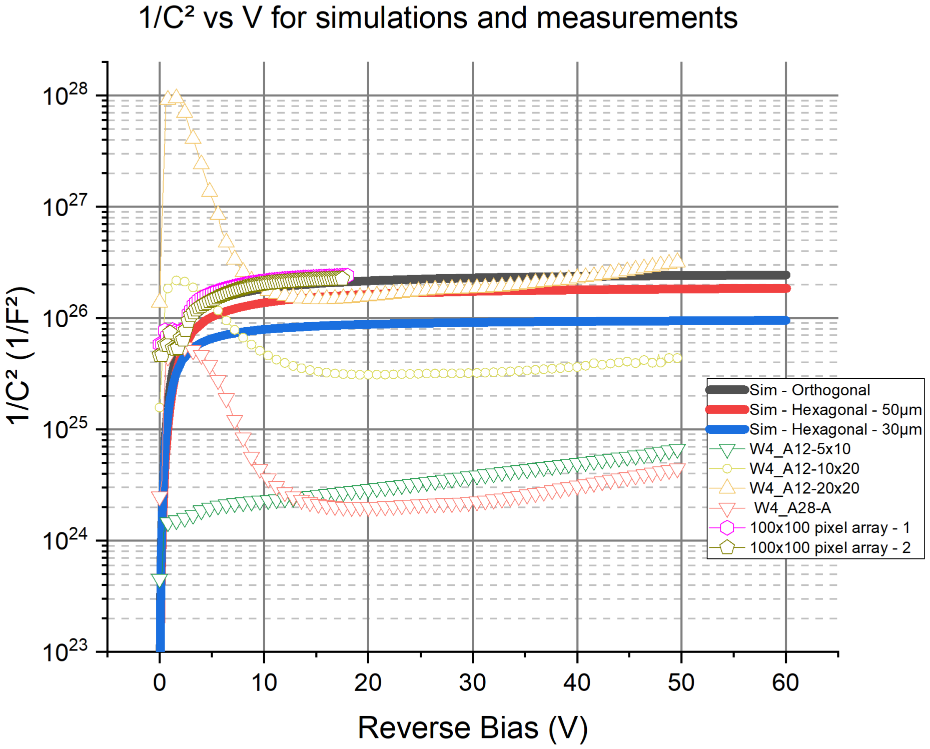

FIGURE 5.11: $1/C^2$ vs V from simulations (straight line) and measurements (empty symbols).

By extracting the output current at an n-type electrode, the I-V curves can be obtained, and are represented at Fig. 5.10 with the current normalized for one pixel. They show a breakdown occurring at 60V, while the leakage current reach a plateau at less than 10V, specially for the smaller-sized pixel cells, which are the orthogonal and the hexagonal with the p-n distance of 30 μm. Hence, the electric fields are shown at biases of 1V, 5V, 10V and 60V to depict the evolution of the depletion region. Additionally, $1/C^2$ vs V simulations have been performed, shown in Fig. 5.11, and compared with the C-V curves from Figs. 5.5 and 5.6. The curves from the 100x100 arrays fit with the simulations, while the measurements with the hexagonal geometries only fit the one with the bigger array of 20x20. Therefore, only the larger arrays fit with the values of the capacitance from the simulations. The high surface leakage current change the measured capacitance in the case of the smaller samples, similarly as discussed in section 2.2.2 and explained in [53], where high leakage current yield a higher capacity due to the effective addition of a resistance in parallel to the equivalent circuit.

5.3.3 Electric Field Distribution and Uniformity

When comparing the distribution of the electric field from figures 5.12, 5.14 and 5.16, the three cases show a similar general behavior: the regions with the highest electric fields are near the p-stop and at the tips of the columnar electrodes for higher biases. At the p-stop with just a few volts already shows a significantly higher electric field than the rest of the structure. However, the depletion region shows that in any of the structures, with just $1V$ they are not fully depleted in the lateral direction, specially in the case of the hexagonal 50 μm p-n distance, in which the region between pixels is not yet depleted at all, while for the 30 μm p-n distance is, although not near the p-type electrodes. At $5V$, all the structures are already fully depleted laterally, but all of them feature a non-depleted region at backside, which gets gradually depleted with increasing bias, reaching an effective full depletion at $60V$. Therefore, simulations show that, while the lateral depletion occur with just a few volts, some more bias needs to be applied so that the backside gets fully depleted, being that the case for any of the configurations.

The figures showing the electric field along a cross section cut depict how the region in between pixels feature a low absolute value of the electric field, which is a common phenomenon across all the 3D pixel sensors. Despite of that, it is still important to know which configurations feature a more uniform electric field. One of the relevant contributions to the time resolution is the non-uniformity of the electric field at the plane perpendicular to the hitting particles, due to yielding a distribution of rise-times which degrade the time resolution. Therefore, an important factor to determine a better performing configuration for timing measurements, would be the study and comparison of the uniformity of the electric field within the three configurations. Since there is no specific figure of merit for the uniformity of the electric field, 2D histograms have been performed which show the frequency at which there is a certain absolute value of the electric field at a given distance from the electrode located at the position (0,0), at a bias voltage of 60V within a cross section plane. The resulting 2D histograms are shown at Fig. 5.18, with the orthogonal geometry found at A, the hexagonal with a p-n radius distance of 30 μm at B and the hexagonal with a p-n radius distance of 50 μm at C. For the hexagonal geometry, only the points corresponding to the cell of the n-type electrode located at the (0,0) have been considered, so that only one cell is analyzed at a time and consequently can be compared to the orthogonal geometry. The separation has been set by a straight line crossing both p-type electrodes.

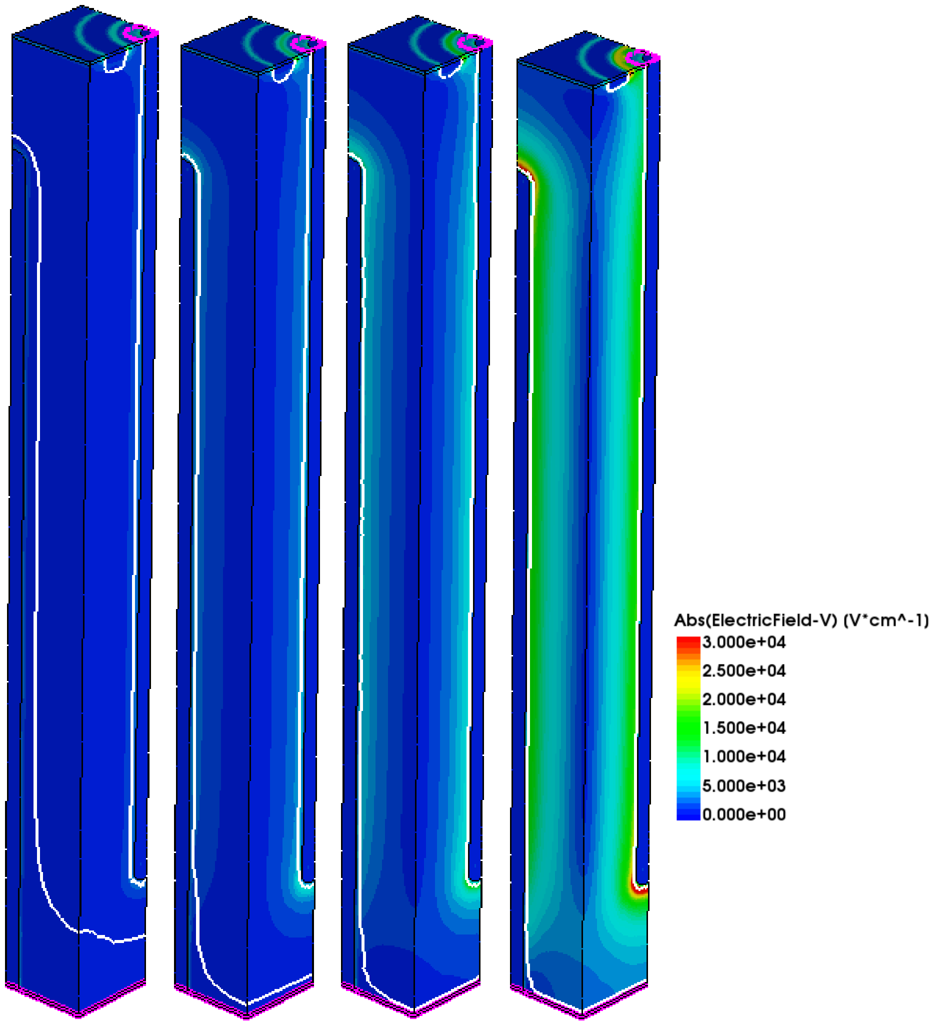

(A) (B) (C) (D) (E)

FIGURE 5.12: Electric field distributions for the orthogonal geometry, applying biases of 1V (A), 5V (B), 10V (C) and 60V (D).

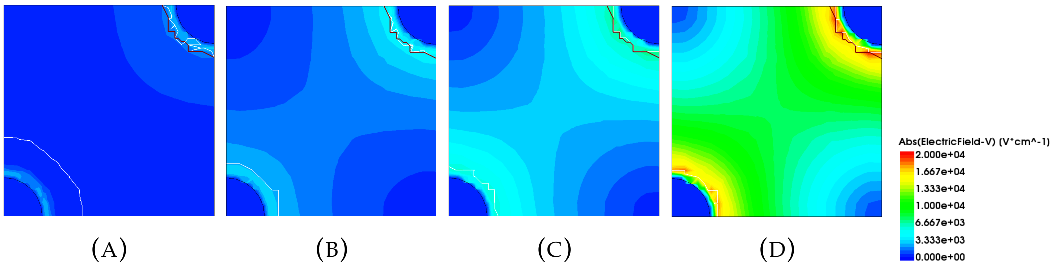

(A) (B) (C) (D)

FIGURE 5.13: Electric field distributions at a cross section of the orthogonal geometry structure, with applied biases of 1V (A), 5V (B), 10V (C), and 60V (D).

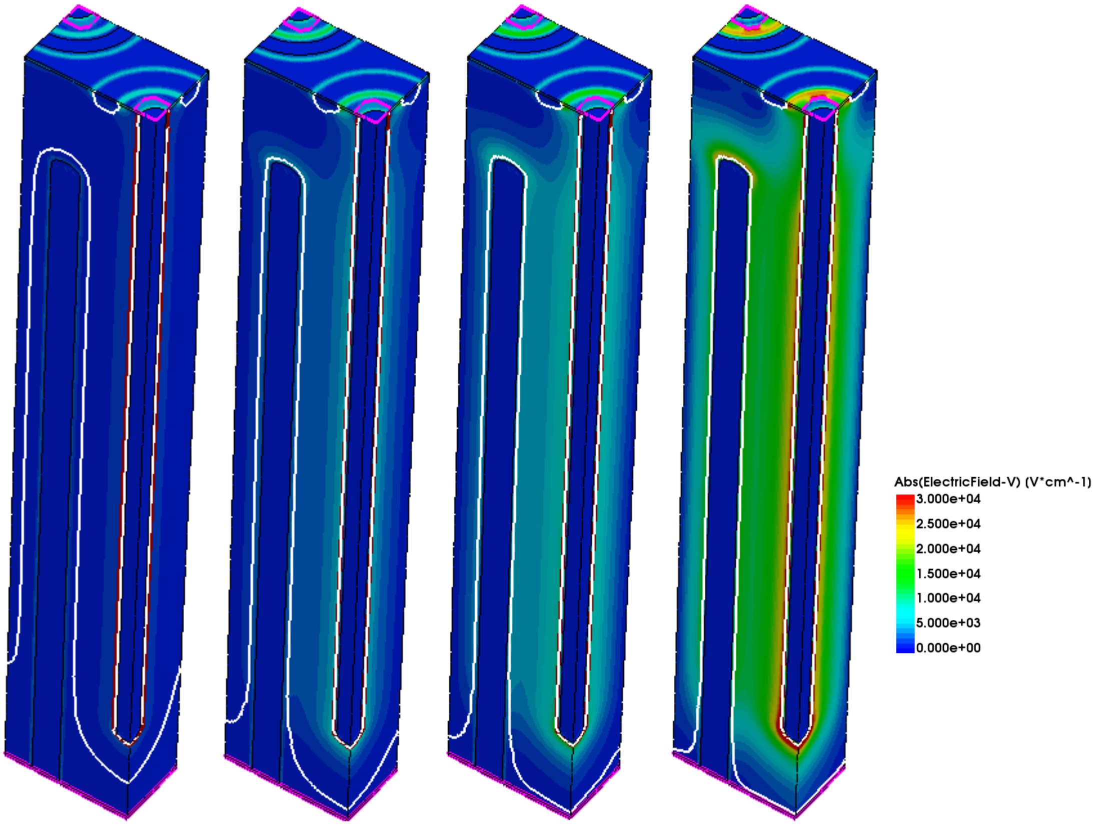
Abs(ElectricField-V) (V*cm^-1)
3.000e+04
2.500e+04
2.000e+04
1.500e+04
1.000e+04
5.000e+03
0.000e+00

(A) (B) (C) (D) (E)

FIGURE 5.14: Electric field distributions for the hexagonal geometry with p-n distance of 30 μm, applying biases of 1V (A), 5V (B), 10V (C) and 60V (D).

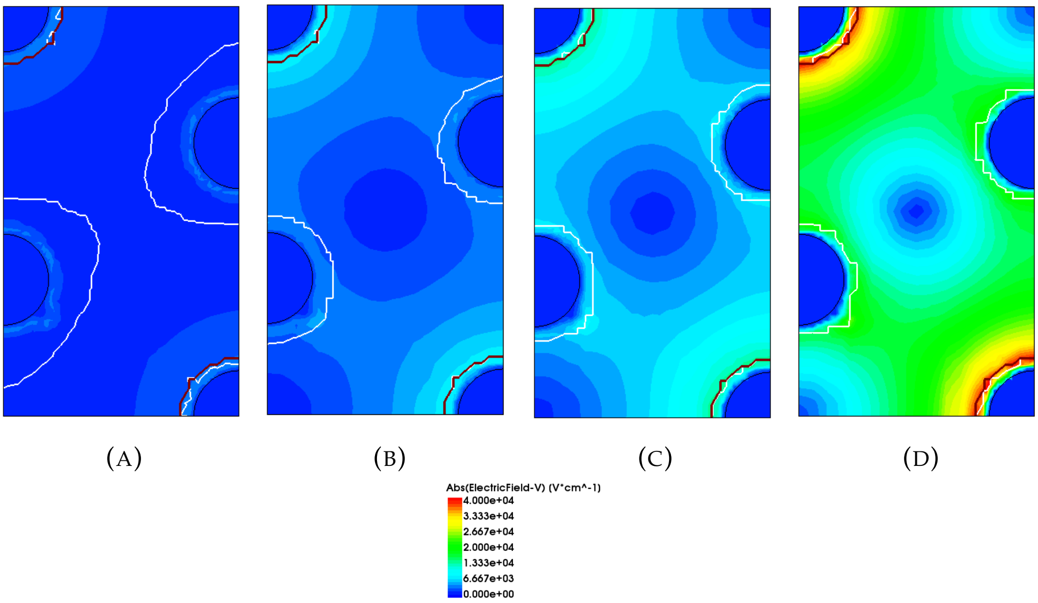

(A) (B) (C) (D)

FIGURE 5.15: Electric field distributions at a cross section of the hexagonal geometry structure with p-n distance of 30 μm, with applied biases of of 1V (a), 5V (b), 10V (c), and 60V (d).

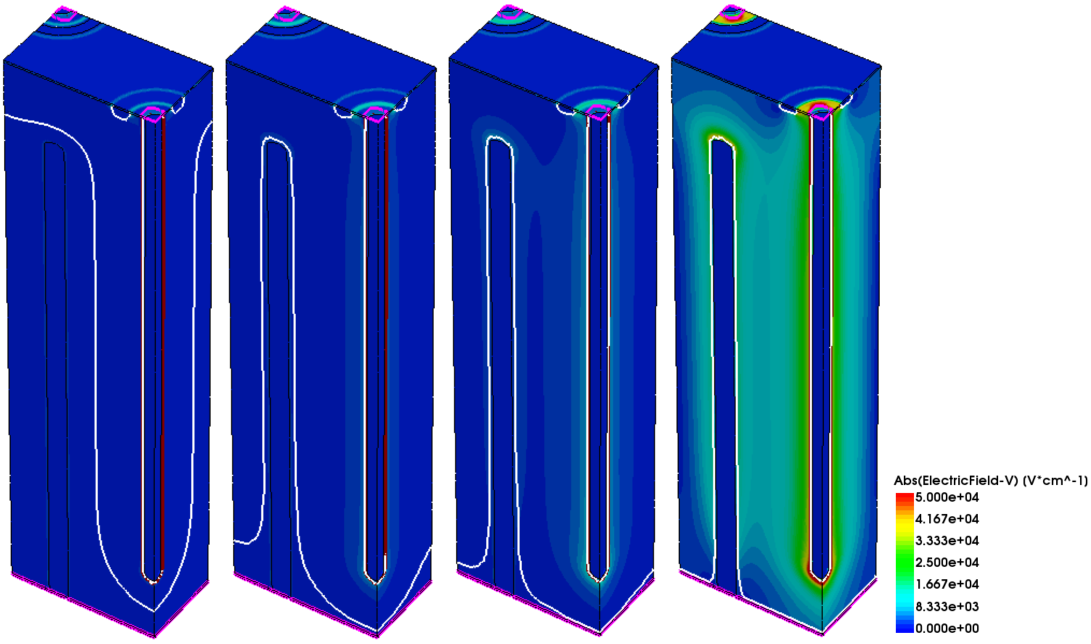

(A) (B) (C) (D) (E)

FIGURE 5.16: Electric field distributions for the hexagonal geometry with p-n distance of 50 μm, applying biases of 1V (A), 5V (B), 10V (C) and 60V (D).

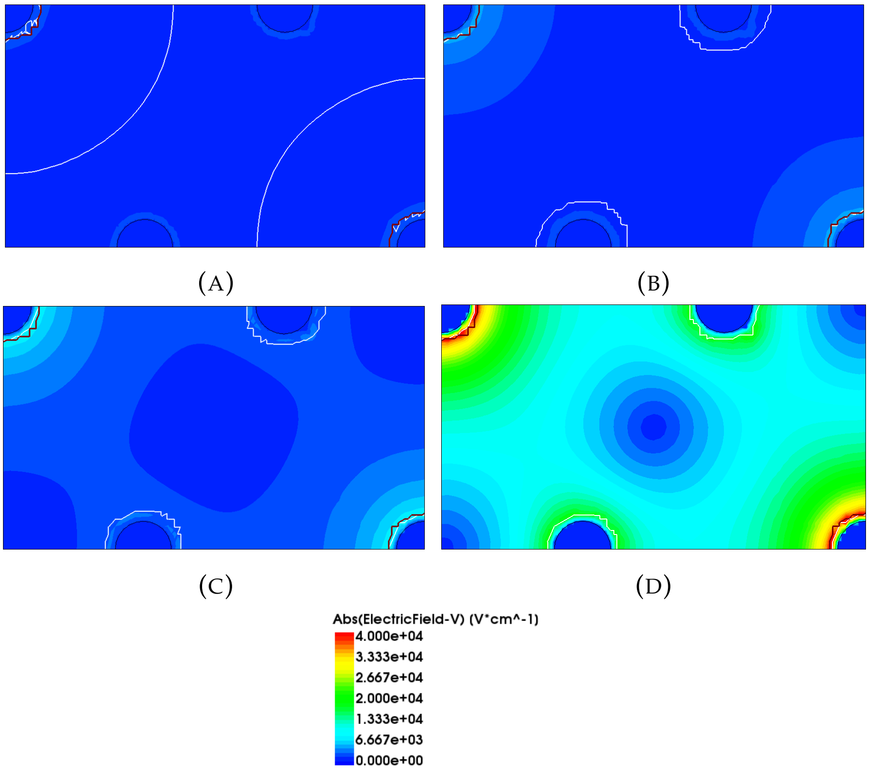

(A) (B) (C) (D)

FIGURE 5.17: Electric field distributions at a cross section of the hexagonal geometry structure with p-n distance of 50 μm, with applied biases of 1V (a), 5V (b), 10V (c), and 60V (d).

To give an idea of how they are to be interpreted, in the case there was a completely uniform electric field, all the points would be located at the same position in Y, distributed along the X axis, for it would mean that at all points in the cell would have the same value of the electric field, independently on the position. On the other hand, a non-uniform one would have the points scattered vertically at all distances.

When comparing the three configurations, they show a similar general behavior by having a first decrease of the electric field with little spread of electric field values, which correspond to the vicinity of the n-type electrode, which features a decaying electric field with distance which decays radially. Afterwards, there is a spread in values of the electric field which correspond to distances closer to the inter-electrode positions. The spread is attributed to the fact that at the distances at which there is the lower values of the electric field, at a close radius there is as well the p-type electrode, which features as well higher values of the electric field. Despite them showing a similar behavior, in the case of the hexagonal geometries the spread of the values of the electric field does not happen until approximately 15 μm for the 30 μm p-n distance and 25 μm for the 50 μm p-n distance, while for the orthogonal geometry already shows a spread of values at before 15 μm. Despite of that, a potential drawback for the hexagonal geometry would be that the region with the lowest absolute value of the electric field is found at the furthest distance, which could mean that there could be a major difference between the rise-times of particles hitting such positions and particles hitting positions closer to the n-type electrode. However, it is not clear how this would affect the overall time resolution and whether or not it would be dominant over the more uniform electric field that remains at the rest of the cell.

Another figure that can give information about the uniformity of the electric field is the mean value of the electric field at a given distance, with having as an error bar the spread of the values in said distance, calculated by means of the standard deviation. The figure is shown in Fig. 5.19. The side-by-side comparison show how in the three cases there is a smooth decrease of the electric field with distance, and a small increase in the end except for the case of the hexagonal with a p-n distance of 30 μm. The eventual increase is attributed to the higher electric field close to the p-type electrode. Moreover, the orthogonal geometry shows a rapid initial increase followed by a quick rise, whereas the hexagonal geometry results in a smoother electric field.

In addition to the uniformity of the electric field, another crucial factor influencing the time resolution is the intensity of the electric field itself. It

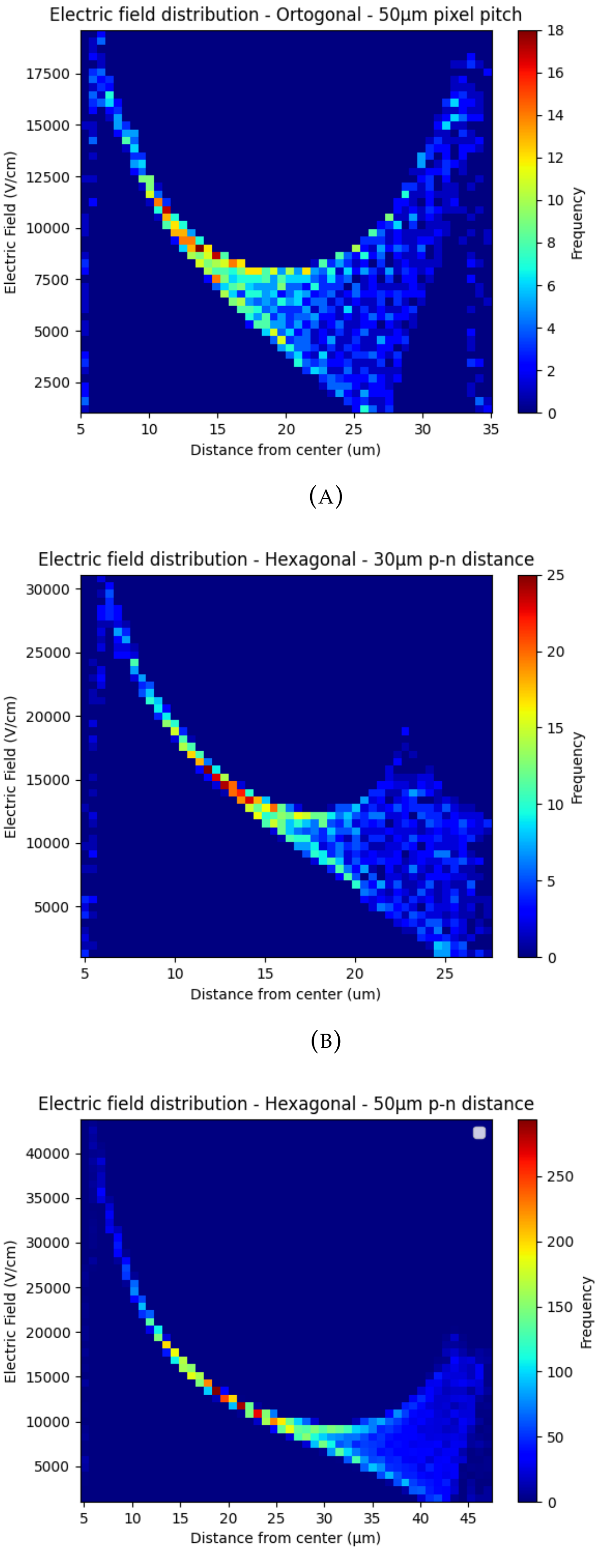

(A)

(B)

(C)

FIGURE 5.18: 2D Histograms of the frequency of the absolute values of the electric field depending on the distance from the n-type electrode located at the (0,0) position.

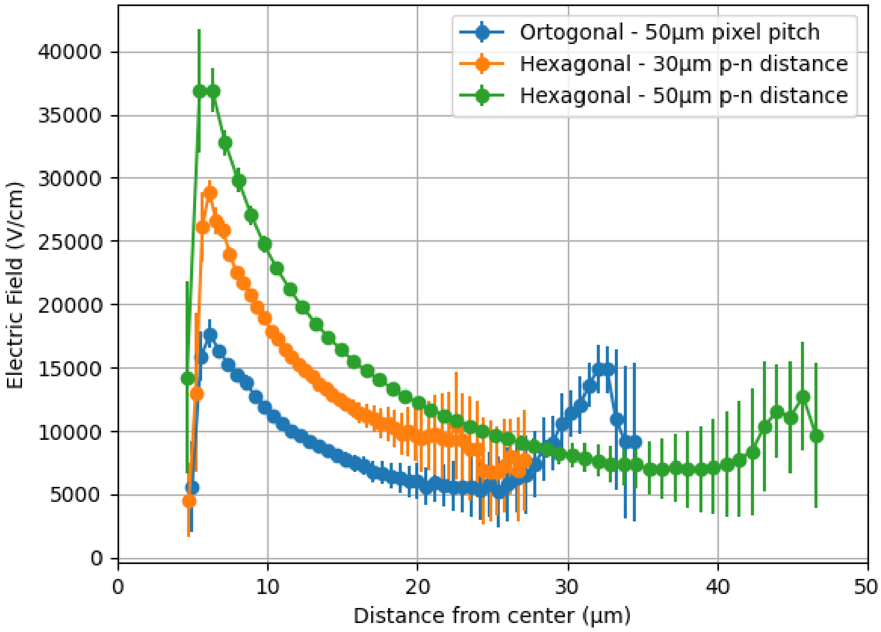

FIGURE 5.19: Mean value of the electric field depending on the distance. The error bars represent the spread of the values of the electric field within a given distance from the n-type electrode.

plays a significant role in minimizing the jitter contribution, where given a charge faster signals resulting from larger electric fields, produce larger signals when compared to slower ones. In Fig. 5.19, it is presented the curves corresponding to the three geometries showing which percentage of points within the cross sections feature absolute values higher than a certain threshold, given by the values at the X axis. From this plot can be extracted that with the same bias, the hexagonal geometries feature overall higher electric fields than with the orthogonal geometry, and while from Fig. 5.19 could be extracted that the hexagonal 30 μm p-n distance configuration had a smaller electric field than the one with p-n distance of 50 μm, it is concluded that the density of the electric field is higher in the former.

5.4 Conclusions and Discussion

In this chapter, 3D sensors with a hexagonal distribution have been discussed and compared to the orthogonal counterpart, with the design for timing applications for future colliders. Sensors have been designed and produced at CNM, building 3D sensors with 285 μm thick wafers featuring both hexagonal with p-n distances of 30 μm and 50 μm p-n distances, and orthogonal

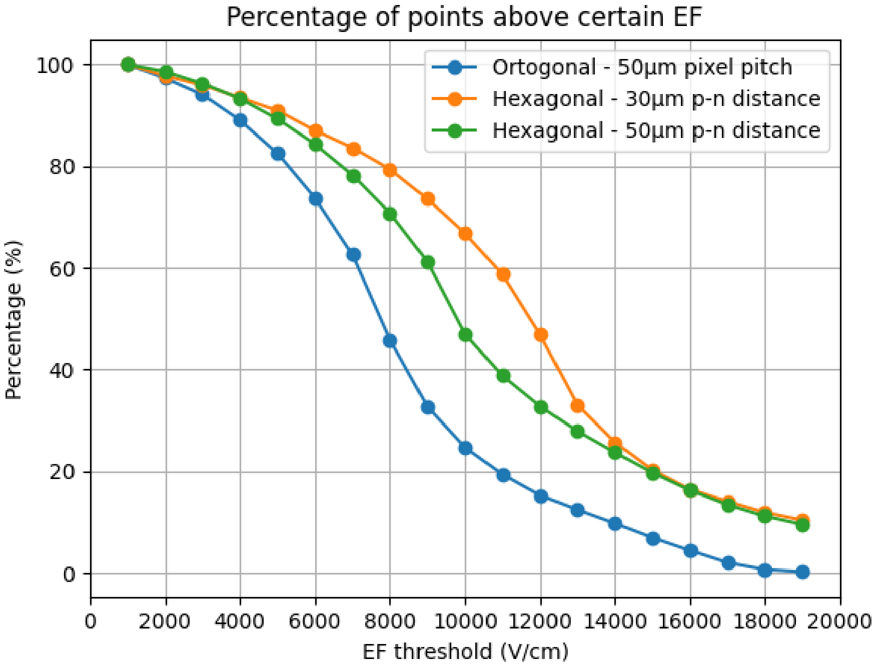

FIGURE 5.20: Mean value of the electric field.

distributions with a pixel pitch of 50 μm. The outcoming sensors have been characterized by means of I-V at room and low temperatures together with C-V measurements. The results showed that the same current was found for both temperature levels, meaning that there biggest contribution to the leakage current comes from the surface, and not from the bulk. Despite of that, C-V curves show a fast first depletion followed by a second depletion reached at close to $20V$, which is far below the breakdown voltage, meaning then that they can be operated fully depleted.

Afterwards, TCAD simulations of the 3D structures using the Synopsys Sentaurus software have been introduced. This involved the parameters used to create the structures, the resulting devices, and their electrical simulations. Despite featuring an artifact in one of the p-type columns the simulated structures are enough to represent the real structures. Then, the electrical simulations have been shown, displaying an $I - V$ curve with a breakdown at $60V$, as well as showing the $1/C$ vs V curves with a first fast depletion followed by a much slower depletion. Moreover, the $1/C$ vs V simulations have been compared with the previous measurements, showing that the curves fit when the arrays from the measurements are big, while the smaller arrays would not fit, which is found to be related to the large surface leakage current from the produced sensors. Additionally, the two-phase depletion has been confirmed by means of the electric field distribution simulations, which include the depletion region that shows how with less than $5V$ there is a full depletion at the direction between electrodes, while there is still non-depleted volume at the backside of the sensor. Despite of that, at the maximum voltage of $60V$ the backside is fully depleted.

Finally, a study of the uniformity and distribution of the electric field with a bias of $60V$ has been performed, in order to study which is the best candidate for timing measurements, whether if the hexagonal or the orthogonal geometry. 2D histograms of the distribution of the electric field depending on the distance from the center of the electrode have been shown, as well as a comparison among them of the mean value of the electric field depending on the the distance from the center of the electrode. When comparing the orthogonal and the hexagonal geometry, there is a wider spread with distance in the case of the orthogonal than with the hexagonal. Besides, the distribution that yields the larger values of electric field is the hexagonal, specially for the one with 50 μm. Furthermore, it has as well been shown, that the configuration that keeps the highest electric field along its cell is the hexagonal with 30 μm, meaning that there is a larger percentage of points within the same structure that features a large electric field.

All in all, while there seems to be some more uniformity in the hexagonal geometry which reduces the contribution of the electric field distortion to the time resolution, the factor that mostly makes the hexagonal configuration a candidate for better timing measurements is the larger electric field with even larger distance. As seen in chapter 3, one of the most limiting factors with 3D sensors for timing applications is the SNR, and with a given amount of charge, faster rise-time yield larger signals, it would imply a potential improvement over orthogonal geometries. Additionally, faster rise-times, would as well imply lower trapping probability, improving as well the radiation hardness.

As future work, an irradiation campaign should be performed on the produced sensors to prove its radiation hardness, as well as time resolution measurements with TCT and Sr90 source, to prove which configuration yield better charge collection efficiency and time resolution among them. Moreover, to further study the potential time resolution of the 3D sensors with orthogonal or hexagonal geometries, Montecarlo simulations should be performed in order to simulate multiple transients which can provide statistics to make the time resolution analysis.

Chapter 6

Conclusions and Future Work

In this thesis, 3D silicon radiation sensors have been investigated for radiation harsh enviornments. The work is motivated by the upcoming upgrade of the LHC, namely High-Luminosity LHC, and the Future Circular Collider (FCC) project. Both projects expect an increase in events per collision to unprecedented levels, requiring radiation sensors capable of performing reliably throughout the particle accelerators' lifetimes.

3D sensors fabricated at the clean room facilities in Centro Nacional de Microelectrónica (IMB-CNM-CSIC) on n-type $200\mu m$ thick silicon sensors have been electrically characterized before and after radiation exposure, with equivalent fluence levels of $1 \cdot 10^{14} n_{eq}/cm^2$, $1 \cdot 10^{15} n_{eq}/cm^2$, $5 \cdot 10^{15} n_{eq}/cm^2$, $1 \cdot 10^{16} n_{eq}/cm^2$, $5 \cdot 10^{16} n_{eq}/cm^2$ and $1 \cdot 10^{17} n_{eq}/cm^2$. The batch included a variety of devices, including sensors designed for specific ASICs, pad diodes with arrays of pixel pitches of $50\mu m\ x\ 50\mu m$, $25\mu m\ x\ 100\mu m$ in a variety of included number of pixels, and test structures with a single central electrode separately connected from the surrounding eight. Deficient metallization was found in multiple test structure devices, notably at fluence levels of $5 \cdot 10^{16} n_{eq}/cm^2$ and $1 \cdot 10^{17} n_{eq}/cm^2$. These were re-metallized through a series of Focused Ion Beam processes that restored the contact but left a halo of metal around the pad contacts. Electrical characterization, in the form of I-V and C-V curves, was performed on multiple of these sensors, before and after irradiation. The results are presented in Chapter 2. I-V curves showed that while the n-on-n architecture showed a higher leakage current due to the lower electrostatic potential barrier between the bulk and the n+ electrode, the current decreased after substrate type inversion due to non-ionizing effects. After substrate type inversions, leakage current increased with fluence, saturating after an equivalent fluence level of $1 \cdot 10^{15} n_{eq}/cm^2$. C-V curves showed full depletion with just a few volts before irradiation, and approximately $100V$ at $1 \cdot 10^{16} n_{eq}/cm^2$. C-V curves could not show full depletion for fluence levels of $5 \cdot 10^{16} n_{eq}/cm^2$ and $1 \cdot 10^{17} n_{eq}/cm^2$ due to capacitance distortion with high leakage currents.

In Chapter 3, the Transient Current Technique (TCT) was used to study time resolution and charge collection efficiency performance in response to an infrared laser. The laser intensity was calibrated using a reference PiN sensor. Waveforms were recorded exposing the reference sensor to a Sr^{90} source using the same electronics as the TCT, and were later analyzed by extracting the most probable value of the signal amplitude, which was then used to match the signal height induced by the laser. Setting an appropriate laser intensity is crucial because time resolution strongly depends on the Signal-To-Noise Ratio (SNR) of the signal, and an arbitrarily large laser intensity would yield biased results.

2D maps of charge collection were performed on pad diodes and test structures before and after irradiation, showing that charge collection had the same profile as the sensors. At a fluence level of $1 \cdot 10^{17} n_{eq}/cm^2$, the mean free path was lower than the inter-electrode distance due to lower collected charge at further distances from the n+ electrodes. Separately, 2000 waveforms were recorded at a position that minimized laser reflection by avoiding any metallization for arrays of 50 x50 pixels and test structures. Waveforms were then analyzed to obtain the time resolution and the charge collection. Results showed that large diode arrays yielded worse timing performance than the small test structures due to higher noise from the larger capacitance. Across all studies, time resolution was found to improve after substrate inversion, up to a fluence level of $1 \cdot 10^{15} n_{eq}/cm^2$, after which it had approximately the same or better time resolution as before irradiation. The improved time resolution after substrate inversion is mainly attributed to a higher SNR from larger signals induced by greater applied biases, together with lower leakage current. At a fluence level of $1 \cdot 10^{15} n_{eq}/cm^2$ an avalanche effect amplified the signal. However, at a fluence level of $5 \cdot 10^{16} n_{eq}/cm^2$ degraded considerably unless a much larger bias was applied, yielding a similar time resolution as before irradiation.

A study of time resolution with different laser intensities was also conducted using pad diodes. Results showed an improving performance with laser intensity, saturating with very large signals, indicating that other factors like weighting field distortion become more dominant. Notably, a time resolution of $700 ps$ was measured for a pad diode irradiated at a fluence level of $1 \cdot 10^{17} n_{eq}/cm^2$, with a laser calibrated to twice the intensity of a MIP. While this is an order of magnitude larger than the standards expected for the HL-LHC and the FCC (ranging $10 - 30 ps$), it must be considered the larger noise from the capacitance of a large array, so better timing performance is expected for smaller arrays. Moreover, it shows that 3D sensors can perform timing measurements even at extreme fluence for particles inducing larger signals even for large diode arrays. Lastly, a 2D map of the time resolution with a 3-MIP laser calibration was conducted, showing the strong dependence of time resolution on signal amplitude. The 2D map was performed by changing positions manually, which was too time-consuming to carry out for all fluence levels.

CCE and timing studies were performed for test structures, except for timing at $1 \cdot 10^{17} n_{eq}/cm^2$ due to insufficient signal amplitude. Results showed CCE of 100% for a fluence level of $1 \cdot 10^{14} n_{eq}/cm^2$, and more than 100% for higher fluence levels, attributed to the avalanche effect due to applied higher biases. Additionally, the bias required for a CCE of 100% increases with equivalent fluence level. However, while at a fluence level of $5 \cdot 10^{16} n_{eq}/cm^2$ a CCE of 200% was extracted at a bias of $300V$, at $1 \cdot 10^{17} n_{eq}/cm^2$ only 13% was collected at a bias of $360V$. This indicates that 3D sensors severely degrade at fluence levels beyond $5 \cdot 10^{16} n_{eq}/cm^2$. However, further measurements should be performed at extreme fluences for sensors that do not require undergoing a FIB process that leaves a metal halo around the contact, which would decrease the charge collected due to laser reflection.

In Chapter 4, the commissioning of a strontium-90 source setup at the Radiation Detectors laboratory in CNM was conducted. The commissioning involved finding a time resolution of $32.34ps$ at a bias of $363V$ for two LGAD sensors at a temperature of $-32°C$. One of these sensors was later used as reference for timing measurements performed for test structures irradiated at fluence levels of $1 \cdot 10^{15} n_{eq}/cm^2$, $1 \cdot 10^{16} n_{eq}/cm^2$ and a non-irradiated one. Results showed a time resolution of $68ps$ at a voltage of $50V$ before irradiation, $27.77ps$ at $100V$ for $1 \cdot 10^{15} n_{eq}/cm^2$ and $82.51ps$ at $225V$ for $1 \cdot 10^{16} n_{eq}/cm^2$. Therefore, consistent with TCT measurements, time resolution improves after irradiation and decreases at higher radiation doses. Additionally, in both setups, the best time resolution is found around $1 \cdot 10^{15} n_{eq}/cm^2$. Charge collection studies showed better charge collection at $1 \cdot 10^{16} n_{eq}/cm^2$. However, lower charge collection was found for $1 \cdot 10^{15} n_{eq}/cm^2$, attributed to signal reflection that reduced the tail of the signal, resulting in a narrower integration window that decreases the integrated charge. Despite this, the amplitude was significantly higher, indicating charge multiplication as observed with the TCT setup. The signal reflection is most likely due to an impedance mismatch of the board, as it was not observed in other measurements. Hence, for future work, measurements should be carried out using a fully functional PCB, and ensuring that signals have the expected shape. Moreover, for future work, Sr^{90} source measurements should be performed for higher fluence levels, especially at $1 \cdot 10^{17} n_{eq}/cm^2$. Additionally, a low event rate was found for the setup, indicating a misalignment between the DUT and the reference sensor. Therefore, a mobile support would be convenient for more efficient data taking, a limiting factor when taking large amounts of data.

TCT and Sr^{90} source setups showed to yield comparable results, indicating that while TCT neglects the Landau distribution of energy deposition, the 3D sensors' characteristics allow for reliable results that can be used to study sensor performance. Despite this, future work requires optimization of both setups. For the TCT setup:

- Automatization of time resolution 2D map to better study the time resolution dependence on the position in the pixel, a phenomenon especially interesting for 3D sensors.
- Monitoring of laser intensity to properly control the induced signal and avoid arbitrarily large or small signals that bias timing results.
- Better temperature control. In some cases, reaching the desired temperature was difficult, even sometimes not reaching $-20°C$.

For the Sr^{90} source setup:

- Controlled movement of the DUTs to improve alignment between sensors, required for better event rate.
- More correctly functioning PCB, to avoid signal distortion and to be able to wire-bond more fluence levels simultaneously, which helps to measure more sensors in the same timescale.

In Chapter 5, 3D sensors designed for timing measurements are studied. The design involves thicker active thickness for larger induced signals, and the addition of a hexagonal geometry that better optimizes space distribution, thus further reducing travelling distances for drifting carriers. A batch of sensors was produced at the CNM clean room facilities and later characterized with I-V and C-V curves. Measurements showed that while a high surface leakage current was found, compliance was not reached before full depletion, thus making the sensors completely operational. Moreover, simulations were carried out to better understand the differences in terms of electric field and depletion between the classic orthogonal geometry and hexagonal distributions with p-n distances of $30\mu m$ and $50\mu m$. Simulations showed a breakdown occurring at $60V$, and a lateral full depletion reached with less than $5V$. However, a bias between $10V$ and $60V$ is required to deplete the bottom of the p+ electrode. A study on uniformity of the electric field was carried out, showing a slightly more uniform electric field for the hexagonal geometry. More notably, while featuring similar pixel sizes, the hexagonal geometry maintains higher absolute values of the electric field across the sensor compared to the orthogonal, yielding faster signals necessary for better timing performances.

For further study, an irradiation campaign should be conducted for the fabricated 3D sensors designed for timing applications. Afterwards, TCT and strontium-90 source measurements should be performed to further prove the difference in timing and CCE between both geometries.

Appendix A

Simulation Models

In this appendix, further information about the physical models used for the TCAD simulations is provided.

A.1 Mobility models

To accurately simulate the behaviour of a device, it is crucial to consider factors that affect carrier behaviour. TCAD Synopsis Sentaurus features mobility models that can be employed for various conditions. When multiple mobility models are used, the total mobility is calculated using Mathiessen's rule:

$$\frac{1}{\mu} = \frac{1}{\mu_1} + \frac{1}{\mu_2} + \cdots \tag{A.1}$$

Where μ is the total mobility and $\mu_1, \mu 2 \cdots$ represent the different contributions to mobility from bulk, surface or thin layers. The models used are the doping dependence model, the Lombardi, high field saturation and carrier-carrier scattering.

A.1.1 Doping dependence

Impurities in semiconductors act as scattering points in the lattice, reducing the mobility of the carriers as a result. To account for this effect, the Masetti model [43] can be used:

$$\begin{aligned} \mu_{dop} =& \mu_{min1} exp\left(-\frac{P_c}{N_{A,0}+N_{D,0}}\right) \\ &+ \frac{\mu_{const}-\mu_{min_2}}{1+\left(\left(N_{A,0}+N_{D,0}\right)/C_r\right)^{\alpha}} - \frac{\mu_1}{1+\left(C_s/\left(N_{A,0}+N_{D,0}\right)\right)^{\beta}} \end{aligned} \tag{A.2}$$

Coefficient	Electrons	Holes	Unit
μ_{min1}	52.2	44.9	cm^2/Vs
μ_{min2}	52.2	0	cm^2/Vs
μ_1	43.4	29.0	cm^2/Vs
P_c	0	$9.23 \cdot 10^{16}$	cm^3
C_r	$9.68 \cdot 10^{16}$	$2.23 \cdot 10^{17}$	cm^3
C_s	$3.43 \cdot 10^{20}$	$6.10 \cdot 10^{20}$	cm^3
α	0.680	0.719	1
β	2.0	2.0	1

TABLE A.1: Coefficients used for the Masetti model.

Where μ_{min1}, μ_{min2} and μ_1 are reference mobilities, P_c, C_r and C_s represent reference doping concentrations, and α and β are coefficients. μ_{const} is the low-doping reference mobility, determined by the constant mobility model:

$$\mu_{const} = \mu_L \left(\frac{T}{300K}\right)^{\zeta} \tag{A.3}$$

Where μ_L is the mobility due to the bulk phonon scattering, T is the temperature, and ζ is 2.5 for electrons and 2.2 for hole. Therefore, the constant mobility decays with temperature according to a saturation velocity of 1417 cm^2/Vs for electrons and 470.5 cm^2/Vs for holes. The rest of the coefficients are listed at table A.1.

A.1.2 Lombardi Model

In semiconductor interfaces, high transverse electric fields are common, which force carriers to interact with acoustic surface phonons and surface roughness. The mobility contribution due to surface roughness is given by:

$$\mu_{sr} = \left(\frac{\left(E_T/E_{ref}\right)^A}{\delta} + \frac{E_T^3}{\eta}\right)^{-1} \tag{A.4}$$

Where E_T is the transverse electric field, E_{ref} is a factor that ensure a unitless numerator and equals one, and A, δ, η are parameters. The contribution from acoustic phonons is given by:

$$\mu_{ac} = \frac{B}{E_T} + \frac{C\left(\frac{N_{A,0}+N_{D,0}+N_2}{N_0}\right)^{\lambda}}{E_T^{1/3}\frac{T}{300K}} \tag{A.5}$$

Coefficient	Electrons	Holes	Unit
B	$4.57 \cdot 10^7$	$9.925 \cdot 10^6$	$cms^{-}1$
C	$5.80 \cdot 10^2$	$2.947 \cdot 10^3$	$V^{2/3}s$
$N_0 = N_2$	1	1	cm^{-3}
λ	0.1250	0.00317	1
δ	$5.85 \cdot 10^{14}$	$2.0546 \cdot 10^{1}4$	cm^2/Vs
k	1	1	1
A	2	2	1
η	$5.85 \cdot 10^{3}0$	$2.546 \cdot 10^{3}0$	V^2/cms

TABLE A.2: Coefficients used for the Lombardi model.

where B and C are parameters, $N_{A,0}$, $N_{D,0}$ represent the concentration of acceptors or donors, respectively, N_0 is a factor that ensure a unitless numerator and equals one, T is the temperature, and B, C, and λ are parameters.

These contributions are included in Matthiessen's rule (Eq. A.1) with a coefficient that decreases the contribution with further distances from the surface:

$$\frac{1}{\mu} = \frac{1}{\mu_b} + \frac{D}{\mu_{sr}} + \frac{D}{\mu_{ac}} \tag{A.6}$$

where μ_b represents the bulk contribution to mobility, a $D = \exp -xl_{crit}$ with x being the distance from the interface and l_{crit} a fit parameter. The values of the various parameters in the Lombardi model are listed in Table A.2.

A.1.3 High Field Saturation

For a high enough electric field, the velocity of carriers is no longer proportional to the electric field, but instead saturates to a certain value $v_s at$. This behaviour can be explained by the Canali model, which describes mobility in function of the temperature, fitted up to 430K [44]:

$$\mu(F) = \frac{\mu_{low}}{\left[1 + \left(\frac{\mu_{low}F}{v_{sat}}\right)^{\beta}\right]^{\beta^{-1}}} \tag{A.7}$$

Where μ_{low} is the low-field mobility, v_{sat} is the saturation velocity and β is a temperature dependent parameter. β and v_{sat} are given by:

$$\beta = \beta_0 \left(\frac{T}{300K}\right)^{\beta_{exp}} \tag{A.8}$$

Coefficient	Electrons	Holes	Unit
$v_{sat,0}$	$1.07 \cdot 10^7$	$8.37 \cdot 10^6$	$cms^{-}1$
$v_{sat,exp}$	0.87	0.52	1
β_0	1.109	1.213	1
β_{exp}	0.66	0.17	1

TABLE A.3: Coefficients used for the Canali model.

$$v_{sat} = v_{sat,0} \left(\frac{T_0}{T} \right)^{v_{sat,exp}} \tag{A.9}$$

The values of the parameters are listed in Table A.3

A.1.4 Carrier-Carrier Scattering

Mobility can also degrade with carrier-carrier scattering, which is described by the Conwell-Weisskopf model. Its contribution to the total mobility given by the Mathiessen's law is expressed by:

$$v_{eh} = \frac{D \left(\frac{T}{300K} \right)^{3/2}}{\sqrt{np}} \left[ln \left(1 + F \left(\frac{T}{300K} \right)^2 (pn)^{-1/3} \right) \right]^{-1} \tag{A.10}$$

Where $D = 1.04 \cdot 10^{21} cm^{-1} V^{-1} s^{-1}$ and $F = 7.452 \cdot 10^{13} cm^{-2}$. T is the temperature of the system, and n and p the electron and holes density, respectively.

A.2 Generation-recombination models

A.2.1 Schockley-Reah-Hall Recombiantion

This model reproduces recombination through deep defect levels in the band gap. In Synopsis Sentaurus it is implemented in the following form:

$$R_{net}^{SRH} = \frac{np - n_{i,eff}^2}{\tau_p (n + n_1) + \tau_n (p + p_1)} \tag{A.11}$$

With:

$$n_1 = n_{i,eff} exp \left(\frac{E_{trap}}{kT} \right) \tag{A.12}$$

$$p_1 = n_{i,eff} exp \left(\frac{E_{trap}}{kT} \right) \tag{A.13}$$

Where E_{trap} is the difference between the defect level and the intrinsic level. τ_p and τ_n are the electron and holes lifetimes, which are modelled as a product of a doping-dependent, field-dependent and temperature-dependent factors:

$$\tau_{n,p} = \tau_{dop} \frac{f(T)}{1 + g_{n,p}(F)} \tag{A.14}$$

Where $[1 + g_{n,p}(F)]^{-1}$ is the electric field factor, taken into account when calculating the carrier lifetime due to recombination. For electric fields larger than $3 \cdot 10^5 V/cm$ this factor cannot be neglected, due to reversely biased p-n junctions being more sensitive to defect-assisted tunnelling, yielding an e-h pair generation even before band-to-band tunneling or avalanche mechanisms. For this, the Schenk Trap-Assisted Tunneling Model has been used, which for the case of the electrons has the form [76]:

$$\begin{aligned} g_n(F) = {} & \left(1 + \frac{(\hbar\Theta)^{3/2}\sqrt{E_t - E_0}}{E_0 \hbar\omega_0}\right)^{-1/2} \frac{(\hbar\Theta)^{3/4}(E_t - E_0)^{1/4}}{2\sqrt{E_t E_0}} \left(\frac{\hbar\Theta}{kT}\right)^{\frac{3}{2}} \\ & \times \exp\left(-\frac{E_t - E_0}{\hbar\omega_0} + \frac{\hbar\omega_0 - kT}{2\hbar\omega_0} + \frac{2E_t + kT}{2\hbar\omega_0} \ln\frac{E_t}{\varepsilon_R} \right. \\ & \left. - \frac{E_0}{\hbar\omega_0} \ln\frac{E_0}{\varepsilon_E} + \frac{E_t - E_0}{kT} - \frac{4}{3}\left(\frac{E_t - E_0}{\hbar\Theta}\right)^{\frac{3}{2}}\right) \end{aligned} \tag{A.15}$$

Where E_0 is the energy of an optimum horizontal transition path, which is given by:

$$E_0 = \frac{(2\varepsilon_R kT)^2)}{(\hbar\Theta)} \tag{A.16}$$

With $\varepsilon_R = Sh\omega_0$ being the relaxation energy, S is the Huang-Rhys factor, $\hbar\omega_0$ the phonon energy, E_t the energy level of the recombination center, and $\Theta = (q^2F^2/2\hbar m_{\Theta,n})$ is the electro-optical frequency. The mass $m_{\Theta,n}$ is the electron tunnelling mass in the direction of the field. The expression for holes goes as Eq. A.15, but with $m_{\Theta,p}$ instead of $m_{\Theta,n}$ and $E_{g,eff} - Et$ instead of just E_t.

A.2.2 Auger Recombination

In the Auger recombination process, an electron is relaxed from the conduction band to the valence band, transferring the energy to another electron

Coefficient	Electrons	Holes	Unit
A_A	$6.7 \cdot 10^{-32}$	$7.2 \cdot 10^{-32}$	cm^6s^{-1}
B_A	$2.45 \cdot 10^{-31}$	$4.5 \cdot 10^{-33}$	cm^6s^{-1}
C_A	$-2.2 \cdot 10^{-32}$	$2.63 \cdot 10^{-32}$	cm^6s^{-1}
H	3.46667	8.25688	1
N_0	$1.0 \cdot 10^{18}$	$1 \cdot 10^{18}$	cm^3

TABLE A.4: Coefficients used for the auger recombination effect model.

that relaxes through the release of phonons. This effect is especially non-negligible in at high carrier density regions. The rate of recombination due to band-to-band Auger effect is given by:

$$E_0net^A = (C_n n + C_p p)\left(np - n_{i,eff}^2\right) \tag{A.17}$$

With C_n and C_p being the temperature dependent coefficients:

$$C_n(T) = \left(A_{A,n} + B_{A,n}\left(\frac{T}{300K}\right)C_{A,n}\left(\frac{T}{300K}\right)^2\right)\left[1 + H_n \exp\left(-\frac{n}{N_{0,n}}\right)\right] \tag{A.18}$$

$$C_p(T) = \left(A_{A,p} + B_{A,p}\left(\frac{T}{300K}\right)C_{A,p}\left(\frac{T}{300K}\right)^2\right)\left[1 + H_p \exp\left(-\frac{n}{N_{0,p}}\right)\right] \tag{A.19}$$

The term $[1 + H_p \exp(-p/N_{0,p})]$ is used to take into consideration the decrease of the Auger coefficients at high injection levels, which is due to excitons decaying at high carrier densities, resulting in a decrease of recombination [77]. The values of the Auger coefficients are listed in table A.4.

A.2.3 Avalanche - Impact Ionization

When the space charge region width is lower than the mean free path between two ionizing events, an avalanche mechanism can take place, causing an electrical breakdown process. In this case, the generation for electrons and holes are treated separately, with a total generation rate that can be expressed as:

$$G_{ii} = \frac{1}{q}\left(\alpha_n\left|\overrightarrow{J_n}\right| + \alpha_n\left|\overrightarrow{J_p}\right|\right) \tag{A.20}$$

Coefficient	Electrons	Holes	Valid range of electric field	Unit
$a\,(low)$	$7.03 \cdot 10^5$	$8.37 \cdot 10^6$	$1.75 \cdot 10^5\ V/cm\ to\ E_0$	cm^{-1}
$a\,(high)$	$7.03 \cdot 10^5$	$7.03 \cdot 10^5$	$E_0 to 6 \cdot 10^5\ V/cm$	cm^{-1}
$b\,(low)$	$1.231 \cdot 10^6$	$7.03 \cdot 10^5$	$1.75 \cdot 10^5\ V/cm\ to\ E_0$	V/cm
$b\,(high)$	$1.231 \cdot 10^6$	$7.03 \cdot 10^5$	$E_0 to 6 \cdot 10^5\ V/cm$	V/cm
E_0	$4 \cdot 10^5$	$4 \cdot 10^5$	-	V/cm
$\hbar\omega_{op}$	0.063	0.063	-	E_v
λ	$62 \cdot 10^{-8}$	$62 \cdot 10^{-8}$	-	cm
$\beta\,(low)$	0.678925	0.815009	$1.75 \cdot 10^5\ V/cm\ to\ E_0$	1
$\beta\,(high)$	0.678925	0.677706	$E_0 to 6 \cdot 10^5\ V/cm$	1

TABLE A.5: Coefficients from the van Overstraeten-de Man model for impact ionization.

Where $\overrightarrow{J_n}$ and $\overrightarrow{J_p}$ are the electron and hole current density vectors, and α_i is the ionization coefficient of the carrier i, which is the reciprocal of the mean free path. The Overstraeten-de Man model, based on Chynoweth law, provides the used coefficients:

$$\alpha\left(F_{ava}\right) = \gamma a \exp\left(-\frac{\gamma b}{F_{ava}}\right) \tag{A.21}$$

With:

$$\gamma = \frac{\tanh\left(\frac{\hbar\omega_{op}}{2kT_0}\right)}{\tanh\left(\frac{\hbar\omega_{op}}{2kT}\right)} \tag{A.22}$$

The factor γ expresses the temperature dependence of the phonon gas against which carriers are accelerated. The values of a, b and $\hbar\omega_{op}$ apply to fields in the range from $1.75 \cdot 10^5 Vcm^{-1}$ to $6 \cdot 10^5 Vcm^{-1}$, and vary depending on the case of high or low electric field. Its values are listed in table A.5.

A.3 Effective Intrinsic Density

In a regions with a high enough doping concentration, the narrowing of the bandgap becomes non-negligible. The model for the lattice temperature-dependancy of the bandgap is [46]:

$$E_g(T) = E_g(0) - \frac{\alpha T^2}{T + \beta} \tag{A.23}$$

Where $E_g(0)$ is the bandgap energy at $0K$, $\alpha = 4.76 \cdot 10^{-4} eV/K$ and $\beta = 636K$. So, the effective bandgap can be expressed by the contributions of the default bandgap according to the temperature $E_g(T)$, and contribution from the narrowing using a model of choice:

$$E_{g,erff}(T) = E_g(T) + \delta E_{bg} \tag{A.24}$$

The one used is the Old Slotboom model, which is expressed as:

$$\delta E_{bg} = E_{ref} \left[\ln\left(\frac{N_{tot}}{N_{ref}}\right) + \sqrt{\left(\ln\left(\frac{N_{tot}}{N_{ref}}\right)\right)^2 + 0.5} \right] \tag{A.25}$$

Where $E_{ref} = 9.03 \cdot 10^{-3} eV$ and $N_{ref} = 1.017 cm^{-3}$.

Bibliography

[1] R. Oerter, *The Theory of Almost Everything: The Standard Model, the Unsung Triumph of Modern Physics*. Penguin Publishing Group, 2006, ISBN: 9780452287860. [Online]. Available: `https://books.google.es/books?id=fkjmjwEACAAJ`.

[2] A. Collaboration, "Observation of a new particle in the search for the standard model higgs boson with the atlas detector at the lhc," *Physics Letters B*, vol. 716, no. 1, pp. 1–29, 2012, ISSN: 0370-2693. DOI: `https://doi.org/10.1016/j.physletb.2012.08.020`. [Online]. Available: `https://www.sciencedirect.com/science/article/pii/S037026931200857X`.

[3] C. Collaboration, "Observation of a new boson at a mass of 125 gev with the cms experiment at the lhc," *Physics Letters B*, vol. 716, no. 1, pp. 30–61, 2012, ISSN: 0370-2693. DOI: `https://doi.org/10.1016/j.physletb.2012.08.021`. [Online]. Available: `https://www.sciencedirect.com/science/article/pii/S0370269312008581`.

[4] "The large hadron collider." (), [Online]. Available: `https://home.cern/science/accelerators/large-hadron-collider`.

[5] "Experiments at cern." (), [Online]. Available: `https://home.cern/science/experiments`.

[6] A. Collaboration, "Technical Design Report for the ATLAS Inner Tracker Pixel Detector," CERN, Geneva, Tech. Rep., 2017. [Online]. Available: `http://cds.cern.ch/record/`.

[7] S. T. et al, "Novel 3d pixel sensors for the upgrade of the atlas inner tracker," vol. 9, 2021. DOI: `https://doi.org/10.3389/fphy.2021.624668`.

[8] C. CERN Education and O. Group, "Lhc - the guide faq.," Brochure 002, February, 2017. [Online]. Available: `https://cds.cern.ch/record/2809109/files/CERN-Brochure-2021-004-Eng.pdf`.

[9] "2022: Higgs10, lhc run 3 and restart." (2022), [Online]. Available: `https://home.cern/press/2022`.

[10] G.Arduini, “High-luminosity large hadron collider (hl-lhc): Technical design report,” CERN, Tech. Rep., 2020. DOI: `https://doi.org/10.23731/CYRM-2020-0010`.

[11] W. Herr and B. D. Muratori, “Concept of luminosity,” 2006. [Online]. Available: `https://api.semanticscholar.org/CorpusID:34280714`.

[12] O. Brüning, “The high-luminosity large hadron collider,” vol. 1, pp. 241–243, 2019. DOI: `https://doi.org/10.1038/s42254-019-0050-6`.

[13] CERN. (), [Online]. Available: `https://fcc.web.cern.ch/photos`.

[14] “Future circular collider, Conceptual design report.” (), [Online]. Available: `https://fcc-cdr.web.cern.ch/#`.

[15] F. Zimmerman, “Fcc feasibility study status,” 110th Plenary ECFA Meeting, 2022. [Online]. Available: `https://indico.cern.ch/event/1172215/`.

[16] K. K. N. S.M. Sze, *Physics of Semiconductor Devices*, 3rd. John Wiley Sons, 2007, ISBN: 978-0-471-14323-5.

[17] G. Lurtz, *Semiconductor Radiation Detectors*. Springer, 1999, ISBN: 978-3-540-71678-5.

[18] G. F. Knoll, *Radiation Detection and Measurement*. John Wiley Sons, 2000, ISBN: 9780470131480.

[19] F. Hartman, *Evolution of silicon sensor technology in particle physics* (Springer Tracts in Modern Physics). Springer, 2009, vol. 275, ISBN: 978-3-319-64434-9.

[20] A. Chilingarov, “Iv and cv measurements in si diodes,” Technical Note, 2014. [Online]. Available: `https://rd50.web.cern.ch/`.

[21] C. Honsberg and S. Bowden. “Absorption coefficient.” (2019), [Online]. Available: `www.pveducation.org`.

[22] M.K.Sahu and G.Palai, “Theoretical investigation of doping concentration in silicon semiconductor using optical principle,” *International Journal of Optics and Photonics (IJOP)*, vol. 9, no. 2, pp. 99–98, 2015.

[23] S. Ramo, “Currents induced by electron motion,” *Proceedings of the IRE*, vol. 27, no. 9, pp. 584–585, 1939. DOI: `10.1109/JRPROC.1939.228757`.

[24] D. Pitzl, N. Cartiglia, B. Hubbard, *et al.*, "Type inversion in silicon detectors," *Nuclear Instruments and Methods in Physics Research Section A: Accelerators, Spectrometers, Detectors and Associated Equipment*, vol. 311, no. 1, pp. 98–104, 1992, ISSN: 0168-9002. DOI: https://doi.org/10.1016/0168-9002(92)90854-W. [Online]. Available: https://www.sciencedirect.com/science/article/pii/016890029290854W.

[25] R. Wunstorf, W. Bugg, J. Walter, F. Garber, and D. Larson, "Investigations of donor and acceptor removal and long term annealing in silicon with different boron/phosphorus ratios," *Nuclear Instruments and Methods in Physics Research Section A: Accelerators, Spectrometers, Detectors and Associated Equipment*, vol. 377, no. 2, pp. 228–233, 1996, Proceedings of the Seventh European Symposium on Semiconductor, ISSN: 0168-9002. DOI: https://doi.org/10.1016/0168-9002(96)00217-3. [Online]. Available: https://www.sciencedirect.com/science/article/pii/0168900296002173.

[26] M. Moll, "Radiation damage in silicon particle detectors," Ph.D. dissertation, University of Hamburg, 1999. [Online]. Available: https://mmoll.web.cern.ch/thesis/.

[27] G. K. et al, "Charge collection studies on custom silicon detectors irradiated up to 1.6·1017 neq/cm2," *Journal of Instrumentation*, vol. 8, P08004, 2013. DOI: 10.1088/1748-0221/8/08/P08004.

[28] G. Kramberger, V. Cindro, I. Mandić, M. Mikuž, and M. Zavrtanik, "Determination of effective trapping times for electrons and holes in irradiated silicon," *Nuclear Instruments and Methods in Physics Research Section A: Accelerators, Spectrometers, Detectors and Associated Equipment*, vol. 476, no. 3, pp. 645–651, 2002, Proc. of the 3rd Int. Conf. on Radiation Effects on Semiconductor Materials, Detectors and Devices, ISSN: 0168-9002. DOI: https://doi.org/10.1016/S0168-9002(01)01653-9. [Online]. Available: https://www.sciencedirect.com/science/article/pii/S0168900201016539.

[29] V. C. et al, "Readout of non-irradiated and irradiated strip detectors with fast analogue electronics," *Nuclear Instruments and Methods in Physics Research Section A: Accelerators, Spectrometers, Detectors and Associated Equipment*, vol. 439, no. 2, pp. 337–343, 2000, ISSN: 0168-9002. DOI: https://doi.org/10.1016/S0168-9002(99)00871-2. [Online]. Available: https://www.sciencedirect.com/science/article/pii/S0168900299008712.

[30] M. H. S. Seidel J. Metcalfe, "Depletion voltage abnd effective doping concentration of float zone and magnetic czochralski silicon diodes irradiated by protons to conditions relevant to the high luminosity lhc," CERN, 19th RD50 Workshop, 2011.

[31] L. W.-F. et al, "Annealing studies of irradiated p-type sensors designed for the upgrade of atlas phase-ii strip tracker," *Nuclear Instruments and Methods in Physics Research Section A: Accelerators, Spectrometers, Detectors and Associated Equipment*, vol. 924, pp. 128–132, 2019, 11th International Hiroshima Symposium on Development and Application of Semiconductor Tracking Detectors, ISSN: 0168-9002. DOI: `https://doi.org/10.1016/j.nima.2018.10.014`. [Online]. Available: `https://www.sciencedirect.com/science/article/pii/S0168900218313299`.

[32] S. Seidel, "Silicon strip and pixel detectors for particle physics experiments," *Physics Reports*, vol. 828, pp. 1–34, 2019, Silicon strip and pixel detectors for particle physics experiments, ISSN: 0370-1573. DOI: `https://doi.org/10.1016/j.physrep.2019.09.003`. [Online]. Available: `https://www.sciencedirect.com/science/article/pii/S0370157319302923`.

[33] G. P. et. al., "Technology developments and first measurements of low gain avalanche detectors (lgad) for high energy physics applications," *Nuclear Instruments and Methods in Physics Research Section A: Accelerators, Spectrometers, Detectors and Associated Equipment*, vol. 765, pp. 12–16, 2014, Proceedings of the 9th International "Hiroshima" Symposium on Development and Application of Semiconductor Tracking Detectors, ISSN: 0168-9002. DOI: `https://doi.org/10.1016/j.nima.2014.06.008`. [Online]. Available: `https://www.sciencedirect.com/science/article/pii/S0168900214007128`.

[34] S. Parker, C. Kenney, and J. Segal, "3d — a proposed new architecture for solid-state radiation detectors," *Nuclear Instruments and Methods in Physics Research Section A: Accelerators, Spectrometers, Detectors and Associated Equipment*, vol. 395, no. 3, pp. 328–343, 1997, ISSN: 0168-9002. DOI: `https://doi.org/10.1016/S0168-9002(97)00694-3`. [Online]. Available: `https://www.sciencedirect.com/science/article/pii/S0168900297006943`.

[35] H. V. Jansen, M. J. de Boer, S. Unnikrishnan, M. C. Louwerse, and M. C. Elwenspoek, "Black silicon method x: A review on high speed and selective plasma etching of silicon with profile control: An in-depth comparison between bosch and cryostat drie processes as a roadmap to next generation equipment," *Journal of Micromechanics and Microengineering*, vol. 19, no. 3, p. 033 001, Feb. 2009. DOI: 10.1088/0960-1317/19/3/033001. [Online]. Available: https://dx.doi.org/10.1088/0960-1317/19/3/033001.

[36] G. K. et. al, "Timing performance of small cell 3d silicon detectors," *Nuclear Instruments and Methods in Physics Research Section A: Accelerators, Spectrometers, Detectors and Associated Equipment*, vol. 934, pp. 26–32, 2019, ISSN: 0168-9002. DOI: https://doi.org/10.1016/j.nima.2019.04.088. [Online]. Available: https://www.sciencedirect.com/science/article/pii/S0168900219305704.

[37] H. F.-W. Sadrozinski, A. Seiden, and N. Cartiglia, "4d tracking with ultra-fast silicon detectors," *Reports on Progress in Physics*, vol. 81, no. 2, p. 026 101, Dec. 2017. DOI: 10.1088/1361-6633/aa94d3. [Online]. Available: https://dx.doi.org/10.1088/1361-6633/aa94d3.

[38] S. Garbolino, "Integrated front-end electronics for high precision timing measurements with radiation detector," Ph.D. dissertation, Università degli Studi di Torino, 2011.

[39] "Constant fraction discriminator." (2006), [Online]. Available: https://commons.wikimedia.org/wiki/File:Constant_fraction_1.svg.

[40] L. Landau, "56 - on the energy loss of fast particles by ionisation," in *Collected Papers of L.D. Landau*, D. TER HAAR, Ed., Pergamon, 1965, pp. 417–424, ISBN: 978-0-08-010586-4. DOI: https://doi.org/10.1016/B978-0-08-010586-4.50061-4. [Online]. Available: https://www.sciencedirect.com/science/article/pii/B9780080105864500614.

[41] S. Meroli. "The landau distribution and energy loss for ionizing particles." (2024), [Online]. Available: https://meroli.web.cern.ch/Lecture_landau_ionizing_particle.html.

[42] "Synopsys tcad." (2024), [Online]. Available: https://www.synopsys.com/silicon/tcad.html.

[43] G. Masetti, M. Severi, and S. Solmi, "Modeling of carrier mobility against carrier concentration in arsenic-, phosphorus-, and boron-doped silicon," *IEEE Transactions on Electron Devices*, vol. 30, pp. 764–769, 1983.

[Online]. Available: `https://api.semanticscholar.org/CorpusID:30133547`.

[44] C. Canali, G. Majni, R. Minder, and G. Ottaviani, "Electron and hole drift velocity measurements in silicon and their empirical relation to electric field and temperature," *IEEE Transactions on Electron Devices*, vol. 22, no. 11, pp. 1045–1047, 1975. DOI: `10.1109/T-ED.1975.18267`.

[45] E. Conwell and V. F. Weisskopf, "Theory of impurity scattering in semiconductors," *Phys. Rev.*, vol. 77, pp. 388–390, 3 Feb. 1950. DOI: `10.1103/PhysRev.77.388`. [Online]. Available: `https://link.aps.org/doi/10.1103/PhysRev.77.388`.

[46] A. O. W. Bludau and W. Heinke, "Temperature dependence of the band gap of silicon," *Journal of Applied Physics*, vol. 45, pp. 1846–1848, 1974. [Online]. Available: `https://api.semanticscholar.org/CorpusID:122507306`.

[47] L. V. group, "Radiation damage in the LHCb vertex locator," *Journal of Instrumentation*, vol. 8, no. 08, P08002–P08002, Aug. 2013. DOI: `10.1088/1748-0221/8/08/p08002`. [Online]. Available: `https://doi.org/10.1088%2F1748-0221%2F8%2F08%2Fp08002`.

[48] S. S. et. al., "The effect of humidity on reverse breakdown in 3d silicon sensors," *Nuclear Instruments and Methods in Physics Research Section A: Accelerators, Spectrometers, Detectors and Associated Equipment*, vol. 785, pp. 1–4, 2015, ISSN: 0168-9002. DOI: `https://doi.org/10.1016/j.nima.2015.02.056`. [Online]. Available: `https://www.sciencedirect.com/science/article/pii/S0168900215002661`.

[49] O. R. Kalliopuska J. Eränen S., "3d simulations of 3d silicon radiation detector structures," *Nuclear Instruments and Methods in Physics Research Section A: Accelerators, Spectrometers, Detectors and Associated Equipment*, vol. 568, no. 1, pp. 27–33, 2006, New Developments in Radiation Detectors, ISSN: 0168-9002. DOI: `https://doi.org/10.1016/j.nima.2006.07.015`. [Online]. Available: `https://www.sciencedirect.com/science/article/pii/S016890020601268X`.

[50] G. G. et al, "Simulations of 3d detectors," Conference presentation, 2011. [Online]. Available: `https://indico.cern.ch/event/104062/contributions/23157/attachments/14005/20413/giacomini.pdf`.

[51] "Institut jožef stefan." (2024), [Online]. Available: `https://www.ijs.si/ijsw/IJS`.

[52] M. B. et al., "Evaluation of the radiation field in the future circular collider detector," *Phys. Rev. Accel. Beams*, vol. 19, p. 111 004, 11 Nov. 2016. DOI: `10.1103/PhysRevAccelBeams.19.111004`.

[53] A.Chilingarov, "Distortion of the cv characteristics by a high current," Technical Note, 2003. [Online]. Available: `https://rd50.web.cern.ch/doc/recommendations.html`.

[54] "Particulars, advanced measurement systems." (2016), [Online]. Available: `http://particulars.si/`.

[55] A. M. S. Particulars. "Particulars-laser pulse." (2014), [Online]. Available: `http://www.particulars.si/downloads/Particulars-Procedures-LaserPulse.pdf`.

[56] A. M. S. Particulars. "User manual." (2015), [Online]. Available: `http://particulars.si/downloads/ParticularsLaserHardware-UserGuideV2.0.pdf`.

[57] "Deutsches elektronen-synchrotron desy." (2020), [Online]. Available: `https://www.desy.de/index_eng.html`.

[58] S. Ritt, *Psi drs4 user manual*, Apr. 2017. [Online]. Available: `https://www.manualslib.com/manual/1230412/Psi-Drs4.html?page=1#manual`.

[59] G.-F. D. et al, "3d trenched-electrode sensors for charged particle tracking and timing," *Nuclear Instruments and Methods in Physics Research Section A: Accelerators, Spectrometers, Detectors and Associated Equipment*, vol. 927, pp. 24–30, 2019, ISSN: 0168-9002. DOI: `https://doi.org/10.1016/j.nima.2019.02.015`. [Online]. Available: `https://www.sciencedirect.com/science/article/pii/S0168900219301901`.

[60] S. Hideaki and S. Shigeru, "A method for selecting the bin size of a time histogram," *Neural computation*, vol. 19, pp. 1503–27, Jul. 2007. DOI: `10.1162/neco.2007.19.6.1503`.

[61] Y. Laghla and E. Scheid, "Optical study of undoped, b or p-doped polysilicon," *Thin Solid Films*, vol. 306, no. 1, pp. 67–73, 1997, ISSN: 0040-6090. DOI: `https://doi.org/10.1016/S0040-6090(97)00247-2`. [Online]. Available: `https://www.sciencedirect.com/science/article/pii/S0040609097002472`.

[62] M. M. et al., "Comparative investigation of irradiated small-pitch 3d strip detectors," 2018.

[63] A. G. A. et al., ". charge collection efficiency of proton-irradiated small-cell 3d strip sensors up to 1.7 × 10 16n eq/cm2 equivalent fluence," 2018.

[64] "Light absorption and charge collection of highly irradiated silicon sensors," Krakow, June 2017.

[65] C. B. et al., "Time resolution of an irradiated 3d silicon pixel detector," *Instruments*, vol. 6, no. 1, 2022, ISSN: 2410-390X. DOI: `10.3390/instruments6010012`.

[66] L. D. et al., "Comparison of the time resolution of unirradiated and irradiated lgads and 3d sensors," *Nuclear Instruments and Methods in Physics Research Section A: Accelerators, Spectrometers, Detectors and Associated Equipment*, vol. 1046, p. 167 691, 2023, ISSN: 0168-9002. DOI: `https://doi.org/10.1016/j.nima.2022.167691`.

[67] N. C. et al., "Beam test results of a 16ps timing system based on ultra-fast silicon detectors," *Nuclear Instruments and Methods in Physics Research Section A: Accelerators, Spectrometers, Detectors and Associated Equipment*, vol. 850, pp. 83–88, 2017, ISSN: 0168-9002. DOI: `https://doi.org/10.1016/j.nima.2017.01.021`. [Online]. Available: `https://www.sciencedirect.com/science/article/pii/S0168900217300219`.

[68] "Ucsc pcb boards specifications." (2017), [Online]. Available: `https://twiki.cern.ch/twiki/bin/view/Main/UcscSingleChannel`.

[69] C. Grieco, "Low Gain Avalanche Detectors for the ATLAS High Granularity Timing Detector," Presented 11-07-2022, Ph.D. dissertation, Barcelona, Autonoma U. [Online]. Available: `https://cds.cern.ch/record/2816611`.

[70] N. e. a. Cartiglia, "Tracking in 4 dimensions," Oct. 2017, p. 489. DOI: `10.22323/1.314.0489`.

[71] H. Spieler, *Semiconductor Detector Systems*. Oxford University Press, Aug. 2005, ch. 8, ISBN: 9780198527848. DOI: `10.1093/acprof:oso/9780198527848.001.0001`. [Online]. Available: `https://doi.org/10.1093/acprof:oso/9780198527848.001.0001`.

[72] D. Contardo. "Technological progress and fcc-ee detector requirements." (2020), [Online]. Available: `https://indico.cern.ch/event/838435/contributions/3682439/attachments/1970986/3278846/FCC_DC_16012020.pdf`.

[73] T. K. et al, "Monolithic cmos sensors for sub-nanosecond timing," *Nuclear Instruments and Methods in Physics Research Section A: Accelerators, Spectrometers, Detectors and Associated Equipment*, vol. 979, p. 164 461, 2020, ISSN: 0168-9002. DOI: `https://doi.org/10.1016/j.nima.2020.164461`. [Online]. Available: `https://www.sciencedirect.com/science/article/pii/S0168900220308585`.

[74] N. S.-M. et al., "Altiroc, a 25 ps time resolution asic for atlas hgtd," 2019.

[75] "Medipix3." (2005), [Online]. Available: `https://medipix.web.cern.ch/medipix3`.

[76] A. Schenk, "A model for the field and temperature dependence of shockley-read-hall lifetimes in silicon," *Solid-State Electronics*, vol. 35, no. 11, pp. 1585–1596, 1992, ISSN: 0038-1101. DOI: `https://doi.org/10.1016/0038-1101(92)90184-E`. [Online]. Available: `https://www.sciencedirect.com/science/article/pii/003811019290184E`.

[77] R. Häcker and A. Hangleiter, "Intrinsic upper limits of the carrier lifetime in silicon," *Journal of Applied Physics*, vol. 75, no. 11, pp. 7570–7572, 1994. DOI: `https://doi.org/10.1063/1.356634`.